Università degli Studi di Salerno

Dipartimento di Ingegneria dell'Informazione ed Elettrica e Matematica Applicata

Tesi di Dottorato/Ph.D. Thesis

Models and Methods for the Identification of Degradation Processes in Photovoltaic Panels

Rudy Alexis Guejia Burbano

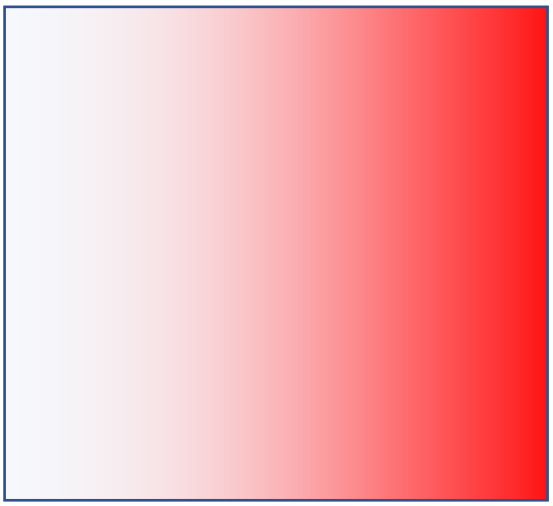

Supervisor: **Prof. Giovanni Petrone**

Ph.D. Program Director: **Prof. Pasquale Chiacchio**

Dottorato di Ricerca in Ingegneria dell'Informazione
Ciclo 34 – anno 2022

Università degli Studi di Salerno

.DIEM

Dipartimento di Ingegneria dell'Informazione ed Elettrica e Matematica Applicata

Dottorato di Ricerca in Ingegneria dell'Informazione
Ciclo 34

TESI DI DOTTORATO / PH.D THESIS

Models and Methods for the identification of degradation processes in photovoltaic panels

Rudy Alexis Guejia Burbano

SUPERVISOR: **Prof. Giovanni Petrone**

PHD PROGRAM DIRECTOR: **Prof. Pasquale Chiacchio**

2022

Acknowledgements

I'm extremely grateful to my advisor professor Giovanni Petrone for his great patient and guide during this road. I also could not have undertaken this journey without professor Martha Lucia Orozco, who puts her confidence and faith on my work and responsibility.

I am also grateful to professors Giovanni Spagnuolo and Walter Zamboni for their support, especially for making me feel calm, in family.

Lastly, to my family, my parents and my brother. They gave me the reasons for continuing to dream every day during this long trip. And to all of them who gave me words of faith for smiling during the long nights that I made a great effort to be a better person, a better engineer.

Abstract

Photovoltaic (PV) systems have become one of the most promising renewable energy sources in the last years. Inevitable, these systems face different degradation effects associated with environmental and operative conditions, manufacturing defects, and mismatch conditions that accelerate the degradation. The diagnosis of degradation processes has become an important topic for increasing the reliability and efficiency of PV devices. It seeks to maximize the performance of solar devices and contribute to early detection processes for enhancing the maintenance planning tasks saving energy and money losses.

The contribution of this thesis is aimed to propose methodological tools for carrying out early detection tasks of degradation effects on PV devices. Online implementations are in the spotlight since they bring the benefit of avoiding modifying the nominal operative condition of the PV devices. For achieving that goal, this thesis has addressed three main proposals for carrying out diagnosis of degradation processes on PV devices.

The first approach analyzed a selection of *analytical* or *explicit* methods validated in previous studies with good performance modeling photovoltaic devices in healthy conditions. In this case, the aim was to test their capability to detect degradation in photovoltaic modules. The study focused on the series resistance estimation since many degradation phenomena occurring in photovoltaic devices are reflected in a variation of the series resistance of the single diode equivalent circuit. A comparison of different explicit methods, used to estimate the model parameters from experimental I-V curves of a photovoltaic module operating in normal as well as degraded states under outdoor conditions, is proposed. It showed that only few methods exhibit enough reliability to estimate correctly the model parameters in presence of degradation and low sensitivity to the environmental operating conditions.

The second approach moved on to more complex parameter estimation methods such as *optimization* techniques. Here, neural networks (ANNs) are used for isolating faults and degradation phenomena occurring in photovoltaic (PV) panels. In literature, it is well known that the values of the single diode model (SDM) associated with the PV source are strongly related to degradation phenomena, and

their variation is an indicator of panel degradation. On the other hand, the values of parameters that allow identifying the degraded conditions are unknown a priori. They are different from panel to panel and strongly dependent on environmental conditions, PV technology, and manufacturing process. For these reasons, to correctly detect the presence of degradation, the effect of environmental conditions and manufacturing processes must be properly filtered out.

This approach exploits the intrinsic capability of multilayer perceptron (MLP) ANN to map in its architecture two effects: 1) the non-linear relations existing among the SDM parameters and the environmental conditions, 2) the effect of the degradation phenomena on the I-V curves and consequently on the SDM parameters. The variation of each parameter, calculated as the difference between the output of the two ANN stages, gives a direct identification of the type of degradation occurring on the PV panel. The method has been initially tested by using the experimental I-V curves provided by the National Renewable Energy Laboratory (NREL) database where the degradation effects were introduced artificially, and later tested by using some degraded experimental I-V curves.

The third approach is addressed to complement the aforementioned methodologies by extending the analysis to frequency-domain techniques. Thus, it presents a challenging and innovative approach for detecting degradation phenomena on photovoltaic (PV) panels using the Electrochemical Impedance Spectroscopy (EIS) technique. This technique has been applied to the chemistry field for a long time ago, but, it has a short history with PV devices. Previous studies have shown promising results with EIS as a tool for the diagnosis of PV devices but, most of them were limited to cell level and controlled conditions in the laboratory.

The innovation of this proposal is supported by two basic aspects that differentiate it from previous ones in the literature: the operating environmental conditions and the operating point. First, this work is aimed to detect degradation phenomena on photovoltaic (PV) devices at the panel level working under outdoor conditions by using the EIS technique. Secondly, the impedance is measured by leaving the PV panel in the real-operative status corresponding to the maximum power point without altering its power production. The implementation of the analysis in these conditions are innovative, but, at the same time mean a challenge due to it requires a detailed and careful implementation of the methods in the right way for characterizing the process.

As a preliminary step, the EIS technique is applied in simulation to analyze the PV panel dynamic response through a detailed LTSpice model including by-pass diodes. The degradation effect to analyze was partial shading conditions. Simulation results showed particular changes in the impedance shape under partial shading conditions only by performing the EIS with the panel operating in MPP thus without scanning the whole I-V curve. This confirmed the usefulness of EIS but also the necessity of going in deep with experimental data for obtaining a more

reliable representation of the device with its own representative element values.

As the experimental campaign had different challenges and required most careful steps, the first experimental implementation used a single PV panel. Since variations on the series resistance are associated with multiple degradation phenomena, this first experimental campaign sought to estimate changes in this parameter using a dynamic model fitted to the experimental impedance measurements. Hence, the PV panel impedance measurements are compared in nominal and degraded conditions. The results show that the dynamic model provides higher accuracy in comparison with the series resistance variation identified through the single–diode model, which is the most usual approach. Thus, it is demonstrated the feasibility of detecting degradation effects by using the dynamic model of PV panels working under outdoor conditions.

The next step consisted in extending the analysis to other effects as partial shading with two PV panels in series connection. Here, the number of PV panels for analyzing is restricted due to hardware limitations.

The objective of this stage was to compare the experimental impedance measurements in two conditions, uniform operating conditions and partial shading conditions. The preliminary results show that the partial shading conditions are also detectable by using EIS. But, the complete characterization of the whole effect requires extending the dynamic model to more complex models able to represent both dynamics in a representative model. Due to the reduced database with partial shading conditions currently available, a final assessment cannot be discussed. Nevertheless, the achieved results are very encouraging with interesting perspective for the future work.

Contents

State of Art of static and dynamic modelling of PV panels for degradation analysis **1**

1.1 Introduction 1

1.2 Modelling of Photovoltaic solar panels 4

1.2.1 PV static models: the Single Diode Model 4

1.3 Parameter identification approaches 6

1.3.1 Classification of methods 6

1.3.2 Relations among degraded PV panels and SDM parameters 7

1.4 Methods for the on-line diagnosis of PV systems 10

1.5 Frequency domain analysis 12

1.5.1 PV dynamic models 12

1.5.2 Electrochemical Impedance Spectroscopy 13

1.5.3 Impedance spectroscopy on photovoltaics (PV) panels . . . 16

Parameters Extraction of Single Diode Model for Degraded Photovoltaic Modules **18**

2.1 Introduction 18

2.2 Photovoltaic model and parameter identification methods 19

2.2.1 Explicit equations based on the LambertW function 19

2.2.2 Explicit equations by using the Serial–Parallel Ratio 21

2.2.3 Explicit equations based on the Phang's method 22

2.2.4 Explicit equations based on the Toledo's method 23

2.2.5 Identification method based on curve fitting 24

2.2.6 Data extrapolation from experimental I-V curve 25

2.3 Experimental methodology 27

2.3.1 Measurement system and setup 27

2.3.2 Data pre–processing 28
2.4 Comparison of the identification methods in nominal conditions . . 29
2.5 Results with additional series resistance 34
2.6 Conclusions 39

Early Detection of Photovoltaic Panel Degradation through Artificial Neural Network 41
3.1 Introduction 41
3.2 Description of the proposed approach 42
3.3 Description of Experimental $I-V$ curves Database 44
3.3.1 Generation of training set and validation set for a healthy PV panel 46
3.3.2 Generation of training set and validation set for a degraded PV panel 47
3.4 Configuration of the proposed double level ANN architecture . . . 48
3.4.1 Dataset Normalization 50
3.4.2 Overfitting and Generalization 51
3.5 ANN identification results for healthy conditions 52
3.6 ANN results with simulated degradation on $I-V$ curves 55
3.6.1 Improving the ANN results with repeated tests 61
3.6.2 Comparison with other ANN solutions 62
3.7 ANN results with experimental degraded $I-V$ curves 64
3.8 Extending the methodology to other PV panels and technologies . 65
3.8.1 Performance analysis of ANN used as regression model . . . 72
3.9 Conclusions 74

Impedance Spectroscopy for Diagnosis of Photovoltaic Modules under Outdoor Conditions 76
4.1 Introduction 76
4.2 Impedance Spectroscopy simulations for partial shading detection . 77
4.2.1 PV panel modelling and circuit configuration 78
4.2.2 Simulation of the PV Module under Mismatched Conditions 80
4.2.3 EIS analysis and discussion of simulation results 83
4.3 Measurement setup and EIS data validation 86
4.3.1 Configuration of the EIS instrumentation 86
4.3.2 Experimental Platform Description 88

4.3.3 Selection of the operating point for measuring stable EIS spectra 90
4.3.4 Reliability of the spectra at MPP 92
4.4 Impedance spectroscopy for online series resistance monitoring . . 95
4.4.1 Analisys of experimental EIS for a single PV module . . . 95
4.4.2 Identification of the series resistance degradation 98
4.5 Impedance spectroscopy for partial shading detection 103
4.5.1 Setup of series connected PV panels 103
4.5.2 Series connected panels operating in partial shading conditions 107
4.5.3 Uniform vs. partial shading condition operation 109
4.6 Double arc identification on the impedance spectra 109
4.6.1 Analysis of EIS experimental data with improved quality . 109
4.6.2 PV dynamic models for PV string operating in partial shading conditions 111
4.6.3 Detection of small partial shading effect 116
4.6.4 EIS measurement vs. simulation data 116
4.7 Conclusion 119

General Conclusions **120**

Future Works **123**

REFERENCES **124**

List of Figures

1.1 Equivalent circuit of the single diode model 5
1.2 Generic voltage vs current relationship for a PV device 5
1.3 Summary methodologies for parameter identification. 7
1.4 Module failures detectable from the $I-V$ curve 8
1.5 Ideal small-signal PV dynamic model 12
1.6 Dynamic model with a constant phase element (CPE). 13
1.7 Identification of the impedance spectra through a sinusoidal stimulation of V_p, I_p 14
1.8 (a) Complex plane, (b) Bode magnitude diagram, and (c) Bode phase diagram of the impedance values of the PV panel. 15
2.9 Slopes approximation on the I–V curve 26
2.10 SDM with additional series resistance 28
2.11 Experimental curves of PV panel under study with different added series resistances 30
2.12 I_{ph} estimation at different irradiance conditions with respective regression lines 31
2.13 Estimations of series and parallel resistances at different irradiance conditions by using the selected identification methods 32
2.14 Detection of additional series resistance ΔR_s for Phang and Toledo methods 36
2.15 Detection of additional series resistance ΔR_s for LambertW and SPRatio methods 37
2.16 Comparison between experimental and simulated curves for different experiments 39
3.17 Flow chart for training the proposed ANN architecture 43
3.18 Healthy and degraded $I-V$ curves with the selected points passed to the ANN 48
3.19 Proposed ANN architecture 49

3.20 ANN identification of the photoinduced current in healthy condition. 52
3.21 ANN identification of the saturation current in healthy condition. . 53
3.22 ANN identification of the ideality factor in healthy condition. . . . 53
3.23 ANN identification of the series resistance in healthy condition. . . 53
3.24 ANN identification of the shunt resistance in healthy condition. . . 54
3.25 Comparison of experimental data and reconstructed single-diode $I-V$ curve with estimated ANN parameters in healthy condition. In this case the error area is 5% 54
3.26 Comparison of experimental data and reconstructed single-diode $I-V$ curve with estimated ANN parameters in healthy condition. In this case the error area is 0.5% 55
3.27 ANN identification of degraded curve with -5% of variation on I_{ph} for two different irradiance and temperature conditions. 57
3.28 ANN identification of degraded curve with 200% of variation on I_{sat} for two different irradiance and temperature conditions. 58
3.29 ANN identification of degraded curve with -3% of variation on η for two different irradiance and temperature conditions. 59
3.30 ANN identification of degraded curve with 70% of variation on R_s for two different irradiance and temperature conditions. 59
3.31 ANN identification of degraded curve with -80% of variation on R_{sh} for two different irradiance and temperature conditions. 60
3.32 Experimental $I-V$ curves with added series resistance for the same environmental conditions 64
3.33 ANN identification of series resistance for different induced degradation effect and for different environmental conditions . . . 65
3.34 Trend of the set of five parameters and their percentage confidence interval error for a temperature range of [35-36] °C 66
3.35 Percentage confidence Interval error for every parameter in a temperature range of [35-36] °C 68
3.36 Percentage confidence Interval error for the set of five parameters of PV panel B in a temperature range of [35-36] °C 70
3.37 Percentage confidence Interval error for the set of five parameters of PV panel C in a temperature range of [37-38] °C 71
3.38 Performance of different machine learning techniques for characterizing the degradation effect on the set of five parameters: *Stage 2* of the figure 3.17 72

3.39 Performance of different machine learning techniques with a optimized procedure for detecting the degradation effect on the set of five parameters: *Stage 2* of the figure 3.17 73

4.40 Module configuration by using SDM for simulation on LTSpice . . 79

4.41 I-V curves of the Kyocera KC175GHT-2 using the SDM equation (red) and the LTSpice circuital setup (blue) 80

4.42 Scheme for the PV panel stimulation for performing the EIS. . . . 81

4.43 Simulated I-V curves of Kyocera KC175GHT-2 in uniform and mismatched condition. 82

4.44 Impedance diagram at STC of the PV panel simulated with LTSpice 83

4.45 Comparison of impedances resulting from the studied cases of mismatching. Blue points represent the ideal state at STC. Green points show a normal operation under low irradiance conditions. Red points depict the mismatch condition presented in table 4.27. 84

4.46 Variation of EIS for different levels of mismatch and low irradiance cases 85

4.47 Biologic configuration tool 86

4.48 Hardware setup arranged for the experimental process. 88

4.49 Relationship between the *I–V* curve and the impedance values in the complex plane with different operating points at a particular environmental condition ($G = 951$ W/m^2 and $T = 52$ °C). 90

4.50 Validation of the Lin-KK tool for a impedance measurement at V_{oc} 93

4.51 Validation of the Lin-KK tool for a impedance measurement at MPP. 94

4.52 Validation of the Lin-KK tool for impedance measurements at (MPP + 1 [V]) 94

4.53 Comparison of the experimental R_{mpp} values and the impedance ad zero frequency using the CPE model. Upper plot: PV module at nominal conditions. Lower plot: PV module with the external resistor. 97

4.54 Comparison of test cases #10 (red markers) and #6 (blue markers) from Tables 4.33 and 4.34 respectively. 98

4.55 Parameters variation of the CPE dynamic model as function of the operating point of the *I–V* curve 99

4.56 Left plot: R_s estimated by using SDM. Right plot: R_0 estimated by using EIS spectra. The asterisks refer to the parameters in nominal conditions. The square markers refer to the tests with the external resistance. 100

4.57 Regression process for the values calculated using the SDM and the dynamic model in the two test cases. 102
4.58 Percentage error estimation between the nominal delta value ($\Delta R = 0.175\ \Omega$) and the value given by the SDM and the dynamic model using the regression curves for the whole irradiance range. . 102
4.59 PV panel disposition. 104
4.60 Static (a) and dynamic (b) response of two series connected PV panels under uniform environmental conditions. 104
4.61 Static (a) and dynamic (b) response of two series-connected PV panels under partial shading conditions. 107
4.62 Comparison of static a) and dynamic response b) of two series connected PV panels under uniform and partial shading conditions. 110
4.63 Different operating points for PV panels operating in partial shading conditions 111
4.64 Static (a) and dynamic (b) response of two series connected PV panels under uniform environmental conditions with optimised perturbation amplitude. 112
4.66 PV dynamic models for representing PV string operating in partial shading condition. 112
4.65 Static (a) and dynamic (b) response of two series connected PV panels under partial shading conditions with optimised perturbation amplitude. 113
4.67 Fitted impedance spectra with models of fig.4.66 for two series connected PV panels under partial shading conditions. 115
4.68 Static (a) and dynamic (b) response of two series connected PV panels under partial shading conditions with optimised perturbation amplitude. 116
4.69 Static (a) and dynamic (b) response of two series connected PV panels under partial shading conditions with optimised perturbation amplitude. 117
4.70 Comparison of experimental vs. simulation data of two partial shaded PV panels. 118

List of Tables

1.1 Preliminary EIS studies on solar PV cells/modules 17
2.2 Interval and start points for the five SDM parameters 24
2.3 Tuning parameters for the fitting procedure 25
2.4 Isofotón I-53 main specifications 28
2.5 Mean value μ and standard deviation σ of the 5 SDM calculated by different methods 33
2.6 *MAPE* of electrical parameters and global curve error *(GCE)* . . . 34
2.7 Mean value μ and standard deviation σ of the parameters with additional $R_s = 1.5\,\Omega$ 38
2.8 *MAPE* of electrical parameters and global curve error (*GCE*) with $\Delta R_s = 1.5\,\Omega$ 38
3.9 Characteristics of the PV panel under study and ranges of the data measured. 45
3.10 Pseudo code for generating degraded $I-V$ curves 47
3.11 SDM parameters variation for generating degraded $I-V$ curves . 48
3.12 SDM parameters estimated with ANN for $I-V$ curves of figure 3.27 58
3.13 SDM parameters estimated with ANN for $I-V$ curves of figure 3.28 58
3.14 SDM parameters estimated with ANN for $I-V$ curves of figure 3.29 59
3.15 SDM parameters estimated with ANN for $I-V$ curves of figure 3.30 60
3.16 SDM parameters estimated with ANN for $I-V$ curves of figure 3.31 61
3.17 Average of SDM parameters variation (in %) estimated with ANN 62
3.18 ANN techniques for PV diagnosis and faults identification 63
3.19 CI error ranges for the set of parameters (Fig.3.34) 67
3.20 CI error ranges for the set of parameters (Fig.3.35) calculated with the RMSE cost function 69
3.21 Characteristics of the PV panel under study and ranges of the data measured. 69

3.22 CI error ranges for the set of parameters (Fig.3.36) calculated for the PV panel B 70
3.23 CI error ranges for the set of parameters (Fig.3.37) calculated for the PV panel C 71
3.24 Summary of the main characteristics of the regressors assessed . . 73
4.25 Kyocera KC175GHT-2 datasheet characteristics at STC and SDM parameters. 78
4.26 Characteristics of the by-pass diode VSB2045 (PV solar cell protection Schottky rectifier) 79
4.27 Testing cases for analysing the effect of mismatch on the EIS spectra. 82
4.28 Python Automator functions 87
4.29 Data structure for the I-V curve measurements 87
4.30 Data structure of the Impedance Spectroscopy measurements . . . 88
4.31 Nominal parameters of the Solbian FLEXSP50L PV panel 89
4.32 Basic information of the environmental sensors used for sensing the ambient conditions. 89
4.33 Parameter estimation by using the CPE model at MPP under different irradiance levels. 96
4.34 Parameter estimation by using the CPE model at MPP under different irradiance levels with an additional external resistor. . . . 97
4.35 Preliminary comparison of the series resistance variation found by the SDM and the dynamic CPE model. 100
4.36 Parameters of the regression curves for the series resistance values found using the SDM and the dynamic model (EIS). 101
4.37 Preliminary comparison of the series resistance variation found by the SDM and the CPE model($\Delta R = 0.35\ \Omega$). 103
4.38 Estimated parameter of the CPE model for different environmental conditions. 106
4.39 Estimated parameter of the CPE dynamic model in partial shading conditions. 108
4.40 Estimated parameter of a double RC branch 114
4.41 Estimated parameter of the CPE model plus with an additional RC branch 114
4.42 Estimated parameter of a double CPE model 114
4.43 Summary of the methodologies proposed 122

List of publications

The research in this thesis has been previously divulged through a series of journal, conference, and book chapter publications. These publications are:

Journal

J1 M. Piliougine, R. A. Guejia-Burbano, G. Petrone, F. J. Sánchez-Pacheco, L. Mora-López, and M. Sidrach-de-Cardona, **"Parameters extraction of single diode model for degraded photovoltaic modules,"** Renew. Energy, vol. 164, pp. 674–686, 2021, doi: 10.1016/j.renene.2020.09.035. [Online] Available: *https://doi.org/10.1016/j.renene.2020.09.035*

J2 Guejia Burbano RA, Petrone G, Manganiello P. **"Early Detection of Photovoltaic Panel Degradation through Artificial Neural Network"**. Applied Sciences. 2021; 11(19):8943. doi:10.3390/app11198943. [Online] Available: *https://doi.org/10.3390/app11198943*.

J3 R. A. Guejia-Burbano, M. Piliougine, G. Petrone, **"Impedance Spectroscopy for Diagnosis of Photovoltaic Modules under Outdoor Conditions"** [Manuscript submitted for publication on IEEE Journal of Photovoltaics], Dipartimento di Ingegneria dell'Informazione ed Elettrica e Matematica Applicata, Università degli Studi di Salerno, 2022.

Conference

C1 R. A. Guejia-Burbano and G. Petrone, **"Partial shading detection on PV panels through on-line Impedance Spectroscopy,"** 2021 IEEE International Conference on Environment and Electrical Engineering and 2021 IEEE Industrial and Commercial Power Systems Europe (EEEIC / I&CPS Europe), 2021, pp. 1-6, doi: 10.1109/EEEIC/ICPSEurope51590.2021.9584621. [Online] Available: *https://doi.org/10.1109/EEEIC/ICPSEurope51590.2021.9584621*

C2 R. A. Guejia-Burbano, V. Noviello, G.Petrone, **"Online detection of PV degradation effects through ANN Classifier"**, 14th International Conference of TC-Electrimacs Committee (Electrimacs 2022), 2022.

Book chapter

B1 G. Petrone, L. Orza, F. J. Sánchez-Pacheco, R. A. Guejia-Burbano, M. Piliougine, L. Mora-López, and M. Sidrach-de-Cardona. "Reliability of Explicit Methods to Identify the Parameters of PV Panels with Degraded Series Resistance: An Experimental Comparison" DOI:10.1007/978-3-030-56970-9_10. pp.117-128. In ELECTRIMACS 2019 - Selected Papers Volume 2. In LECTURE NOTES IN ELECTRICAL ENGINEERING - ISSN:1876-1100 vol. 697

Apart from that, a cooperation was carried out in the development of additional papers. As they were out of the scope of this document, they were not included in the current thesis.

Cooperations

COOP1 M. Piliougine, R.A. Guejia-Burbano, G. Spagnuolo, Detecting Partial Shadowing and Mismatching Phenomena in Photovoltaic Arrays by Machine Learning Techniques. (2022). UNDER REVISION to be published in IEEE Open Journal of the Industrial Electronics Society.

State of Art of static and dynamic modelling of PV panels for degradation analysis

1.1 Introduction

Photovoltaics (PV) is a key technology for the transition from fossil fuels toward a decarbonized and sustainable energy supply [1]. Solar energy is available and abundant in a large part of the world and cannot be monopolised, thus, the development of PV systems, as well as other renewable sources is strategic for many countries and societies. Moreover, the penetration of photovoltaic (PV) generation in the urban environment is significantly growing owing to its ability to reduce the power bills of the owners and support the grid with local generation[2].

Research activities in the field of PV cell technology, power electronics, monitoring, control processes, and grid integration are generally focused on improving the PV energy production and system reliability, thus increasing the overall efficiency of PV installations and reducing the cost. However, despite a very long lifetime (around 25 years) of PV modules, many studies [3] highlight that some degradation effects can be accelerated by various unpredictable and unavoidable phenomena which are related to the environmental and the operating conditions, the type of electrical connections and the manufacturing processes, among others [4]. For example, especially in urban area, residential PV plants have high probability to be subject to panel mismatch, partial shading, hot spots, and/or mechanical stress that accelerate the degradation phenomena. Another example is shown in [5], where the authors prove that the combined effect of PV delamination, water penetration into the delaminated area and high string voltage operation, leads to many failures in PV panels and inverters. Since the severity of delamination increases gradually, this phenomenon can be early detected so that the affected PV panel can be replaced with a new one. This preventive maintenance will reduce the risk of PV system outages, avoid further damages

and consequently keep the PV plant up and running, thus increasing the PV plant's energy yield over the system lifetime.

Some of these degradation mechanisms induce visible negative effects on the photovoltaic module, e.g discolouration of the encapsulation material, bubble formation or snail tracks, with possible detrimental effects on the photovoltaic electrical parameters [6]. Despite these visual defects, many faults and degradation phenomena cannot be distinguished with a visual inspection thus no information can be provided to users that could request the replacement of the modules if they do not meet the warranty, especially if the degradation is due to the manufacturing processes. Furthermore, PV modules also exhibit a natural aging that reduces the annual PV energy production with a more or less flat degradation rate. For crystalline silicon PV modules, it has been estimated a reduction of [0.8-0.9]% over the year [7]. An exhaustive review of degradation phenomena occurring in PV modules is reported in [8].

For these reasons, in the PV market there is an increasing interest into non–invasive and cheap functionalities to be integrated into PV plants in order to identify early degradation of PV panels, some smart products are already available for residential applications [9]. An early detection of PV degradation allows to take decisions about system maintenance and PV panel replacements. In some cases, it can prevent catastrophic consequence like fires. On–site monitoring systems are aimed to provide/report information about the energy production, operating conditions and analysis of different faults. In this scenario, diagnostic functions allow to detect quickly the faulty PV modules and to estimate the difference between the produced energy and the expected one, thus supporting the owners of PV plants to reduce the payback time and maximise the profit from the produced energy. In [10] a review of effective, low cost, and viable PV monitoring systems for small and medium scale PV plants is shown.

In the literature it is possible to find two different approaches to characterise a photovoltaic panel (and hence having a tool to estimate the degradation). The first type relies on the performing of a comparison between the solar energy received by the PV module, and the electrical energy delivered through its terminals and estimated by means of its electrical measurement [11, 12, 13]. The electrical behaviour of a photovoltaic module under specific conditions of irradiance and cell temperature is described in terms of its I-V curve [14]. In order to estimate the energy input it is required a solar irradiance sensor and a cell temperature sensor attached to the module, then the PV performance, in a given window of time, is obtained by calculating an indicator denominated Performance Ratio [15]. The evolution of this performance indicator throughout time allows to detect the possible degradation in terms of energy production [16]. The drawback of this approach is that hardly the required sensors are available due to their high costs [17], and in the case of having them, there are multiple associated problems related

to the inaccuracy of measurement and their periodically calibration and cleaning [18].

Other techniques, usually defined as *"model–based"* approaches, consist on the identification of some parameters associated to models that are suitable to describe accurately the electrical behaviour of the photovoltaic devices. Depending on the evolution of these parameters, the degradation could be diagnosed and estimated [19, 20, 21]. The identification of the values of these parameters could be done from the data obtained only from its *I-V* curve without measuring the irradiance. Moreover, some of these methods only require a few selected points of the *I-V* curve.

Static and dynamic models are employed to detail specific characteristics of the PV device that are commonly not present in the manufacturer datasheet. Regarding static models, the most popular photovoltaic electrical models are the Single Diode Model (SDM) and the Double Diode Model (DDM) [22], both derived from Schottky diode equation with the addition of a series resistance and a parallel resistance for taking into account the losses inside the PV device. For both models the relationship between voltage and current (mathematical model of the PV module) is described by a non–linear and implicit equation with five unknown parameters for the SDM and seven unknown parameters for the DDM.

From the other side, dynamic models search to integrate the PV system as a whole. The capacitance is the dominant effect that a PV cell/module has internally. But additional effects that result from other elements as the parasitic inductance or series conductance support the relevance of a model that covers the impact of all these dynamic elements. The identification of that elements commonly uses two approaches from the literature. Frequency-domain and time-domain analysis implement different methodologies for describing the physical phenomena governing the behavior of the PV solar cell, especially the phenomena that affect its internal capacitance [23]. The analysis of the dynamic element variation is another way that helps to depict different degradation phenomena present in the PV cell/module that are not discernible using only static analysis. Thus, static and dynamic model-based approaches can be complementary for diagnosing the degradation effects growing in the PV device.

As described in literature [24], the diagnostic procedures could be classified into *"off–line"* and *"on–line"* methods. The *"off–line"* methods require to disconnect the module from the photovoltaic array to be measured and characterised independently. On the contrary, *"on–line"* methods use information acquired while the module is working without disconnecting it from the array. Due to their low cost and flexible configurations, embedded systems installed on site are used to perform the measurement and process the experimental data. As *"on-line"* diagnostic methods are directly implemented on this type of devices, it is useful that the algorithms or equations required to implement those methods are as

simple as possible to speed up the data processing, avoiding implicit expressions and iterative procedures.

Thus, the current thesis has taken into account the issues, the set of methodologies, studies, theories, and models previously mentioned for implementing methodological tools for the early identification of degradation processes in solar PV devices. To confront this challenge, this work has proposed methodologies addressing the problem to online implementations.

The methodologies are guided to keep the devices in nominal operative conditions for power production. It means non-invasive methodologies, able to perform the diagnosis in the field for avoiding energy and power losses.

The argument of the thesis is structured into four chapters. The first chapter introduces the discussion of the problems to address. Here, a summary of the main PV models and methods for analyzing PV degradation phenomena are presented briefly. This information is expanded and duly explained in the specific chapters where they are used. The second chapter is focused on the analysis of the performance of model-based approximations for detecting degradation effects using experimental data. The third chapter employs numerical algorithms and computational intelligence approaches for creating an architecture that assesses degradation effects in PV devices using the main characteristics of the static PV model. Finally, chapter four exploits the frequency-domain techniques and the dynamic PV model for mapping the relationship between degradation effects and changes in the dynamic PV element values.

1.2 Modelling of Photovoltaic solar panels

1.2.1 PV static models: the Single Diode Model

Figure 1.1 shows the single–diode model (SDM) equivalent electrical circuit of a PV device [22]. It can be scaled–up or down to be adapted to a single PV cell, a PV module or a PV array, depending on the number of cells connected in series and parallel. The corresponding SDM equation for a photovoltaic module is given in (eq 1.1).

$$I = I_{ph} - I_0 \cdot \left(exp\left\{ \frac{V + I \cdot R_s}{n_s \cdot n \cdot V_t} \right\} - 1 \right) - \frac{V + I \cdot R_s}{R_{sh}} \tag{1.1}$$

where V is the voltage between the terminals of the photovoltaic module (V), I is the output current (A), I_{ph} is the photo-generated current (A), I_0 is the dark saturation current (A), n is the diode ideality factor (dimensionless), R_s is the series resistance (Ω), R_{sh} is the shunt or parallel resistance (Ω) and n_s is the

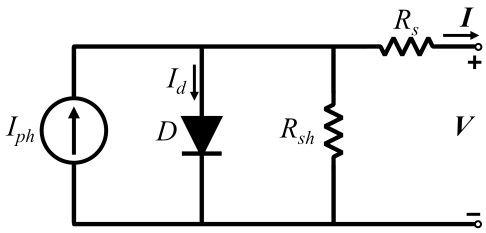

Figure 1.1. Equivalent circuit of the single diode model

number of cells in series.

In addition, V_t is the thermal voltage (V) given by kT/e, being k the Boltzmann constant (1.380649×10^{-23} JK^{-1}), e the elementary electric charge ($1.602176634 \times 10^{-19}$ C) [25] and T the cell temperature expressed in kelvin (with $T = 273.15 + T_m$ if T_m is expressed in °C).

The SDM, shown in figure 1.1, is the most used PV model due to the trade-off between simplicity and accuracy [26]. This model, together to double-diode model (DDM), and triple-diode model (TDM) are widely used for modeling, simulation, performance evaluation, design optimization of PV systems as well as for monitoring and diagnosis purposes [27]. Indeed, the accurate parameter identification of the equivalent PV electrical model allows to study the characteristics of a PV source[28] in whichever operating conditions. So that, instead of analysing the shape of each $I - V$ curves, it is easier to detect degradation by evaluating the variation of such parameters with respect their values in healthy conditions.

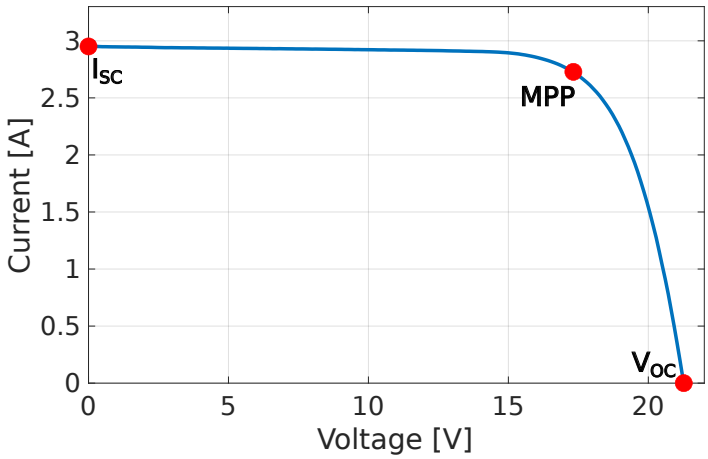

Figure 1.2. Generic voltage vs current relationship for a PV device

Figure 1.2 shows the characteristic relationship between the current and voltage

(I-V curve) of a cell, module, or array at specific environmental conditions (irradiance and temperature). Here, the main points of the curve are the short-circuit current (I_{sc}), the open-circuit voltage (V_{oc}), and the maximum power point (MPP). When the device is short-circuited (positive and negative terminals connected directly), the voltage in the device is at the minimum value (zero), and the current flowing out reaches the maximum. This point is named I_{sc}. On the other hand, when the device does not have connected any load (open-circuited), the current goes to zero value and the voltage in the device terminals reaches the maximum. This is called V_{oc}. Finally, The MPP refers to the point when there is a special combination of current and voltage where the electrical power generated reaches the maximum.

1.3 Parameter identification approaches

1.3.1 Classification of methods

To reproduce accurately the I–V curve of a PV array, it is not enough to have a good mathematical model (e.g. the SDM), but it is also necessary to correctly determine or estimate its parameters. The lasts can vary from one cell/module to another and depend on the operating conditions, thus resulting extracted parameters influence the final accuracy of the adopted model [29].

In the literature, it is possible to find a lot of deterministic and stochastic methods available to determine a valid set of the parameters values (I_{ph}, I_0, n, R_s and R_{sh}) [30, 31, 32, 33]. There are also works that are only able to estimate a reduced subset of the parameters [34, 35, 36], even some that are only focused on the identification of the series and shunt resistances [37, 38], since internal resistances are indicators of some degradation phenomena. For example, the series resistance is affected by corrosion in the electrical contacts, soldering problems and degradation of the cells, among others [39].

The paper [40] provides an extensive review of works related to the modelling and parameter estimation of photovoltaic (PV) cells, mainly devoted to the PV simulation. Among them, the explicit methods are strongly appreciated due to the fact that they provide acceptable results with very few computational burden [41]. They usually exploit the three notable points that an I-V curve passes through: the short–circuit current (I_{sc}) , the open–circuit voltage V_{oc} and the maximum power point (V_{Pmax}, I_{Pmax}). In some cases, the slopes of the I–V curve calculated in I_{sc} and V_{oc} are also needed.

The parameters identification is a relevant task since they are not available on the PV panel manufacturer datasheet. Besides, there are variations associated with the operating conditions, non-linear nature, and degradation phenomena [42].

Methodologies for solving this task are commonly grouped into three categories [43]: iterative (numerical), non-iterative (analytical), and AI-based optimization approaches.

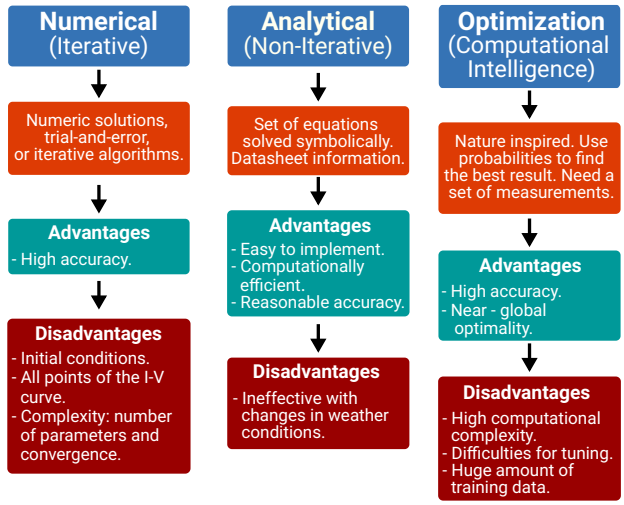

Figure 1.3. Summary methodologies for parameter identification.

Analytical methods use equations solved symbolically or explicitly by using key-points information from datasheet or $I-V$ curve data. These approaches are characterized by the simplicity of its implementation and computational efficiency [44].

Numerical methods seek to fit the points of the $I-V$ curve by using systems of equations that are solved numerically. Commonly, trial and error approaches or numerical solvers such as Newton-Raphson and curve-fitting methods are used. The accuracy, reliability, and convergence of these methodologies are strongly linked to the selection of the initial conditions [43, 45].

Optimization approaches group different kinds of algorithms based on artificial intelligence and heuristics methods. The development of computational intelligence has improved the implementation of these algorithms to solve highly non-linear and complex problems. Many advantages are associated with these approaches as no preliminary identification of the search space of parameters, high accuracy, and in some cases they do not need of a mathematical model. Nevertheless, it requires high computational complexity [28].

1.3.2 Relations among degraded PV panels and SDM parameters

In [46] the most common degradation effects and failures that are detectable by the inspection of the $I-V$ curve and the related SDM parameters variations are

described. They are visually shown in Figure 1.4. A brief comment on these effects is also reported in the following. It is worth to note that, for copyright restrictions, any photo concerning degraded PV modules is reported in this thesis, nevertheless the visual effects of degradation phenomena on PV modules are well documented in [46] and related references.

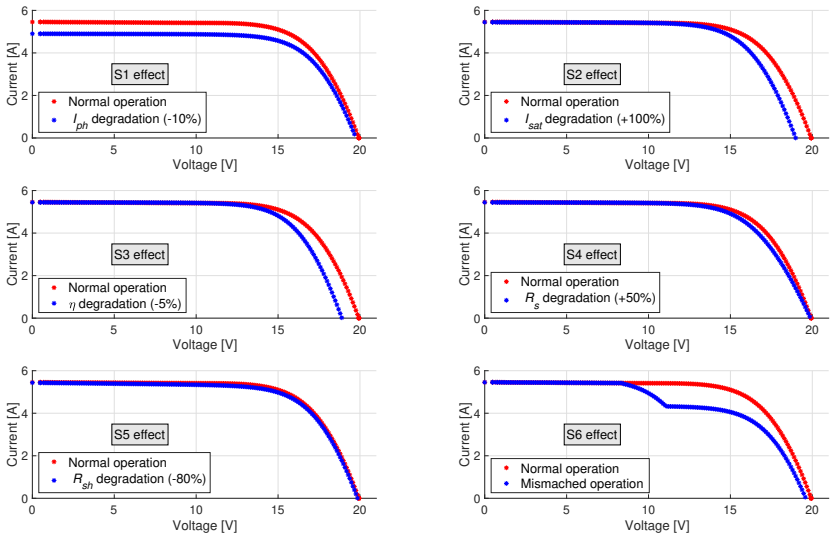

Figure 1.4. Module failures detectable from the $I-V$ curve

- **S1 effect:** The $I-V$ curve exhibits a lower short-circuit current (I_{sc}) than expected.
  This degradation effect may be caused by the loss of transparency of the encapsulation due to browning or yellowing, glass corrosion which reduces the light trapping of the module, or delamination which causes optical uncoupling of the layers. This is mainly reflected in the reduction of the photoinduced current (I_{ph}) parameter.

- **S2 and S3 effects:** The $I-V$ curve has an open circuit voltage (V_{oc}) lower than expected, all points shift homogeneously to the left while the $I-V$ curve preserves its slope around V_{oc}. This anomaly may be due to failed cell interconnections, short circuits from cell to cell or a failure of the bypass diode. Such kind of failure can be associated to the SDM ideality factor (η) because the number of cells (n_s) in a PV module directly appear in the SDM equation (1.1). Thus, the effects of cells failures can be expressed as:

$$\eta = \eta_H \frac{n_H}{n_s} \tag{1.2}$$

where η_H is the healthy ideality factor and n_H is the number of healthy cells inside the PV panel made of n_s cells. For example, if $n_s = 36$, one failed cell has an impact of almost -3% on the η parameter.
The open-circuit voltage of the module can be reduced also by the light-induced degradation (LID) of crystalline silicon modules or potential induced degradation (PID). Since the leakage current inside the PV cell is an indicator of such phenomena, they can be directly associated to the variation of saturation current I_{sat} parameter. Small variation of I_{sat} does not affect significantly the $I - V$ characteristic. It can be observed that the impact of I_{sat} and η is right opposite. This can cause multi-modal problem in the parameter identification, which means that the same $I - V$ curves may be reproduced with different pairs of the I_{sat} and η. Therefore, in some cases the same degradation phenomena can be associated almost indifferently in the I_{sat} variation or η variation.

- **S4 effect:** The slope of the $I - V$ curve near V_{oc} is lower indicating an increase of the series resistance R_s in the PV module.

  Among the SDM parameters, R_s appears as a key parameter due to its straightforward relation with several degradation effects in PV devices. Sera *et al.* [37, 47] show that the series resistance is the main element that affects the fill factor. Here, degrading welding points and malfunctioning cells are linked to the variation in this parameter. Stein *et al.* [48] assume the series resistance as a representation of all contacts, series–connected cell layers, and wires. Therefore, a change in this element can be associated with corrosion and UV degradation. Deceglie *et al.* [49] consider the series resistance as an indicator of broken ribbons, broken solder bonds, and contact problems. Finally, in [50] the R_s is viewed as a representation of all signs correlated to the degradation processes.

- **S5 effect:** The slope around I_{sc} is mostly associated to the parallel resistance R_{sh}. The variation of this parameter is due to shunt paths in the PV cells and/or the interconnections. Slight cell mismatch or slight non uniform yellowing, may be another cause.

- **S6 effect:** The presence of steps in the curve is likely caused by the activation of one or more by–pass diodes that are connected in parallel to block of cells to protect them from inverse polarization during mismatched operating conditions. It can be due to irregular soiling or shadow affecting only few cells in the PV module or due to the breakage of one or more cells protected by the same by pass diode. This effect cannot be reproduced with a single diode model, thus the variations of the SDM parameters associated to this effect have not a physical meaning.

Since all degradation phenomena have an impact on the delivered power, the normalised sensitivity ($\mathbf{S_n}$) of the PV output power with respect to the SDM parameters variation has been calculated as follows:

$$\begin{aligned}\mathbf{S_n} &= [s_{n,I_{ph}}, s_{n,I_{sat}}, s_{n,\eta}, s_{n,R_s}, s_{n,R_{sh}}] = \\ &= \left[\frac{\Delta P_{mpp}}{\Delta I_{ph}}\frac{I_{ph,H}}{P_{mpp,H}}, \frac{\Delta P_{mpp}}{\Delta I_{sat}}\frac{I_{sat,H}}{P_{mpp,H}}, \frac{\Delta P_{mpp}}{\Delta \eta}\frac{\eta_H}{P_{mpp,H}}, \frac{\Delta P_{mpp}}{\Delta R_s}\frac{R_{s,H}}{P_{mpp,H}}, \frac{\Delta P_{mpp}}{\Delta R_{sh}}\frac{R_{sh,H}}{P_{mpp,H}}\right]\end{aligned} \tag{1.3}$$

where the $s_{n,k}$ is the normalised sensitivity calculated by introducing the variation Δk to the k-parameter. The subscript $_H$ refers to the values in healthy conditions. Due to the non-linearities of PV power with respect to the SDM parameters, the sensitivity is not constant and it should be calculated locally and for the different environmental operating conditions. The normalised sensitivity values of the delivered PV power with respect to the five parameters variation shown in figure 1.4 is reported in (1.4).

$$\mathbf{S_n} = [1.04, \text{-}0.0606, 1.12, \text{-}0.158, 0.031] \tag{1.4}$$

The results show that the PV output sensitivity with respect to the I_{ph} and η is close to one. As a consequence, few percentage variation of I_{ph} and η is reflected in a significant variation of PV power. R_{sh} and I_{sat} have lower impact, less than one order of magnitude. Sensitivity to R_s is somewhere in between. This means that a small variation of these parameters can be tolerated since the corresponding degradation process is not yet detrimental.

1.4 Methods for the on-line diagnosis of PV systems

The literature overview provided in this section is limited to the approaches which are suitable to be implemented on board to the PV system, thus by using only electrical and environmental measurements provided by on-field sensors. Much more expensive and complex approaches, as for example PV diagnosis based on electroluminescent or thermographic images of the PV panels, achievable by using unmanned aerial vehicle [51] [52], are out of topic of this thesis work.

At present, there are many studies related to PV fault detection and diagnosis, but most of them are focused at the PV system level. In [53], different methods are reviewed and discussed in details by putting into evidence their feasibility, complexity, cost-effectiveness and generalisation capability for large-scale integration. In [54] the discussion is focused on the use of artificial intelligence (AI) and internet of things (IoT) for remote sensing of solar photovoltaic systems to improve the PV diagnosis.

The use of photovoltaic models in combination with AI methods has been already proposed in literature for PV faults detection. In [55] an Artificial Neural

Networks (ANN) is firstly trained with numerical simulation, provided by a PV model, for classification and isolation of eight types of faults, then used with on field measurements to identify possible faulty operating conditions. A Field Programmable Gate Array (FPGA) implementation of the proposed method is also proposed in the paper for the online operation. In [56] the kernel based extreme learning machine (KELM) is employed to train the single hidden-layer feed-forward neural network (SLFN) to classify the degradation fault, short-circuit fault, open-circuit fault and partial shading faults in a PV array. The SLFN needs as inputs electrical values taken from the $I-V$ curve, environmental conditions and the SDM parameters previously calculated starting from the whole $I-V$ curve. An ANN with radial basis function (RBF) requiring only irradiance and PV output power as input has been developed in [57]. The results obtained through the testing of the developed ANN on a PV installation of 2.2 kW capacity, provided an accuracy of 97.9% in faults identifications. In this case no model has been used but it took long-term data measurements for reproducing on the PV installation different kind of faults.

The ANNs training phase usually require a large number of observations, which are not always available. This problem might be mitigated by using probabilistic neural networks (PNNs), that learn on-line with a small number of observations [58, 59].

The explosion of the IoT technologies is expected to enable, with an acceptable additional cost, the diagnosis at PV panel level. Moreover, by exploiting edge computing sensors [60], it will be possible to elaborate on site the data and to transmit to the final user only synthetic information related to the state of health of each PV module. Module-level monitoring devices are already available in the market for monitoring and controlling the single PV panel, thus improving the system performance and the planning of system's operation and maintenance activities [61]. Such devices are also able to perform the $I-V$ curve tracing but the analysis of these data is in charge to the final user. Nevertheless, the offline data analysis is time consuming and requires an operator with a specific PV background. Moreover, the types of faults and degradation mechanisms that can be identified are very limited. To solve this drawback, in [62] it has been proposed an automatic fault detection method that elaborates online the $I-V$ curves of PV panels. The diagnosis is focused on the identification of current mismatch due to the partial shading, hot spot, and cell cracks. The method calculates the concavity and convexity along the $I-V$ curves because the three analysed faults produce steps on the I–V curve, thus not trivial data processing is required for proper detection of the occurring fault.

1.5 Frequency domain analysis

1.5.1 PV dynamic models

A PV solar cell is essentially a p–n junction modelled using resistance, capacitance, and inductance. Figure 1.5 shows the equivalent small-signal ideal dynamic circuit composed of R_d dynamic resistance of diode (Ω), R_s series resistance (Ω), R_{sh} shunt resistance (Ω), C_d diffusion capacitance (F), and C_t transition capacitance (F).

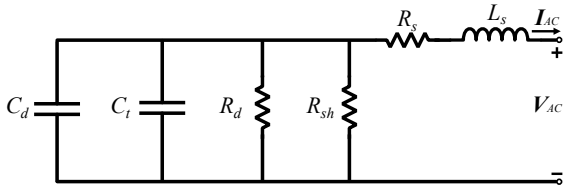

Figure 1.5. Ideal small-signal PV dynamic model

In the small–signal model, the DC components as the module photo-induced current and the diode polarisation current are ignored. Thus, the frequency representation of the AC dynamic circuit is done through the equivalent impedance (Z_{eq}) as a function of the frequency [63].

$$Z_{eq}(\omega) = R_s + \frac{R_p}{(\omega R_p C_p)^2 + 1} + j\left[\omega L_s - \frac{\omega R_p^2 C_p}{(\omega R_p C_p)^2 + 1}\right] \tag{1.5}$$

where C_p is equal to the parallel between C_d and C_t and R_p the parallel between R_d and R_{sh} [64], [65].

The effect of the inductance must be taken into account, especially by the impact of the wires and connectors the system must utilize. These components suppose stronger values compared to the internal inductance cell effect and could increase to module/panel level [64]. Previous works [66, 67, 68, 69, 70] shown that the AC small-signal electrical model shown in figure 1.5 fits in a good way the impedance values obtained for photovoltaic devices. The value is generally determined using time-domain or frequency-domain techniques [65].

In general, EIS spectra do not exhibit a perfect semicircle due to non–ideal capacitances inside the PV p-n junctions. [66, 67, 71]. Therefore, the use of the Constant Phase Element (CPE), especially for Si-based technologies, helps to adjust some deviations of internal processes leading to modelling the experimental impedance data using the circuit of Fig. 1.6, which is described by equation (1.6). Moreover, for the frequency range adopted in this thesis work, the AC model of a module is the same as for a single cell [67, 72].

Besides, according to [73], R_0 represents the series ohmic losses, R_1 the junction resistance, and the junction capacitance (composed of a transition C_t capacitance and a diffusion C_d capacitance) is represented by the CPE element.

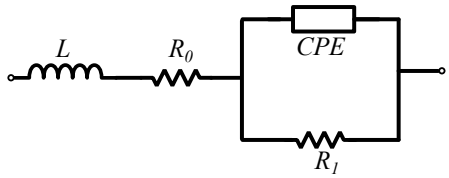

Figure 1.6. Dynamic model with a constant phase element (CPE).

$$Z_{eq}(\omega) = j\omega L + R_0 + \frac{R_1}{[(j\omega)^{\beta} Q R_1 + 1]} \tag{1.6}$$

The impedance of the CPE has a particular interpretation. The β element can have values from 0 to 1. If β tends to 1, CPE is a pure capacitance. If β tends to 0, CPE is a pure resistor. From [74] the value of the equivalent capacitor of the CPE element can be calculated with equation (1.7).

$$C = Q^{\left[\frac{1}{\beta}\right]} R_1^{\left[\frac{1}{\beta}-1\right]} \tag{1.7}$$

1.5.2 Electrochemical Impedance Spectroscopy

Electrical Impedance Spectroscopy (EIS) methodology is a well–established technique to characterize electrochemical devices (e.g. batteries, fuel cells, supercap) in the frequency domain [70],[75]. This method injects a small perturbation, with a variable frequency, superimposed to the system operating point and the impedance spectra is calculated in that operating point, as shown in figure 1.7. The EIS must be performed by using small voltage or current perturbations, thus the response of the system under test is considered linear. Since the perturbation amplitude is very small, the EIS technique should be not invasive and applicable online during the normal operation of the system under test.

In potentiostatic mode, a sinusoidal voltage perturbation is superimposed to the system operation point $v(t) = V_p + V_0 \sin(\omega t)$ with amplitude V_0 and angular frequency ω by producing a current response $i(t) = I_p + I_0 \sin(\omega t + \theta)$ with amplitude I_0 and the same angular frequency ω, but with a phase shift equal to θ. In galvanostatic mode the perturbation is imposed on the current operating point and the voltage response is measured. The sinusoidal perturbation might be

replaced with more complex stimulation signal to speed up the EIS measurements process [76, 77].

For both techniques, the impedance $Z(\omega)$ is calculated as a complex function of the complex frequency ω ($\mathbb{C} \to \mathbb{C}$) defined as the ratio between the Laplace transform $V(\omega)$ of the input and the Laplace transform $I(\omega)$ of the output:

$$Z(\omega) = \frac{V(\omega)}{I(\omega)} = \frac{\mathscr{L}\{v(t)\}}{\mathscr{L}\{i(t)\}} = \frac{V_0}{I_0} \cdot e^{-j\theta} = |Z(\omega)| \cdot e^{-j\theta} \tag{1.8}$$

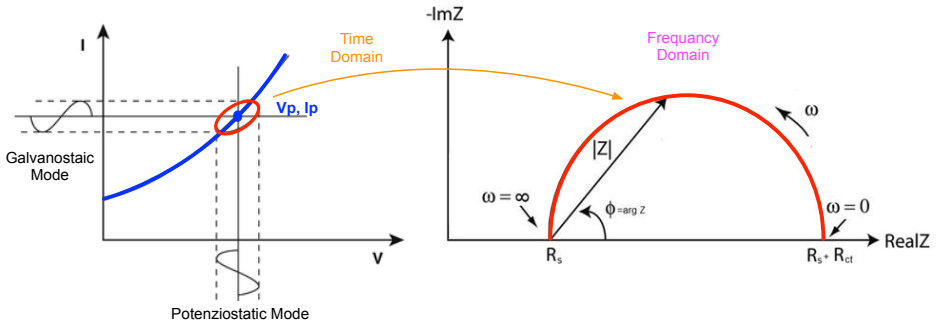

Figure 1.7. Identification of the impedance spectra through a sinusoidal stimulation of V_p, I_p

The frequency range and the amplitude of the small signal are the main parameters to configure for performing the EIS methodology.
As shown in Table 4.43, previous works have fixed these values from 0.01 Hz up to 100 kHz for the frequency and usually 100 mV value is used for the voltage amplitude [68, 73, 78]. In this thesis work, the frequency range was fixed from 10 Hz up to 50 kHz because the PV module under test responds successfully in this range. Details on the EIS measurement equipment and panels under test are reported in section 4.3.2.

Fig. 1.8 shows the measured impedance in the complex plane and through the Bode diagram. Some basic characteristics can be straightforward associated to the circuit in Fig. 1.6. At low frequency ($\omega \to 0$) the impedance value is given by the sum of the series ohmic losses and the junction resistance. At high frequency, the impedance value cross the x–axis and goes down almost vertically indicating that the inductive effect is dominating. This is also evident in the Bode diagram of Fig. 1.8 where, at high frequency, a 180° of phase change can be justified only by an inductive effect. Indeed, the measured impedance shows an almost straight line at high frequency, as highlighted by the dashed vertical asymptote in Fig. 1.8(a) indicating the presence of an inductive effect, mainly due to the cables and connectors used for the experimental setup.

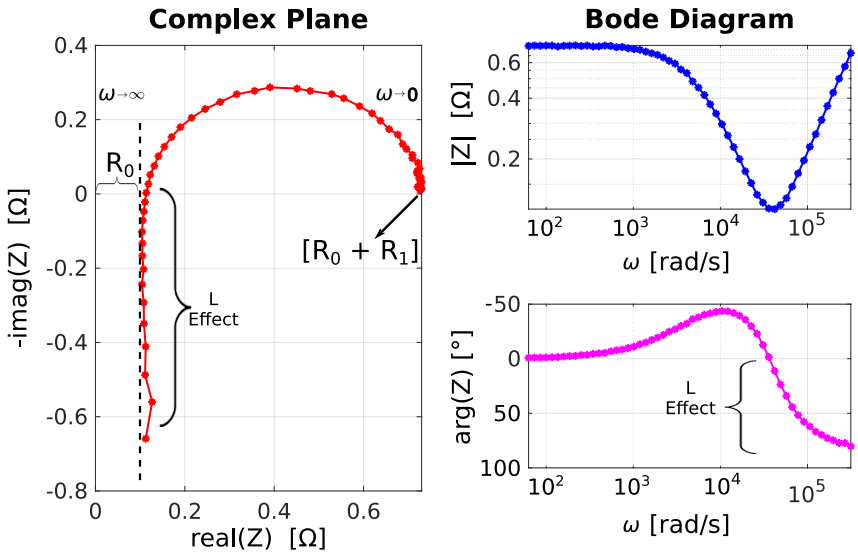

Figure 1.8. (a) Complex plane, (b) Bode magnitude diagram, and (c) Bode phase diagram of the impedance values of the PV panel.

The asymptote is described by the equation $Z(\omega) = R_0 + j\omega L$ which is the vertical boundary for the impedance spectrum in the Complex plane. The variation of L affects the resonance frequency, that is the frequency where the impedance spectrum crosses the real axis close to the asymptote. The resistance R_0, since it is not depending on the frequency, only produces an horizontal translation of the impedance spectrum without modifying its shape.

For the stimulation frequency range employed in the measurement setup, the solar cells introduce mainly a capacitive effect due to their internal p–n junctions. They exhibit inductive behavior for stimulation frequencies beyond 1 MHz, as indicated in [64].

To confirm that the inductive effect visible in the impedance spectra of Fig. 1.8 is dominated by parasitic effects, the measurement setup has been tested on a set of calibrated resistors within the same frequency range used for the PV measurements and at the same testing conditions. The same inductive effect was measured in each test with no significant error in the estimation of the calibrated resistors. These tests corroborate that the inductive effect is mainly due to the MC4 connectors used in commercial PV applications. Indeed, authors in [79], [80], and [81] also reaffirm the presence of inductive parasitic effects generated by PV connectors and wires, which is visible at the highest frequencies of the frequency stimulation range. Although the estimated inductance L is not directly related to the solar cells it is a further parameter that can be monitored for detecting degradation in the cabling of PV panels. It is also worth to note that such parasitic

effect does not appear in laboratory setup where the measurement equipment is directly connected to the PV cells by using short cables [82].

1.5.3 Impedance spectroscopy on photovoltaics (PV) panels

EIS applied to PV systems is relatively new, but, despite it, good preliminary results have been reached for the last few years, especially for the diagnosis of degradation processes [67, 68]. One common limitation of these previous works is their on–field applicability, because they are under controlled conditions (irradiance and temperature) with single solar cells. Some of them have used small solar panels, but still in a laboratory environment.

For instance, in Oprea et al [78], the EIS technique was implemented for determining Potential-Induced Degradation (PID) effects over a residential PV plant of 9.36 KW. The PID effect was confirmed by employing I-V and electroluminescence measurements. To assess the level of degradation the series resistance (R_s), shunt resistance (R_{sh}), and the equivalent capacitance were approximated. The results showed the connection between the element values and the level of degradation caused by the PID.

In Varnosfaderani and Strickland [83] the EIS technique is implemented in a small-scale PV system with no additional electronic devices. Here the DC-DC power electronic converter was utilized for generating and injecting a small AC signal into the PV module without affecting his normal operation. The research showed good accuracy in the impedance values calculated between the online test against laboratory measurements. Thus, were shown some of the benefits and applicability of the technique in online implementation.

Finally, in Katayama et al [68] some commercial polycrystalline silicon solar cells were used to analyze mechanical stress, interconnection ribbon disconnection, and potential-induced degradation processes. The cells were analyzed in normal conditions, and subsequently, degraded with the aforementioned degradation processes. The use of the EIS technique allowed calculating the impedance values for building the model and get the Nyquist plot based on the series resistance, shunt resistance, and equivalent capacitance. The experimental results showed the variability of the elements that composed the model and showed a clear way for differencing the three degradation processes. These works have shown good performance and promising results on using the EIS methodology as a tool for diagnosis in PV modules. Nevertheless, most of them were made at cell level using laboratory tests for demonstrating novelties and benefits.

Table 4.43 summarizes the main information of different methods proposed in the literature for analyzing the PV dynamic response. The techniques are mainly devoted to the performance evaluation of PV cells for validating the

PV manufacturing process, for studying physical phenomena occurring inside the cell, for identifying parameters of dynamic models, as well as for the analysis of degradation and fault detection inside PV cells and modules. Usually, the testing conditions refer to PV cells or modules operating in dark conditions or under controlled irradiance G and temperature T. Table 4.43 also shows the ranges of the stimulation frequency used for testing the PV cells and modules made with single–crystalline (sc–Si) and multi–crystalline (mc–Si) silicon PV technologies.

In this thesis the application of the EIS technique on PV panel operating in MPP in outdoor conditions will be proven. The results are deeply discussed in chapter 4.

Table 1.1. Preliminary EIS studies on solar PV cells/modules

Characteristic	**Reference**												
	[84]	[79]	[85]	[86]	[80]	[87]	[72]	[68]	[65]	[78]	[67]	[88]	[81]
Testing Condition													
Dark	•	•					•	•	•	•	•		
Controlled G and T	•	•	•	•	•	•	•	•					•
Outdoor conditions												•	
Technology													
sc-Si	•	•	•		•	•	•		•	•	•		
mc-Si				•				•	•			•	•
Technique													
Square wave signal	•												
Impedance Spectroscopy		•	•	•	•	•	•	•	•	•	•		
Reflectometry												•	•
Objective													
Physics							•						
Manufacturing							•						
Modelling	•	•	•	•	•	•							
Fault detection									•			•	•
Degradation analysis								•		•	•		
Frequency Range													
1Hz-30kHz	•												
1Hz-100kHz			•					•	•		•		
0.1Hz-100kHz				•									
1Hz-1MHz					•								
150Hz-200kHz						•							
42Hz-5MHz							•						
20Hz-100kHz										•			
0.01Hz-1MHz		•											
20Hz-200kHz													•
PV level													
Cell	•	•	•	•	•	•	•	•					•
Module/Array									•	•	•	•	•

Parameters Extraction of Single Diode Model for Degraded Photovoltaic Modules

2.1 Introduction

The research activity shown in this chapter focuses on the *on–line* estimation of the SDM parameters. As it is shown in [43] or in [89], many papers propose simple procedures or explicit equations for calculating the parameters of the SDM model [26, 90, 91, 92, 93, 94, 95, 96, 97]. Such approaches are potentially suitable to be easily integrated in the *on–line* diagnostic function. Nevertheless they are tested by using data coming from the PV panel datasheets or by using experimental I–V curves acquired in normal operating conditions, thus by validating the identification methods only in non–degraded conditions.

The main contribution of this work is aimed at investigating the reliability of the aforementioned explicit methods, also said *direct methods*, to identify the parameters of the photovoltaic panel that are indicators of possible degradation phenomena, in particular the internal series and parallel resistances. In other words, the goal is to study the reliability of such methods when they are used for diagnostic purposes.

Among all the explicit approaches for parameter identification of the SDM model, four methods have been selected to be compared and analysed (all of them based on a reduced set of simple and direct formulas). By referring to the classification given in [43], two methods have been selected among the ones that use only information as given in the PV panel datasheet, and two methods based on the slopes calculated in the short–circuit current and open–circuit voltage.

In order to have a reference value as accurate as possible for the identified parameters, a non–explicit method based on an iterative fitting procedure has been

also applied. All these methods will be tested by using measurements from several experiments in which different levels of degradation are emulated by connecting in series with the photovoltaic module external resistances with different nominal values. The objective is to study the capability of the methods to detect this simulated degradation effect added to the PV module that is operating for several days under outdoor conditions.

The chapter is organised as follows: Section 2.2 describes briefly the selected methods used for identifying the five parameters of the SDM model. Section 2.3 starts referring to the experimental system used for acquiring the outdoor I–V curves of the photovoltaic module under study. In addition, the procedure to select I–V curves and estimation of the main electrical parameters are explained. The section ends describing how further degradation has been emulated by connecting additional resistances in series. Section 2.4 is aimed at showing and comparing the results obtained by the different methods in the nominal operating conditions by using the numerical curve-fitting approach as the reference. The capability of these approaches for reconstructing the measured I–V curve is also analysed. In Section 2.5, the behaviour of the identification methods with I–V curves measured in degraded condition is studied. Finally, in Section 2.6, the main conclusions of this work are summarised.

2.2 Photovoltaic model and parameter identification methods

The four explicit methods selected among the most promising ones analysed in [43] are briefly recalled in the subsections 2.2.1–2.2.4. Since there is no way to perform a direct measurement of the five parameters of the SDM model, in order to have a reference value for each parameter, a non–explicit method has been used to have a reference value for each parameter. Following the classification proposed by [43], the fifth approach lies within the *"optimisation methods"*, because it uses all the measured points of the I–V curve in order to construct an error function to be minimised by means of an iterative procedure. This method is formalised in section 2.2.5.

2.2.1 Explicit equations based on the LambertW function

This method exploits the Lambert W–function [98] for deriving the set of explicit equations allowing a fast calculation of the SDM parameters. In [22, 41, 99] all details about this approach are provided:

$$I_{ph} \simeq I_{\mathrm{SC}} \tag{2.9}$$

$$E_g(T) = E_{g0} - \frac{a \cdot T^2}{T + b} \tag{2.10}$$

$$I_0 = I_{\mathrm{SC}} \cdot \exp\left\{\left(\frac{V_{\mathrm{OC}}}{V_{\mathrm{OC}} - \beta \cdot T}\right) \cdot \left(\frac{\alpha \cdot T}{I_{\mathrm{SC}}} - 3 - \frac{E_g(T)}{V_t}\right)\right\} \tag{2.11}$$

$$A = \frac{V_{\mathrm{OC}}}{\ln\left(\frac{I_{\mathrm{SC}}}{I_0} + 1\right)} \qquad B = \frac{V_{\mathrm{Pmax}} \cdot (V_{\mathrm{Pmax}} - 2 \cdot A)}{A^2} \tag{2.12}$$

$$n = \frac{A}{N_s \cdot V_t} \tag{2.13}$$

$$C = \frac{V_{\mathrm{Pmax}} \cdot (2 \cdot I_{\mathrm{Pmax}} - I_{ph})}{A \cdot I_0} \quad x = W_0\{\, C \cdot \exp(B)\} - B \tag{2.14}$$

$$R_s = \frac{x \cdot A - V_{\mathrm{Pmax}}}{I_{\mathrm{Pmax}}} \tag{2.15}$$

$$R_{sh} = \frac{x \cdot A}{I_{ph} - I_{\mathrm{Pmax}} - I_0 \cdot (\exp(x) - 1)} \tag{2.16}$$

where α is the current–temperature coefficient of the module expressed in AK^{-1}, β is the voltage–temperature coefficient in VK^{-1} and $W_0\{\,\cdot\,\}$ is the main branch of the Lambert$-W$ function. Finally $E_g(T)$ is the band gap energy (eV) of the semiconductor at temperature T (K); the constants E_{g0} (band gap energy at 0 K), a and b depend on the material. In the case of single–crystalline silicon (sc-Si) the values are $E_{g0} = 1.16$ eV, $a = 7 \times 10^{-4}$ eV K^{-1} and $b = 1100$ K [100]. This approach will be identified in the following as ***LambertW method***.

2.2.2 Explicit equations by using the Serial–Parallel Ratio

In [95, 96] it has been shown that the 5–parameter SDM can be scaled down to 4–parameter SDM without losing significant precision if only one resistance is neglected. The method allows to classify the PV modules into two groups on the basis of the value assumed by the performance indicator named Serial–Parallel–Ratio (SPR):

$$I_{ph} \simeq I_{\mathrm{SC}} \qquad \gamma_i = \frac{I_{\mathrm{Pmax}}}{I_{\mathrm{SC}}} \qquad \gamma_v = \frac{V_{\mathrm{Pmax}}}{V_{\mathrm{OC}}} \tag{2.17}$$

$$r = \frac{\gamma_i \cdot (1-\gamma_v)}{\gamma_v \cdot (1-\gamma_i)} \qquad SPR = (1-\gamma_i) \cdot \exp(r) \tag{2.18}$$

$$\text{Case (A)}: \; SPR > 1 \Rightarrow \begin{cases} R_{sh} = \infty \\ \delta = \ln(1-\gamma_i) \\ R_s = \dfrac{V_{\mathrm{OC}}}{I_{\mathrm{SC}}} \cdot \dfrac{\dfrac{\gamma_v}{\gamma_i} \cdot (1-\gamma_i) \cdot \delta + (1-\gamma_v)}{(1-\gamma_i) \cdot \delta + \gamma_i} \\ A = \dfrac{I_{\mathrm{Pmax}} \cdot R_s - V_{\mathrm{OC}} + V_{\mathrm{Pmax}}}{\delta} \\ I_0 = I_{ph} \cdot \exp\left(\dfrac{-V_{\mathrm{OC}}}{A}\right) \end{cases} \tag{2.19}$$

$$\text{Case (B)}: \; SPR < 1 \Rightarrow \begin{cases} R_s = 0\,\Omega \\ \lambda_1 = \dfrac{(1-\gamma_v) \cdot (2 \cdot \gamma_i - 1)}{(1-\gamma_i) \cdot (\gamma_i + \gamma_v - 1)} \\ \lambda_2 = \dfrac{\gamma_v}{1-\gamma_i} \\ \omega = W_{-1}\{-SPR \cdot \lambda_1 \cdot \exp(-\lambda_1)\} \\ R_{sh} = \dfrac{V_{\mathrm{OC}}}{I_{\mathrm{SC}}} \cdot \dfrac{\lambda_2 \cdot \omega + \lambda_1}{\omega + \lambda_1} \\ A = \dfrac{-V_{\mathrm{OC}} + V_{\mathrm{Pmax}}}{\ln\left\{\dfrac{(I_{\mathrm{SC}} - I_{\mathrm{Pmax}}) \cdot R_{sh} - V_{\mathrm{Pmax}}}{I_{\mathrm{SC}} \cdot R_{sh} - V_{\mathrm{OC}}}\right\}} \\ I_0 = \left(I_{ph} - \dfrac{V_{\mathrm{OC}}}{R_{sh}}\right) \cdot \exp\left(\dfrac{-V_{\mathrm{OC}}}{A}\right) \end{cases} \tag{2.20}$$

where $W_{-1}\{\cdot\}$ is the lower branch of the Lambert$-W$ function and n could be calculated as in the previous methods using (eq 2.13). This approach will be identified in the following as ***SPRatio method***.

2.2.3 Explicit equations based on the Phang's method

The method proposed in [90] uses the values of the slopes at the short–circuit and open–circuit points (R_{sh0} and R_{s0} respectively) as starting points. The regression procedures to estimate these values can be performed over the set $\{V_i, I_i\}$ or over $\{I_i, V_i\}$:

$$R_{s0} = -\left.\frac{dV}{dI}\right|_{I=0} = -\frac{1}{\left.\frac{dI}{dV}\right|_{V=V_{\mathrm{OC}}}} \tag{2.21}$$

$$R_{sh} = R_{sh0} = -\left.\frac{dV}{dI}\right|_{I=I_{\mathrm{SC}}} = -\frac{1}{\left.\frac{dI}{dV}\right|_{V=0}} \tag{2.22}$$

$$B = I_{\mathrm{SC}} - \frac{V_{\mathrm{Pmax}}}{R_{sh}} - I_{\mathrm{Pmax}} \qquad C = I_{\mathrm{SC}} - \frac{V_{\mathrm{OC}}}{R_{sh}} \tag{2.23}$$

$$A = \frac{V_{\mathrm{Pmax}} + R_{s0} \cdot I_{\mathrm{Pmax}} - V_{\mathrm{OC}}}{\ln(B) - \ln(C) + \frac{I_{\mathrm{Pmax}}}{C}} \tag{2.24}$$

$$D = \exp\left(-\frac{V_{\mathrm{OC}}}{A}\right) \qquad I_0 = C \cdot D \qquad R_s = R_{s0} - \frac{A}{I_0} \cdot D \tag{2.25}$$

$$I_{ph} = I_{\mathrm{SC}} \cdot \left(1 + \frac{R_s}{R_{sh}}\right) + I_0 \cdot \left[\exp\left(\frac{I_{\mathrm{SC}} \cdot R_s}{A}\right) - 1\right] \tag{2.26}$$

Finally, for the estimation of the diode ideality factor n it is possible to use (eq 2.13). This set of equations will be noted as ***Phang method***.

2.2.4 Explicit equations based on the Toledo's method

The method proposed in [94] rewrites the SDM equation given in (eq 1.1) differently. In this case, the general equation for the SDM is expressed as:

$$I = A - B \cdot (C^V \cdot D^I - 1) - E \cdot V \tag{2.27}$$

The method needs the set of values at the short–circuit point and three additional points of the *I-V* curve $\{(V_1, I_1), (V_2, I_2), (V_3, I_3)\}$. These values are the starting points for calculating the model of five parameters. Although the choice of these points could be arbitrary, the author suggests choosing three set of points with voltage greater than the maximum power-point and uniformly distributed. In the analysis carried out in this chapter, these additional three points are the maximum power point, the open-circuit point and the maximum of the $\alpha-$power function [32], that taking ($\alpha = 10$) is a point between V_{Pmax} and V_{OC}. The proposed set of equations is:

$$E = -\left.\frac{dI}{dV}\right|_{V=0} = -\frac{1}{\left.\frac{dV}{dI}\right|_{I=I_{\mathrm{SC}}}} \tag{2.28}$$

$$F_1 = \ln(I_{\mathrm{SC}} - E \cdot V_1 - I_1) \tag{2.29}$$
$$F_2 = \ln(I_{\mathrm{SC}} - E \cdot V_2 - I_2) \tag{2.30}$$
$$F_3 = \ln(I_{\mathrm{SC}} - E \cdot V_3 - I_3) \tag{2.31}$$

$$D = \exp\left\{\frac{(F_1 - F_2) \cdot (V_2 - V_3) - (F_2 - F_3) \cdot (V_1 - V_2)}{(I_1 - I_2) \cdot (V_2 - V_3) - (I_2 - I_3) \cdot (V_1 - V_2)}\right\} \tag{2.32}$$

$$C = \exp\left\{\frac{F_2 - F_3 - (I_2 - I_3) \cdot \ln(D)}{V_2 - V_3}\right\} \tag{2.33}$$

$$B = \exp\left\{F_1 - V_1 \cdot \ln(C) - I_1 \cdot \ln(D)\right\} \tag{2.34}$$

$$A = I_{\mathrm{SC}} - B \tag{2.35}$$

$$G = \frac{\ln(C)}{\ln(C) - E \cdot \ln(D)} \tag{2.36}$$

$$I_{ph} = A \cdot G \qquad I_0 = B \cdot G \tag{2.37}$$

$$R_s = \frac{\ln(D)}{\ln(C)} \qquad R_{sh} = \left(\frac{1}{E} - R_s\right) \tag{2.38}$$

$$n = \frac{1}{N_s \cdot V_t \cdot \ln(C)} \tag{2.39}$$

2.2.5 Identification method based on curve fitting

The algorithm used to find the optimal values of the SDM parameters is widely known as trust–region–reflective. A comprehensive guide about this family of techniques can be found in [101].

There is a specific type of trust–region algorithm able to work when the search space is bound to a feasible region. This means that users can define an interval for each parameter to estimate in addition to the required initial point. Fixing an appropriate set of lower and upper limits is not an easy task but it is possible to find some proposals in the literature that are suitable for the SDM [102, 103]. Specifically, the second of those works defines a feasible region taking into account the information from a large database of photovoltaic modules and their features. Table 2.2 presents the values of these intervals, that have been used in this chapter. In addition, the table provides the start point that has been selected for each parameter. The initial values for R_s and R_{sh} are the slopes of the I-V curve in V_{oc} and I_{sc} respectively. They are calculated as shown in section 2.2.6. For I_{ph} the initial point is I_{sc} due to their high correlation. For n and I_0, without any additional information, the centres of the proposed intervals have been adopted as the starting points.

Table 2.2. Interval and start points for the five SDM parameters

	Lower limit	Upper limit	Start point
$I_{ph}[A]$	$1/12$	12	I_{sc}
$I_0[nA]$	1×10^{-3}	$1 \times 10^{+4}$	$5 \times 10^{+3}$
$n[/]$	1	2	1.5
$R_s[\Omega]$	0	100	R_{s0}
$R_{sh}[\Omega]$	1	5×10^4	R_{sh0}

The procedure minimises the following objective function, it describes the PV generator as introduced in the equation (1.1):

$$f = I_{ph} - I_{sat} \cdot [e^{(\frac{V_{pv} + I_{pv} \cdot R_s}{\eta \cdot n_s \cdot V_t})} - 1] - [\frac{V_{pv} + I_{pv} \cdot R_s}{R_{sh}}] - I_{pv} \tag{2.40}$$

The trust–region algorithm integrated into the Optimisation Toolbox of Matlab [104] has been used in this thesis work. In the call to this function it is necessary to pass some important tuning parameters in order to ensure a successful execution. Among these input values, the maximum number of iterations (*maxIter*), the minimum tolerance in the search space (*tolX*) and the minimum tolerance in the target function (*tolFun*) have been settled. When any of these criteria is reached, the function stops its execution. It is worth to note that, due to the strong non-linearity of the SDM model, if the Matlab function uses default setting the convergence to the optimal solution is not assured. Table 2.3 shows the difference between the default values and the ones used in this work.

Table 2.3. Tuning parameters for the fitting procedure

	Default value	Used value
maxIter	400	2500
maxFunEvals	600	10000
tolX	1×10^{-6}	1×10^{-12}
tolFun	1×10^{-6}	1×10^{-12}

The numerical solving procedure provides not only an estimation for each parameter of the SDM model, but also a confidence interval around that value. In this analysis the confidence interval is referring to a confidence level of 99%, which means that with a probability of 0.99 the true value of the parameter is inside that interval. Error bars will be always attached to the plots referring to this method in order to visualise this confidence interval.

This approach will be identified in the following as ***Fitting method***.

2.2.6 Data extrapolation from experimental I-V curve

The typical experimental *I–V* curve is given by a sequence of discrete current-voltage pairs starting in some point close to the short–circuit current (I_{SC}) and finishing in another point close to open–circuit voltage (V_{OC}). However, neither I_{SC} nor V_{OC} values might be measured accurately during the on-line operation and both need to be estimated by linear interpolation. Even worse for (V_{Pmax}, I_{Pmax}) point, that should be detected by using a non–linear interpolation. For each *I–V* curve, the technique described in [105] is used to calculate notable

points and slopes. A brief description of this method is reported in the following. The measured point nearest to the $Y - axis$ is identified being its current value I_x and from the nearest one to the $X - axis$ we get also the voltage component V_y. Then a two–dimensional interval centred in I_x is made $[0,\ 20\% \cdot V_y] \times [I_x - 4\% \cdot I_x,\ I_x + 4\% \cdot I_x]$. The interpolation with all the points inside the interval allows us to determine I_{sc} and also the slope (dI/dV) at $I = I_{\text{sc}}$. Analogous, using linear interpolation again over the interval $[V_y - 10\% \cdot V_y,\ V_y + 10\% \cdot V_y] \times [-20\% \cdot I_x,\ 20\% \cdot I_x]$ the value of V_{OC} and the slope (dI/dV) when $V = V_{\text{OC}}$ are determined. Figure 2.9 and (eq 2.41) show the concept of the slopes and their relationship with the I–V curve. The values of I_{sc} and V_{oc} represent the cuts for the Y and X axes.

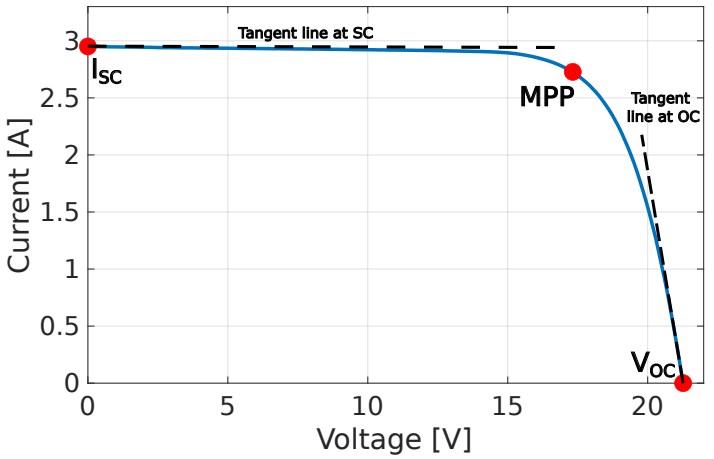

Figure 2.9. Slopes approximation on the I–V curve

$$R_{sh0} = -\frac{dV}{dI}\bigg|_{\text{SC}} \quad , \quad R_{s0} = -\frac{dV}{dI}\bigg|_{\text{OC}} \tag{2.41}$$

As suggested in [105], for estimating the maximum power point MPP, first the P–V curve is computed with $P_i = I_i \cdot V_i$. Then, the measured discrete point with the greatest value $P_z = I_z \cdot V_z$ is considered and all the experimental points $(V_i,\ P_i)$ verifying $P_i \geq 85\% \cdot P_z$ are selected for a fifth-degree polynomial interpolation. Next step is the derivation of the polynomial and the estimation of its real root inside the selected $X - range$. As a result, we can obtain a very good approximation of P_{max}, V_{Pmax} and I_{Pmax}.

The point where the PV module produce the maximum amount of energy, according to its physical properties and the relationship with the environmental variables (irradiance and temperature), is called Maximum Power Point (MPP). Under uniform environmental conditions, that means the same irradiance and

temperature on all the PV cells, the PV array exhibits a unique MPP.

It is worth to note that during the normal operation of a PV array, a control algorithm, called Maximum Power Point Tracking (MPPT), seeks to maintain the PV operating point as close as possible to the MPP for whichever irradiance and temperature conditions hitting on the PV array during the day.

Conventional MPPT algorithms have been adapted to identify the presence of multiple MPPs and tracks the global maximum (GMPP) [106]. However, in general, the modified approaches show high convergence time, require PV parameters to be updated periodically due to degradation of solar cells. Recent literature [107] also proposed MPPT controllers based on optimization meta-heuristic (or bio-inspired) algorithms for tracking the GMPP accurately. Despite high-steady-state efficiency, the performance is strongly dependent on the tuning parameters by leading to scalability issues [108].

It is important to keep in mind that the main research activities carried out in this thesis are focused to leave the PV panels operating in their MPP and at the same time acquire information on its status of health.

2.3 Experimental methodology

2.3.1 Measurement system and setup

In order to analyse and compare the explicit methods for SDM parameter identification, a PV measurement system has been configured for acquiring a large number of *I–V* curves under outdoor conditions. The equipment is installed on the roof of the *Department of Applied Physic II* at the University of Málaga (latitude: 36.715° N ; longitude: 4.478° W; elevation: 60 m). The PV module under test is the model *I–53* from the manufacturer *Isofotón* and its data-sheet specifications are summarised in Table 2.4. In [109] there is a detailed description of the measurement system used and a deep analysis of uncertainties. This equipment is able to acquire simultaneously the *I–V* curves and other external variables such as the in-plane irradiance G_{I} (solar power per square metre incident on the module plane) and the temperature of the module. The system is controlled by a software running in a personal computer in order to take automatic measurements every three minutes from the sunrise to the sunset. This software stores the measurements in a relational database and the data is available to be downloaded throughout a web page accessible from any computer in Internet. A full description of this application can be found in [110].

A first analysis has been done for calculating the actual SDM parameters to be assumed the baseline for estimating the capability of explicit methods to evaluate correctly additional degradation induced artificially. Indeed, to simulate further

Table 2.4. Isofotón I-53 main specifications

Parameter	Symbol	Value
Maximum Output Power at STC (W)	$P_{\text{max STC}}$	53
Voltage at Maximum Power (V)	$V_{\text{Pmax STC}}$	17.4
Current at Maximum Power (A)	$I_{\text{Pmax STC}}$	3.05
Short Circuit Current at STC (A)	$I_{\text{sc STC}}$	3.27
Open Circuit Voltage at STC (V)	$V_{\text{oc STC}}$	21.6
$I_{\text{SC STC}}$ temperature coefficient (AK^{-1})	α	0.001326
$V_{\text{OC STC}}$ temperature coefficient. (VK^{-1})	β	-0.07704
Series resistance (new module) (Ω)	R_s	0.288
Number of Cells in series	n_s	36
Cell Type	$sc-Si$	mono
Cell Area (cm^2)	A_c	104.4

levels of degradation in the real PV system, some resistors with different nominal values are connected in series to the PV module terminals. Figure 2.10 shows the electrical connections of the external resistors and measurement points.

The system has been programmed to perform several days of measurements for each different configuration, in order to ensure a perfect clear sky day for each of the experiments: 0 Ω (no additional series resistor), 0.3 Ω, 1 Ω and 1.5 Ω. The highest values of the additional series resistor have been selected according to the analysis given in [111] where it has been shown that R_s reaches values up to 2.3 Ω over an operation period of 20 year. The experiments have been performed during a period of time between June and July 2018.

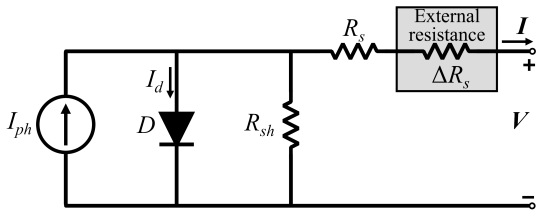

Figure 2.10. SDM with additional series resistance

2.3.2 Data pre–processing

As a result of the four performed experiments, there are available hundreds of I–V curves at different levels of irradiance and module temperature conditions, as well as with different additional series resistances.

Once all the experiments have been finished all the I–V curves have been

downloaded from the server and the files have been imported in Matlab workspace format for their further processing.

The first step is to remove all the measurements that do not satisfy the following criteria:

- The irradiance is measured before and after the measurement of each *I–V* curve. If the difference between both readings is greater than 5 Wm^{-2} the curve is rejected.
- All the measurements done with an irradiance lower than 700 Wm^{-2} have been removed because the single diode model is more accurate for high irradiance levels [112].
- In order to be sure that all the *I–V* curves have a suitable shape, a visual inspection of all selected curves has been done by using a plotting function in Matlab. If it is noticed that a particular curve presents a weird shape (due to a shadow or a measurement error), it is eliminated from the dataset.

The second step is the calculation of the notable points (0, I_{SC}), (V_{OC}, 0) and (V_{Pmax}, I_{Pmax}) from the experimental *I–V* curves in addition to the slopes of the curves in I_{SC} and V_{OC}. This process is detailed in the section **??**.

It is worth to note that the accurate calculation of such values from the experimental data is crucial for not introducing additional errors in the SDM parameter estimation, since the identification of SDM parameters by means of explicit methods is strongly dependent on *I–V* notable points and slopes.

Before analysing the results of the parameter identification methods, the effect of the additional series resistances on the experimental *I–V* is shown in Figure 2.11. The plotted *I–V* curves are at the same irradiance and temperature conditions. In the figure it is evident how the increase of the series resistance affects significantly the knee of the *I-V* curves where is located the maximum power point and the slope in right part of the *I-V* curves.

2.4 Comparison of the identification methods in nominal conditions

The starting point for the comparative analysis of the methods is to estimate the five parameters at fixed conditions of in–plane irradiance and module temperature. From the pre-processed dataset of measured *I–V* curves, only those with cell temperature around a fixed value have been selected (a range of [43,44] °C has been chosen in order to maximise the number of measurements).

The set of *I–V* curves is then identified with $\{C[i]\}_{i=1}^{r}$ and their respective measurements of irradiance and module temperature are $\{G_{\mathrm{I}}[i]\}_{i=1}^{r}$ and $\{T[i]\}_{i=1}^{r}$

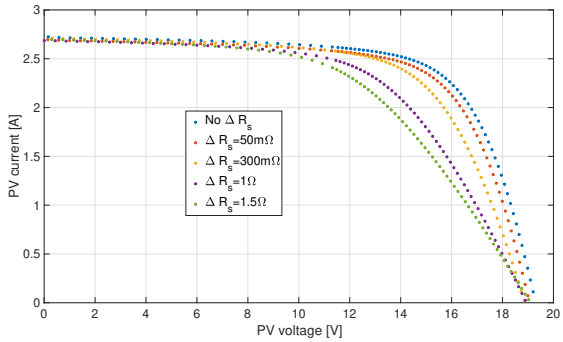

Figure 2.11. Experimental curves of PV panel under study with different added series resistances

respectively, r is the number of selected curves. Over each curve $C[i]$ it is possible to run all the proposed methods (let $m \in$ {Fitting, Phang, SPRatio, Toledo, LambertW}) by providing the five values vector:

$$\{I_{ph}[i], I_0[i], n[i], R_s[i], R_{sh}[i]\}^{(m)} \qquad i \in [1, ..., r] \tag{2.42}$$

The restricted range of temperature allows to make negligible the dependency of SDM parameters on temperature since it is almost constant. Differently, the measured irradiance range has a wide variation because it only fulfils the criterion $G_{\mathrm{I}} \geq 700$ Wm^{-2}, thus a linear regression analysis is applied on the calculated SDM values in order to account the dependency of parameters with respect to in-plane irradiance G_{I}. The regression analysis is performed for all the explicit methods shown in Section 2.2. The results of the fitting method are considered as reference.

For all the methods, the dark saturation current I_0 and diode ideality factor n do not exhibit significant dependency on the irradiance, since the *coefficient of determination*, usually denoted with R^2, is very low. In general, a high R^2 value indicates that the regression model fits with the experimental data. In [113], it is stated that a value of R^2 lower than 0.25 means that between the studied variables there is a very low or no correlation. The parameters I_0 and n are considered not dependent on the irradiance G_{I} because this condition occurs in both cases.

For the other three parameters (I_{ph}, R_s and R_{sh}), the *coefficient of determination* and the corresponding equations of regression lines are reported in Figures 2.12 and 2.13. The figures also show the SDM parameter values calculated with each method by using the selected I–V experimental curves. The regression lines have been expressed as function of the standard irradiance condition $\mathrm{G_{STC}} = 1000$

Wm^{-2} as follows:

$$\begin{aligned} I_{ph} &= \delta_{I_{ph}}^{(m)}(G_\mathrm{I} - \mathrm{G_{STC}}) + I_{ph\ \mathrm{STC}}^{(m)} \\ R_s &= \delta_{R_s}^{(m)}(G_\mathrm{I} - \mathrm{G_{STC}}) + R_{s\ \mathrm{STC}}^{(m)} \\ R_{sh} &= \delta_{R_{sh}}^{(m)}(G_\mathrm{I} - \mathrm{G_{STC}}) + R_{sh\ \mathrm{STC}}^{(m)} \end{aligned} \tag{2.43}$$

where, for a specific method m, $\delta_{I_{ph}}^{(m)}$, $\delta_{R_s}^{(m)}$ and $\delta_{R_{sh}}^{(m)}$ are the angular coefficient of the regression lines and $I_{ph\ \mathrm{STC}}^{(m)}$, $R_{s\ \mathrm{STC}}^{(m)}$ and $R_{sh\ \mathrm{STC}}^{(m)}$ are the offsets of these lines at $G_\mathrm{I} = \mathrm{G_{STC}}$

By referring to the Figure 2.12, it is evident that the estimated I_{ph} values are strongly dependent on G_I since R^2 is almost equal to 1 for each method. This is an expected result because the photo-generated current depends linearly on the irradiance reaching the PV panel surface.

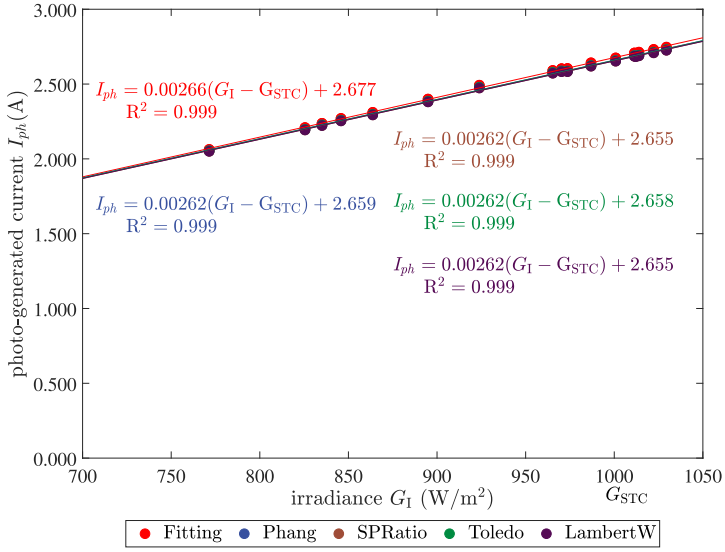

Figure 2.12. I_{ph} estimation at different irradiance conditions with respective regression lines

The regression lines of Figure 2.13 show that the series and parallel resistance dependency on the irradiance is also affected by the applied identification method. Indeed, by considering the results of the fitting method as reference, the other methods exhibit different angular coefficients and offsets. In some cases, the coefficient of determination R^2 is too low, meaning a non-dependency on G_I.

In addition to the regression analysis, the comparison of the calculated values by the explicit methods with respect to the results of the fitting method put into evidence that *Phang* method gives better results in R_s identification, while

LambertW method is more effective in the R_{sh} identification. It is also evident that for the *SPRatio* method the identified R_s is always zero because $SPR < 1$.

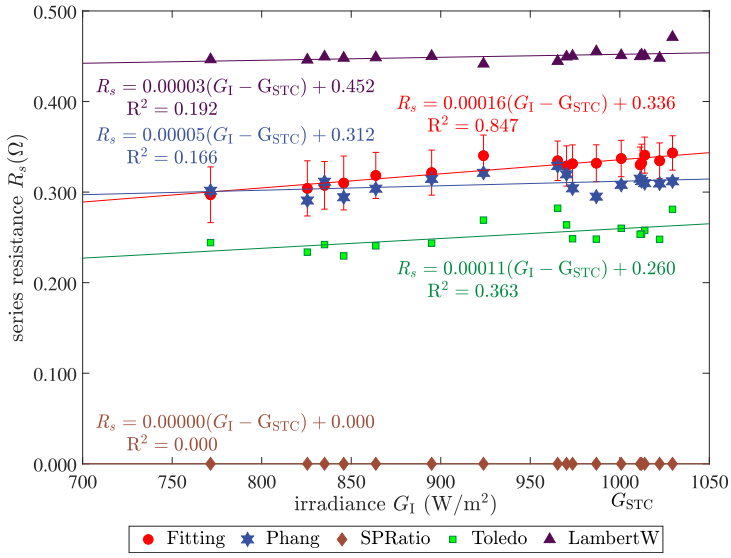

(a) R_s estimation with respective regression lines

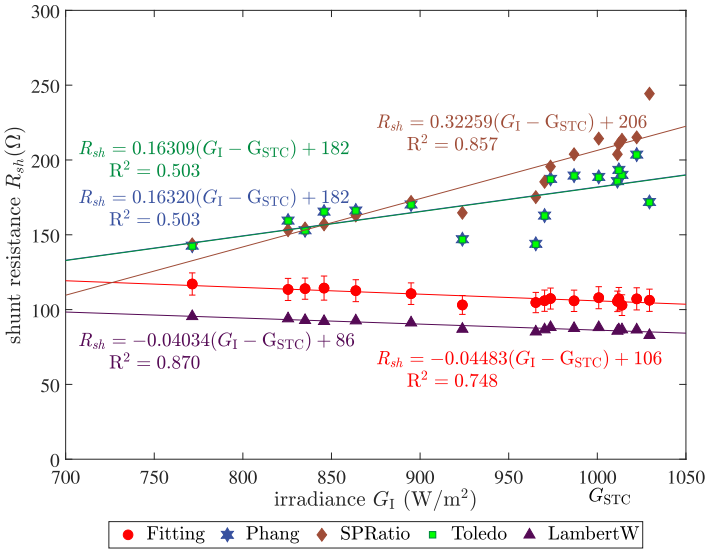

(b) R_{sh} estimation with respective regression lines

Figure 2.13. Estimations of series and parallel resistances at different irradiance conditions by using the selected identification methods

Table 2.5 collects the average values $\mu(\cdot)$ and the standard deviation $\sigma(\cdot)$ of all SDM parameters calculated with the explicit methods and the fitting one.

Results show that each method converges towards different SDM parameters solutions, especially for the dark saturation current I_0. This issue has been already discussed in [114], where it has been shown that very dissimilar sets of the SDM parameters lead to either identical or very close *I-V* characteristics. For this

Table 2.5. Mean value μ and standard deviation σ of the 5 SDM calculated by different methods

		Fitting	Phang	SPRatio	Toledo	LambertW
$\mu(I_{ph})$	[A]	2.677	2.659	2.655	2.658	2.655
$\sigma(I_{ph})$	[A]	0.006	0.006	0.006	0.007	0.006
$\mu(I_0)$	[μA]	0.52	1.8	25	3.0	0.0079
$\sigma(I_0)$	[μA]	0.11	0.7	13	1.0	0.0007
$\mu(n)$		1.282	1.39	1.69	1.44	1.004
$\sigma(n)$		0.010	0.03	0.07	0.03	0.002
$\mu(R_s)$	[Ω]	0.336	0.312	0.000	0.260	0.452
$\sigma(R_s)$	[Ω]	0.005	0.009	0.000	0.012	0.005
$\mu(R_{sh})$	[Ω]	105.8	182	206	182	86.3
$\sigma(R_{sh})$	[Ω]	2.1	13	10	13	1.3

reason, once the five parameters have been estimated for any experimental curve, the *MAPE* (Mean Absolute Percentage Error) of the main electrical parameters (I_{SC} , V_{OC}, P_{max}, I_{Pmax} and V_{Pmax}) is estimated by the following equation:

$$MAPE = \frac{100}{r} \cdot \sum_{i=1}^{r} \left| \frac{y_i - \tilde{y_i}}{y_i} \right| \tag{2.44}$$

where y_i is the value of I_{SC} , V_{OC}, P_{max}, I_{Pmax} or V_{Pmax} calculated directly from the experimental curve and $\tilde{y_i}$ is the same electrical parameter extracted by the *I–V* curve calculated with the single diode model by using the five parameters estimated by each explicit and fitting methods.

A Global Curve Error (*GCE*) based on the similarity between experimental and analytical *I-V* curves is also computed. The GCE takes into account the error in all the *current-voltage* pairs in the first quadrant of the *I-V* plane, it is calculated by considering the area enclosed between the two curves. The relative percentage curve error (*GCE [%]*) is obtained dividing the global error by the area below the experimental curve. As described in [115], this procedure is not depending on the distribution of the experimental points along the curve and the numerical result is more precise. The *MAPE* errors as well as the relative curve error for each method are shown in Table 2.6.

It is noticeable that all the explicit methods, except *LambertW*, have approximated the short-circuit current I_{SC} with much more accuracy than the fitting method.

Table 2.6. *MAPE* of electrical parameters and global curve error *(GCE)*

		LambertW	Phang	SPRatio	Toledo	Fitting
I_{SC}	[%]	0.5	0.0003	0.0015	0.00010	0.4
V_{OC}	[%]	0.4	0.13	0.11	0.11	0.14
P_{max}	[%]	0.10	0.15	0.08	0.11	0.08
I_{Pmax}	[%]	0.6	0.9	0.3	0.6	0.3
V_{Pmax}	[%]	0.7	0.7	0.3	0.5	0.21
GCE	[%]	1.4	0.3	0.9	0.3	0.3

This can be easily justified by the fact that the fitting method performs a global optimisation while explicit methods are working by using only notable points and slopes. For the open-circuit voltage all of them achieves similar results, being *LambertW* the less accurate. The case is the same when predicting the maximum power, but for this case, *Phang* method is slightly worse than the other ones. It is very interesting the behaviour of *SPRatio* to estimate the exact location of the MPP, because it not only achieves a very precise maximum power estimation, but also is almost as good as the fitting procedure for obtaining the pair (V_{Pmax},I_{Pmax}). When analysing the global curve error (similarity between curves), Fitting, Phang and Toledo get very good results.

2.5 Results with additional series resistance

Once the ability of the different methods to estimate the values of the parameters at nominal conditions has been tested, the next step is to study their behaviour when additional resistance is connected in series to the module terminals. Specifically, we want to compare the capacity of the different methods to detect correctly the emulated variation of the PV series resistance. In other words, when a series resistance of a nominal value ρ is added, a particular method m estimates a value of serial resistance equal to $R_s^{(m)}(\rho)$ that is expected to account the emulated variation. The objective would be to calculate how much greater is this value with respect to $R_s^{(m)}(0\ \Omega)$ that is the value without additional resistance, then $\Delta R_s^{(m)}(\rho) = R_s^{(m)}(\rho) - R_s^{(m)}(0\ \Omega)$ is the estimation of ρ provided by the method m.

In order to compare the R_s estimation belonging to different experiments ($\rho = 0\ \Omega$, $\rho = 0.3\ \Omega$, $\rho = 1\ \Omega$, $\rho = 1.5\ \Omega$), they should be referred to the same level of irradiance G_{I}. However, each experiment has been performed under outdoor conditions on different days, being the sequence of the values of incident irradiance G_{I} different from one experiment to other. Therefore, it is very difficult to find two estimations of R_s from different experiments but with the same irradiance.

This issue has been solved by using the regression lines of R_s estimated in the previous experiments (eq 2.43) without PV degradation. Indeed, for each method the corresponding regression line allows to estimate the value of R_s for a given irradiance G_I when $\rho = 0\ \Omega$. In this way, for each experimental *I-V* curve measured with an additional series resistance ρ and under an irradiance $G_\mathrm{I}[i]$, the $R_s^{(m)}(\rho)[i]$ is estimated directly with the method m whereas the value $R_s^{(m)}(0\,\Omega)[i]$ in $G_\mathrm{I}[i]$ is calculated by using the regression line.

The regression lines are then calculated for the points $\{G_\mathrm{I}[i], \Delta R_s^{(m)}(\rho)[i]\}$, to study if there is any correlation between the detected resistance variation $\Delta R_s^{(m)}$ and the incident irradiance G_I. The values $\Delta R_s^{(m)}(\rho)$ should be as close as possible to the added resistance ρ and independent on the irradiance (the regression line should be flat and R^2 very close to zero).

The results of these calculations for the different methods can be seen in Figure 2.14 and Figure 2.15. In every figure, six lines have been plotted but three of them are common: the regression lines of $\Delta R_s^{(F)}(0.3\ \Omega)$, $\Delta R_s^{(F)}(1.0\ \Omega)$ and $\Delta R_s^{(F)}(1.5\ \Omega)$ where $^{(F)}$ stands for the *Fitting method* that is still representing the reference. The other three lines of each figure correspond to $\Delta R_s^{(m)}(0.3\ \Omega)$, $\Delta R_s^{(m)}(1.0\,\Omega)$ and $\Delta R_s^{(m)}(1.5\,\Omega)$, being $m \in \{$*Phang*, *Toledo*, *LambertW*, *SPRatio*$\}$ in the different figures.

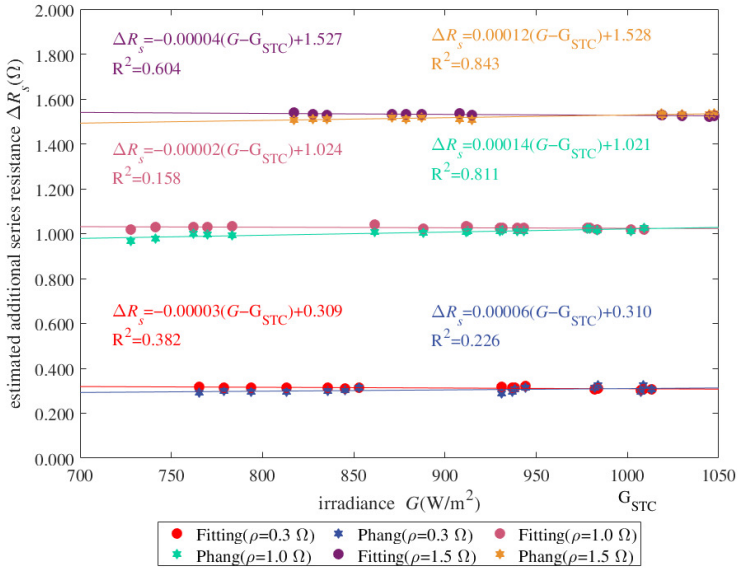

(a) Phang vs. Fitting

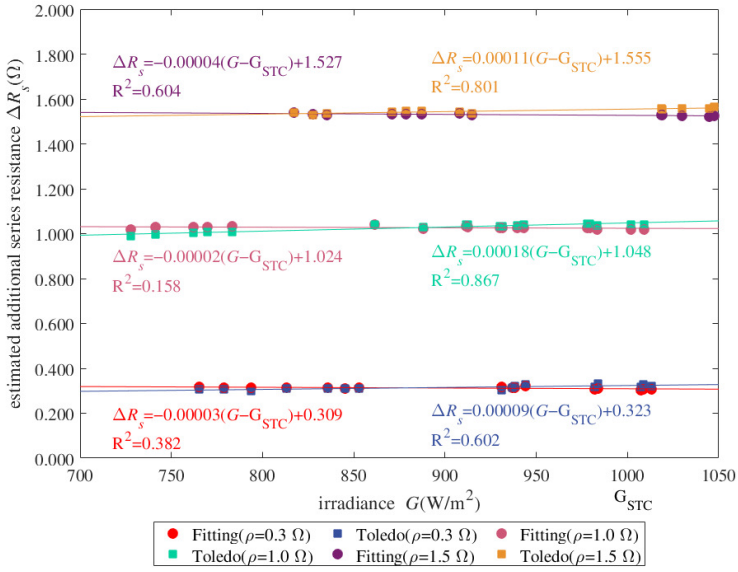

(b) Toledo vs. Fitting

Figure 2.14. Detection of additional series resistance ΔR_s for Phang and Toledo methods

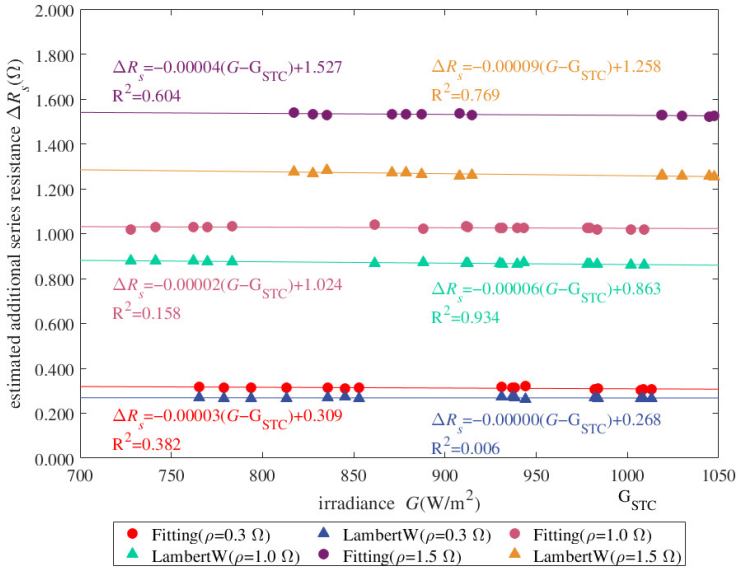

(a) LambertW vs. Fitting

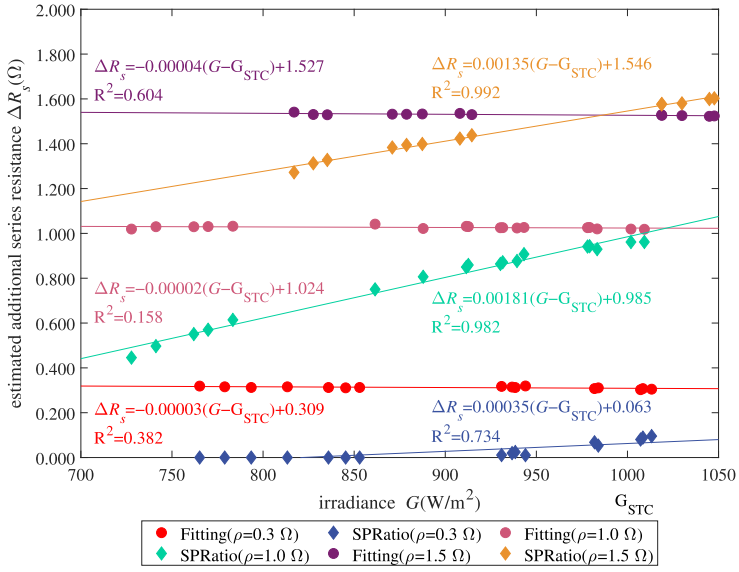

(b) SPRatio vs. Fitting

Figure 2.15. Detection of additional series resistance ΔR_s for LambertW and SPRatio methods

By comparing the four explicit methods with respect to the fitting results it is shown that *Phang* and *Toledo* methods are very effective in the identification of ΔR_s. *LambertW* method gives always an underestimation of ΔR_s. Moreover, the higher the added resistance the higher the error $\Delta R_s - \rho$, hence *LambertW* method is not suitable to identify the SDM parameters for a highly degraded PV panel. As concerns the *SPRatio*, the assumption that R_s is neglected when the coefficient $SPR < 1$ says that the method is not able to detect degradation when the PV series resistance is low. Nevertheless, *SPR* is itself a potential discrete indicator of degradation because when the series resistance increases the *SPR* indicators becomes higher than 1 indicating that the R_s cannot be neglected.

Table 2.7. Mean value μ and standard deviation σ of the parameters with additional $R_s = 1.5\ \Omega$

		Fitting	Phang	SPRatio	Toledo	LambertW
$\mu(I_{ph})$	[A]	2.688	2.659	2.624	2.659	2.624
$\sigma(I_{ph})$	[A]	0.004	0.004	0.003	0.004	0.003
$\mu(I_0)$	[μA]	0.34	0.92	57	1.2	0.0086
$\sigma(I_0)$	[μA]	0.03	0.07	5	0.1	0.0004
$\mu(n)$		1.240	1.323	1.829	1.347	1.0027
$\sigma(n)$		0.01	0.02	0.01	0.02	0.002
$\mu(R_s)$	[Ω]	1.858	1.831	1.532	1.809	1.722
$\sigma(R_s)$	[Ω]	0.003	0.003	0.004	0.003	0.002
$\mu(R_{sh})$	[Ω]	89.4	137	∞	135	58.4
$\sigma(R_{sh})$	[Ω]	1.2	4		4	0.4

Table 2.8. *MAPE* of electrical parameters and global curve error (*GCE*) with $\Delta R_s = 1.5\ \Omega$

		LambertW	Phang	SPRatio	Toledo	Fitting
I_{SC}	[%]	3	0.004	0.007	0.0014	0.3
V_{OC}	[%]	0.6	0.22	0.12	0.11	0.15
P_{max}	[%]	0.6	0.3	0.12	0.12	0.10
I_{Pmax}	[%]	3	0.6	0.015	0.4	0.11
V_{Pmax}	[%]	4	0.3	0.10	0.24	0.09
GCE	[%]	4	0.4	1.2	0.3	0.20

Table 2.7 shows the identified SDM parameters while Table 2.8 reports the *MAPE* of the main electrical parameters and global curve error for the experimental cases performed with the additional series resistance $\rho = 1.5\ \Omega$. Again *LambertW* does not give satisfying results in terms of global curve error. Focusing on the others explicit methods, is confirmed that although they do not provide a set of identified parameters close to the results obtained by the *Fitting Method*, they are able to

reproduce the I–V curves with a global curve error very small, providing a good similarity between experimental and analytical I–V curves. Indeed, the I–V curves shown in Figure 2.16 are almost overlapped with experimental results except for the *LambertW* method that provides an I-V plot slightly different. This happens in both normal and degraded conditions by confirming that such comparison is not enough to verify which methods are more effective to estimate correctly the R_s variation and, as a consequence, to detect the PV degradation properly.

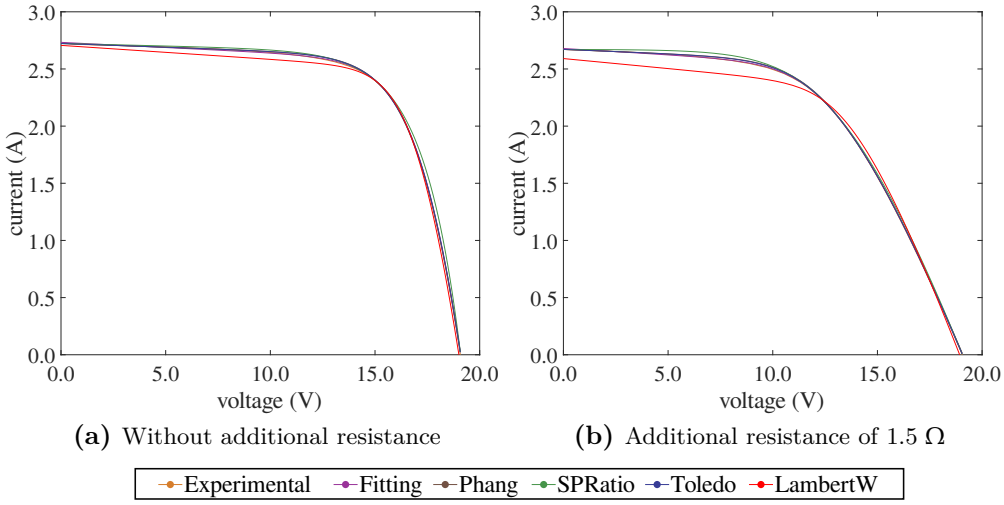

(a) Without additional resistance **(b)** Additional resistance of 1.5 Ω

Figure 2.16. Comparison between experimental and simulated curves for different experiments

2.6 Conclusions

An experimental validation of explicit methods used for the SDM parameter identification has been carried out in this chapter. The analysis has been focused on the series resistance identification in presence of degraded I-V curves. Among them *Phang* method exhibits good capability to estimate both the R_s resistance as well as the emulated additional series resistance ΔR_s.

Toledo method gives an underestimation in the R_s calculation but it is strongly accurate in ΔR_s estimation because the error of R_s calculated in nominal is almost totally compensated by the error of R_s calculated in degraded condition.

LambertW method is less accurate in R_s calculation and moreover the ΔR_s estimation worsens as the additional series resistance increases. This method seems more effective in the evaluation of R_{sh} parameter.

SPRatio method gives bad results in R_s and ΔR_s calculation, nevertheless the

SPR coefficient could be used as discrete indicator for degradation since it strongly depends on the R_s variation. *SPRatio* method gives also and almost exact location of the MPP point both in nominal and degraded conditions.

The analysis, although is not exhaustive, allows to assess that some set of explicit equations provide accurate evaluation of PV series resistance therefore suitable to be implemented on embedded systems for online parameters identification.

The main results of this chapter are published in J1 and B1 documents referenced in the list of publication.

Since the objective of this thesis is to investigate the effectiveness of different approaches to detect PV panel degradation, the study will continue in the next chapter where some approaches belonging to the optimisation methods are analysed.

Early Detection of Photovoltaic Panel Degradation through Artificial Neural Network

3.1 Introduction

Inside the category of *optimization approaches*, artificial neural networks have been proven to be an effective tool for SDM parameters identification. In [116] a multilayer perceptron (MLP) for identifying the I_{ph}, R_s, and I_{sat} parameters has been implemented. The method requires an input vector composed by $I_{sc}, V_{oc}, I_{mpp}, V_{mpp}$ and P_{mpp}. Since these values are provided by the PV panel datasheet, the effectiveness of this method is limited to healthy operating conditions. The study shown [117] instead is focused on identifying the most important points of the $I-V$ curve such as $V_{oc}, I_{sc}, P_{mpp}, V_{mpp}$, and I_{mpp} at the panel level. The method needs as inputs only the irradiance and temperature values and the proposed ANN is realised with a two-hidden layer MLP configuration. In [118], a recurrent neural network was implemented for predicting the output current of the cell by using temperature, irradiance, and voltage as inputs. In [119] the input vector is composed by a mix of environmental and electrical variables such as irradiance, temperature, $V_{oc}, I_{sc}, V_{mpp}, I_{mpp}$, and P_{mpp}. In this case, the parameters identified were R_s, R_{sh}, and η for an application at panel level. A comparison provided in this paper, shows that ANN outperforms ANFIS in estimating the required parameters. Finally, authors in [120] and [121] proposed configurations based on feed-forward neural networks for identifying the full-set of five parameters by means of a two-stage identification. Both works only use irradiance and temperature as inputs, but the work in [121] was focused on a single cell while the other [120] concentrated on an entire PV panel. From the literature analysis has been verified that ANN architectures are valid tool for SDM parameters estimation but, as for the explicit methods discussed in the previous chapter, very few information related to the SDM parameters estimation of PV panel in degraded conditions are available in the literature.

For this reason, in the following section a numerical method is presented that combines $I-V$ curve fitting process performed off-line with a simple ANN architecture operating on-line for estimating the variation of PV panels' SDM parameters when the PV panels are subject to degradation.

With respect to existing approaches, the technique introduced in this chapter has the advantage of providing in run-time the trend of PV degradation through the quantification of the SDM parameters variation with respect to the healthy conditions, thus suitable for predictive maintenance. Moreover, the proposed method uses only three points of the $I-V$ curve around the maximum power point, irradiance and panel temperature thus without using the whole $I-V$ curve that could not be always available during the normal operation of the PV system. Finally, due to the fast elaboration of the ANN results, it can be easily implemented on an embedded system for the online elaboration, once the training phase is performed off-line.

3.2 Description of the proposed approach

In section 1.3.2 the strictly correlation among PV panel degradation and SDM parameters variation have been put into evidence by analysing the $I-V$ curves. On the other hand, the parameters of the PV equivalent circuit change with respect to the irradiance and the temperature of the solar cells. The relationship between them is nonlinear and cannot be easily expressed by analytical equations and nonlinear regression methods can fails when any preliminary information about the input-output relationships are provided. Many papers tried to characterize such behavior. However, it is strongly dependent on the PV panel under test and no general rules can be applied. Some examples are reported in [122]; in [123] authors highlight that the fitting curve, that maps each SDM parameter as function of environmental condition, also varies along the seasons due to the influence of the variable weather and environmental conditions.

As a consequence, a reliable identification of PV degradation phenomena cannot be achieved if relationships among SDM parameters and the environmental condition are not properly accounted for.
The capability of the ANN to train non-linear and unknown relations among variables and to generalize these relationships when new input is provided to the ANN, will be exploited for solving this task. Since ANN does not required knowledge of internal system parameters, it implies reduced computational effort and represents a compact solution for multivariable problems. It is also a good candidate to be implemented on embedded system for online operation.

Figure 3.17 shows the flow chart of the procedure proposed in this chapter. In particular it describes the main steps for selecting the ANN input and target

datasets and performing the ANN training phases.
In stage 1, the ANN will predict the equivalent circuit parameters by only measuring the irradiance and temperature. Such parameters will be assumed as reference values for the healthy operating condition. Indeed for training this ANN, a proper number of healthy $I-V$ curves, acquired in different environmental conditions, has been selected and the corresponding SDM parameters are used as target dataset. As shown in [120], ANN can provide very good estimation of healthy SDM parameters for every environmental condition. This SDM parameters estimation will be used as baseline for detecting possible presence of degradation.

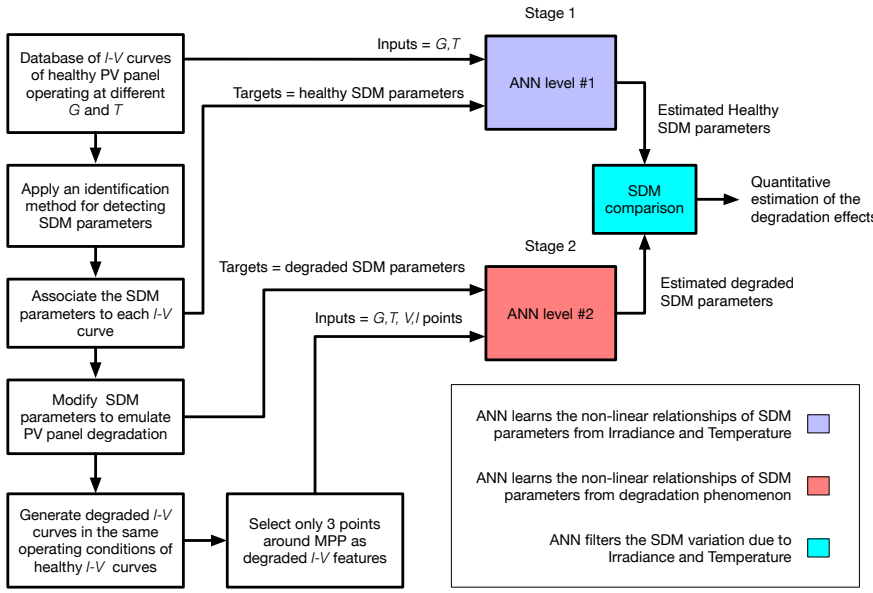

Figure 3.17. Flow chart for training the proposed ANN architecture

In stage 2, a more complex ANN architecture is trained to account for the different types of degradation. For achieving this task, a modified set of $I-V$ curves has been generated by using the single diode model with different sets of parameters that are associated to realistic degradation phenomena. In this stage the ANN receives as input not only the irradiance and cell temperature but also some points of the $I-V$ curve, which are necessary to take into account the modification of the $I-V$ curve shape due to the degradation.

It is worth to note that in this paper only three points around the maximum power point will be used. This allow to monitor the PV source's state of health during normal operation, without the need of a complete scan of the $I-V$ curve: measurement of voltage and current around the MPP will suffice for the detection of degradation. More details on the generation of degraded dataset are given in

section 3.3.2.

The two training phases are completely independent, having in common only part of the input data (G and T) and providing two sets of SDM parameters. The output of stage 1 represents the vector of estimated SDM parameters under the hypothesis that the PV panel is not degraded, thus in healthy condition. The output of stage 2 is the vector of estimated SDM parameters associated with real operating condition, thus representing the real status of health. The difference between the two estimations will give a measure of which parameter is changing and consequently which type of degradation is occurring inside the PV panel. Details on how to configure the ANN architectures are reported in section 3.4.

It is worth to note that the ANN stages are representing the regression models used to estimate the value of a dependent variable (SDM parameters) based on its relationship to one or more independent (predictor) variables (e.g environmental and electrical values associated to a specific operating condition). As discussed in the last part of this chapter the reliability of the estimated results is depending not only on the ANN performances but also on the quality of fitting procedure employed to generate the input-output examples used to train the ANNs.

3.3 Description of Experimental $I - V$ curves Database

For covering as much as possible the different outdoor operating conditions of a real PV arrays, a large database of experimental data has been selected. The $I - V$ curve dataset provided by the National Renewable Energy Laboratory (NREL) is used at beginning to develop the proposed method. NREL has a public database with data measured for flat-plate photovoltaic (PV) modules installed in three different cities in the USA (Cocoa-Florida, Eugene-Oregon, and Golden-Colorado). The experimental process collected PV module current-voltages curves and meteorological data samples from 2010 until 2014 [124]. The work employed different PV technologies such as Single-crystalline silicon (c-Si), Multi-crystalline silicon (m-Si), Cadmium telluride (CdTe), Copper indium gallium selenide (CIGS), Amorphous silicon (a-Si) tandem and triple junction, Amorphous silicon/crystalline silicon or heterojunction with intrinsic thin layer (HIT), and Amorphous silicon/microcrystalline silicon. The database does not report specific commercial or manufacturer information for avoiding any legal conflict. To describe the procedure proposed in this manuscript, without losing of generality, the Multi-crystalline silicon PV module information will be used.

The variables extracted and used for the procedure were the plane-of-array

irradiance (W/m^2), the PV module back surface temperature (°C), and the corresponding current-voltage curve represented with a numbers of points ranging from 180 to 190 samples, depending on the voltage resolution settled on the tracer device.

Table 3.9 shows the features and ranges of measurements of the panel chosen for performing the current analysis.

Table 3.9. Characteristics of the PV panel under study and ranges of the data measured.

Parameter	Value
Technology	Multi-crystalline silicon
Number of cells	36
Module Area	0.647 [m^2]
STC Parameters	
I_{sc}	4.937 [A]
V_{oc}	21.357 [V]
I_{mp}	4.533 [A]
V_{mp}	17.072 [V]
Plane of Array irradiance	(200 - 1300) [W/m^2]
Range of Temperature	(20 - 65) [° C]
Number of points for each $I-V$ curve	[180 - 190]

The irradiance and temperature ranges also have a high impact over the performance of the PV model. From the literature is well known that the single diode model is not suitable for characterizing the PV devices at low irradiance values [125]. For this reason, in this work will refer to irradiance values in the range from medium to high irradiance and only $I-V$ curves acquired with irradiance level above 200 [W/m^2] will be used.

When it comes to the temperature, the single-diode model has not particular restrictions about the ranges. Therefore, there is not any restriction about the ranges of temperature. This work took $I-V$ curves acquired in a wide temperature range of [20-65]°C degrees.

High quality datasets is a key factor for training efficiently the ANN. To achieve this, the data must first be collected and cleaned to remove errors (bad data), outliers, and samples with excessive noise. If these practices are skipped or poorly executed, it will be difficult for the ANN to detect the true underlying models.

In certain cases, partial shading or measurement issues in the tracer device provided $I-V$ curves shapes that generate wrong SDM parameters. For this reason the $I-V$ curves in the NREL database have been preliminary analysed and the ones having abnormal profile have been discarded. At the end more than 20,000 $I-V$ curves are available in the filtered database.

It is worth to note that only a part of the available NREL database is necessary for

the ANN training phases, thus the proposed approach can be applied in practical applications where enough $I-V$ curves are available for different irradiance and temperature conditions. More details on the used $I-V$ curve are given in sections discussing the simulation and experimental cases.

During the normal operation only few values of voltage and current (V_{pv}, I_{pv}) around the MPP, irradiance (G), and PV panel temperature (T) measurements are used as the inputs to the neural network. They have been chosen since they are already measured on photovoltaic installations. Therefore, it is possible to take advantage of such information for online monitoring of the PV source's state of health by means of the proposed ANN architecture.

3.3.1 Generation of training set and validation set for a healthy PV panel

The reference values of the SDM parameters, representing for the ANNs the target values, must be calculated for each experimental $I-V$ curve that will be used during the ANN training and validation processes. Since the ANN training phase is performed offline, the target dataset can be generated by using the nonlinear least-square solver of Matlab to assure an high-quality fitting among the experimental $I-V$ curves and the ones generated by the single diode model. Details on the fitting procedure are reported in section 2.2.5.

For every selected experimental $I-V$ curve, thus for known (G,T), the fitting procedure calculates the set of five parameters $\mathbf{p} = [I_{ph}, I_{sat}, \eta, R_s, R_{sh}]$ that minimize the mean square error between the experimental data and the $I-V$ curve generated by using the single-diode model. In this way, the $\mathbf{p}$ vector associated to the healthy $I-V$ curve will be the target used to train the neural network.

It is worth to highlight that, while the single diode model allows to describe the electrical constraint between $I-V$ measurements (V_{pv}, I_{pv}) and SDM parameters in the form:

$$f(V_{pv}, I_{pv}, \mathbf{p}) = 0 \tag{3.45}$$

the ANN allows to detect the unknown relations:

$$\mathbf{p_H}(G,T) = [I_{ph}, I_{sat}, \eta, R_s, R_{sh}]_H = \mathbf{F_H}(G,T) \tag{3.46}$$

or

$$\mathbf{p}^{deg}(G,T,\mathbf{V},\mathbf{I}) = [I_{ph}, I_{sat}, \eta, R_s, R_{sh}]^{deg} = \mathbf{F^{deg}}(G,T,\mathbf{V},\mathbf{I}) \tag{3.47}$$

where the vector $\mathbf{p_H}(G,T)$ is the estimation of the healthy SDM parameters for the environmental conditions G,T. The vector $\mathbf{p}^{deg}(G,T,\mathbf{V},\mathbf{I})$ is the estimation

of the SDM parameters for the same environmental condition but also accounting PV degradation through the voltage and current values $(\mathbf{V}, \mathbf{I})$ measured around MPP.

3.3.2 Generation of training set and validation set for a degraded PV panel

Although the NREL database collects $I-V$ curves of PV panels operating in outdoor conditions, there are no information if some of them can be classified as degraded $I-V$ curves. For this reason each available $I-V$ curve has been analysed in terms of $I-V$ curve shape, slopes and operation conditions in order to take from the NREL database only healthy $I-V$ curves. Experimental degraded $I-V$ curves are not easily detectable because of the difficulty of reproducing the large variety of degraded conditions and the long time the measurement process will take for registering these kinds of phenomena. For these reasons, in the development of the proposed approach the $I-V$ degraded curves are reproduced artificially by still using the single diode model where variations on the SDM parameters are fixed and know a priory. In this way it will be easy to generate enough $I-V$ curves useful for the ANN training process. This is a similar approach already adopted for emulating PV faults and mismatched operating conditions in others fault identification methods [56, 58, 126].
The degraded $I-V$ curves database have in common with the healthy $I-V$ curves database the same environmental conditions. The new database is generated by applying the pseudo code shown in table 3.10. $N_{healthy}$ is the number of experimental $I-V$ curve taken from the healthy database.

```
for n = 1 : N_healthy
        load irradiance and temperature G, T
        load I − V curve as vectors V_pv, I_pv
        load the vector p of healthy SDM parameters
                for k = 1 : 5
                        assign a random variation (α_k ∈ [α_k,min, α_k,max]) to
                                the k-th parameter:  p(k)^deg = α_k · p(k)
                        calculate the I − V degraded curve by using equation (??)
                                I_pv^deg = f(V_pv, p^deg)
                        save G, T, I_pv^deg, V_pv and p^deg in the degraded database
                end
end
```

Table 3.10. Pseudo code for generating degraded $I-V$ curves

It is worth to note that a degradation effect is applied separately to each parameter, thus the database containing the degraded $I-V$ curves is five times larger than the healthy database. Moreover, to introduce different levels of $I-V$ curve deformation, the parameters degradation effect is randomly chosen according to the boundaries shown in table 3.11. Such boundaries have been

chosen by taking into account that the sensitivity of the $I-V$ curve with respect to each SDM parameter is strongly different, as highlighted in section 1.3.2.
An example of degraded $I-V$ curve obtained artificially by starting from a healthy experimental $I-V$ curve is reported in Figure 3.18. The figure also shows the only three points that will be used by the ANN to estimate the SDM parameters.

degradation factor	$\alpha_{k,min}$	$\alpha_{k,max}$
$I_{ph}^{deg} = \alpha_1 I_{ph}$	0.95	0.9
$I_{sat}^{deg} = \alpha_2 I_{sat}$	2	10
$\eta^{deg} = \alpha_3 \eta$	0.98	0.9
$R_s^{deg} = \alpha_4 R_s$	2	6
$R_{sh}^{deg} = \alpha_5 R_{sh}$	1/3	1/20

Table 3.11. SDM parameters variation for generating degraded $I-V$ curves

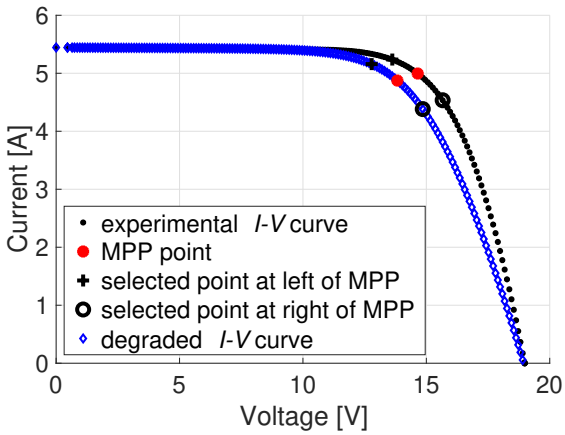

Figure 3.18. Healthy and degraded $I-V$ curves with the selected points passed to the ANN

3.4 Configuration of the proposed double level ANN architecture

This work uses a multi-layer feed-forward neural network. It is conformed by one input layer, one hidden layer, and one output layer. The number of neurons in the input layer is equal to the number of parameters that compound the input vector. The number of neurons in the output layer is fixed by the number of parameters

to identify, in this case, five neurons (equal to the set of five parameters). The number of neurons in the hidden layer depends on the complexity of the problem, a rule of thumb is to choose the smallest configuration that reaches the performance and accuracy wished [120].

The developed ANN is shown in figure 3.19, it is composed of two levels trained independently. The first level is devoted to estimate the parameters of the single diode model by using as input only the irradiance and the PV panel temperature. It is trained by using as target values the SDM parameters extracted with the MATLAB fitting procedure associated to the healthy $I-V$ curve. A number of $N_{trial} = 5000$ experimental curves are selected randomly from the NREL database in order to cover the different environmental conditions. The selected dataset is distributed as 70% for training set, 15% for validation set and 15% for testing set. An inner layer with 20 neurons is used.

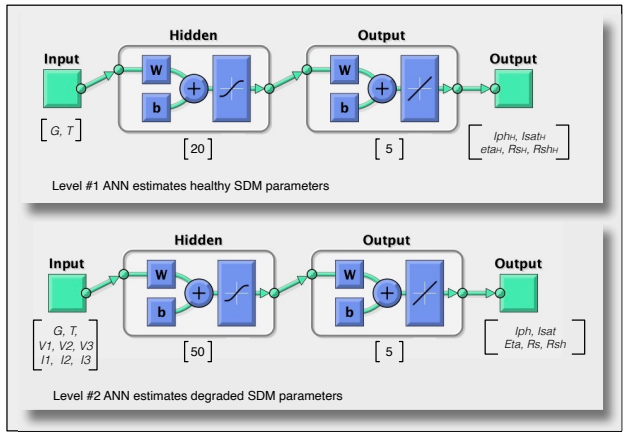

Figure 3.19. Proposed ANN architecture

The second level of the ANN architecture is trained by using as target values the SDM parameters associated to the degraded $I-V$ curves. In this case, the input is a vector of eight elements including the irradiance, temperature, and voltages and currents of the three points around MPP. They are equally spaced of 1 Volt with respect to the MPP, as shown in figure 3.18.
A number of $5 \cdot N_{trial}$ curves are selected randomly from the degraded database in order to cover the different environmental conditions and different kind of parameter degradation. Also in this case, the selected dataset is distributed as 70% for training set, 15% for validation set and 15% for testing set. An inner layer with 50 neurons is used.

The MATLAB Neural Network Toolbox® is employed for configuring, training and testing the proposed architecture.

It is worth to note that, although in this manuscript all the elaborations have been performed on a PC, the trained ANNs can be exported in the Open Neural Network Exchange files [127] and executed by the most common open-source platforms (eg. TensorFlow®) thus for running on embedded systems.
Alternatively, the MATLAB Compiler SDK® [128] could be used for compiling the MATLAB® functions into a shared library for C/C++, .NET, Java, or Python projects and executed on the most common development boards, eg. Raspberry®, BeagleBone® or DSP/FPGA-based architectures.
Moreover, microcontroller manufactures allow to train ANNs and develop optimized codes directly by using their programming tools, thus to optimize performance and reduce development costs [129].

3.4.1 Dataset Normalization

Before passing the inputs and targets to the neural network architecture, it is necessary to preprocess the dataset values for improving the performance of the training process. The normalization process is important for neural network training because it adjusts the different inputs and outputs ranges to a normalized range before applying them to the neural network. In MATLAB the normalization process is set by default and adjust the values to fall in a range between [-1,1]. But in this case, it was found a small bug associated with the default normalization process. It was found that the default normalization process has problems with inputs or targets too small producing errors in the training process. For instance, the common range for the saturation current I_{sat} is in the order of micro and nano amperes. These ranges of values do not allow that the training process found a suitable fit for the targets.

For solving this issue, the normalization process was implemented manually and the inputs and targets will be adjusted in this way:

$$input = \left[\frac{G}{G_{max}}, \frac{T}{T_{max}}\right] \qquad \text{for ANN level \#1}$$

$$input = \left[\frac{G}{G_{max}}, \frac{T}{T_{max}}, \frac{V_i}{V_{max}}, \frac{I_i}{I_{max}}\right] \quad i \in [1,2,3] \qquad \text{for ANN level \#2}$$

$$target = \left[\frac{I_{ph}}{I_{ph,max}}, \frac{log_{10}(I_{sat})}{log_{10}(I_{sat,max})}, \frac{\eta}{\eta_{max}}, \frac{R_s}{R_{s,max}}, \frac{R_{sh}}{R_{sh,max}}\right]$$

for the saturation current the normalization is given on a logarithmic scale for better representing the large range of variation of this parameter.

Since the neural network will approximate its outputs inside the same range, it is also necessary to convert the ANN results back into the same range than the originals inputs and targets.

3.4.2 Overfitting and Generalization

Another common problem of the neural network training process is overfitting. This concept is associated with the way the neural network learns the process and adjust a model for representing it. In a training process with overfitting, the neural network finds a model that fits the set of data. Although the error in this process could be set very small, the neural network builds a too complex model that is unable to identify the right outputs for new data presented to the input. Therefore, the neural network has memorized the behavior of the training data instead of building a model that generalizes the outputs for testing or validation data.

A regularization method consists of modifying the performance function. In this case, the default performance function used by the toolbox of Matlab is the mean square error (MSE) defined as in (3.48). This performance function can be tuned for focusing on generalization by using the weights and bias of the neural network. Here, it is necessary to add the mean values of the sum of weights (MSW) of the neural network to the performance function. Equation 3.50 expresses the way for tuning this configuration. The parameter γ (performance ratio) allows the user to define the level of impact of the regularization. This parameter must be defined in a range between [0-1]. In this case, the user must use his expertise to find a trade-off between generalization and performance [130],[131].

$$\text{MSE} = \frac{1}{N}\sum_{i=1}^{N} e_i^2 = \frac{1}{N}\sum_{i=1}^{N}(t_i - a_i)^2 \tag{3.48}$$

$$\text{MSW} = \frac{1}{n}\sum_{j=1}^{n} w_j^2 \tag{3.49}$$

$$\tilde{E} = \gamma * \text{MSW} + (1-\gamma) * \text{MSE} \tag{3.50}$$

Where N is the number of trials, n is the total number of weights w_i for all the ANN nodes.

Here, the challenge is to choose the correct value for the performance ratio parameter (γ). If the user uses a parameter too large has the risk of overfitting. On the contrary, if the performance ratio parameter is too small, the neural network will not fit the training data adequately.

Bayesian regularization is a neural network training algorithm that updates the weights and bias values. The main characteristic of this algorithm is that it automatically determines the optimal regularization parameters and the correct combination for making up neural networks that generalize well. In the toolbox of Matlab, this function uses Jacobian for calculation, then, the performance must

be mean or sum of square errors. As a consequence, the training process must be assessed by MSE or by the sum square error (SSE) performance functions [116, 131].

The Bayesian regularization method does not need to configure a performance ratio parameter. On the contrary, it automatically calculates the best parameters focusing on generalization.

In the following the results concerning the ANN trained with Bayesian regularization is proposed, they exhibit a good identification of SDM parameters both in healthy and degraded conditions.

3.5 ANN identification results for healthy conditions

The continuous lines in the figures 3.20-3.24 are the estimated SDM parameters provided by ANN, they refer to the healthy conditions and put into evidence the intrinsic relationships among SDM parameters with the environmental conditions for the PV panel under test. It is worth to note that, apart from I_{ph} that is almost linear with G and practically insensitive with respect to the temperature, the behaviour of remaining parameters is completely different from the cases analysed in [120] and [123]. This result is not so much surprising, given that the relationships among parameters and the environmental conditions change significantly from panel to panel.

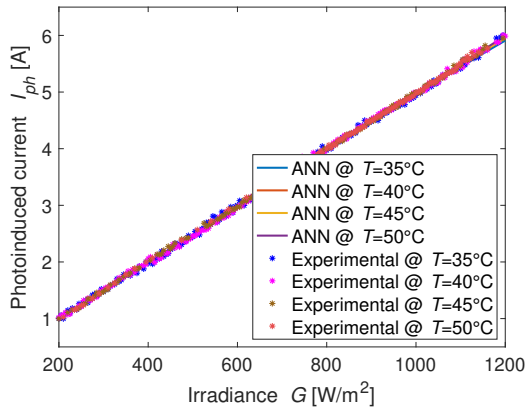

Figure 3.20. ANN identification of the photoinduced current in healthy condition.

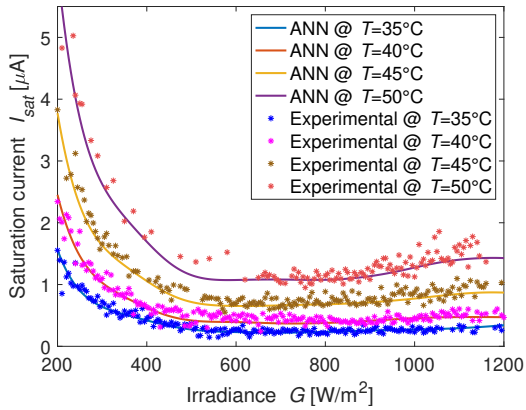

Figure 3.21. ANN identification of the saturation current in healthy condition.

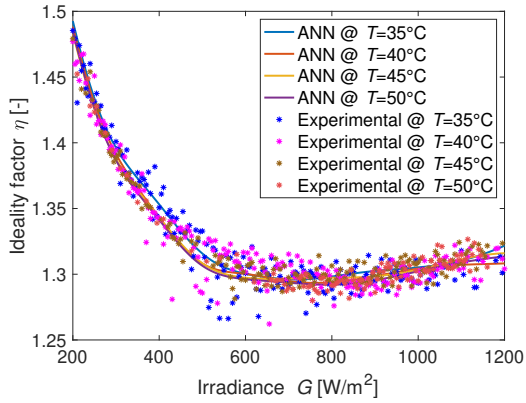

Figure 3.22. ANN identification of the ideality factor in healthy condition.

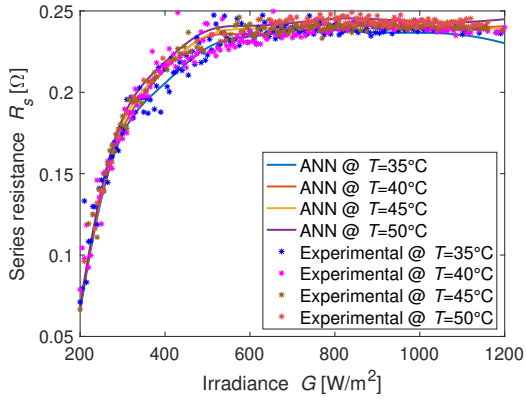

Figure 3.23. ANN identification of the series resistance in healthy condition.

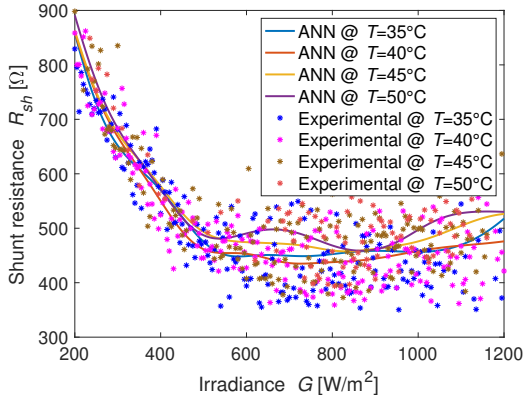

Figure 3.24. ANN identification of the shunt resistance in healthy condition.

To demonstrate the goodness of the ANN parameters estimation, in figures 3.25-3.26 the plots of experimental data, selected randomly from the NREL database, in comparison with the reconstructed $I-V$ curves obtained with the estimated parameters at low and high irradiance conditions are shown.

The Error Area, defined as the difference among the area below the reconstructed $I-V$ curves and the area below the corresponding experimental $I-V$ curve, has been calculated for the tested cases and only for few cases, referring to the low irradiance conditions, a 5% of maximum error has been found. In figure 3.25 the corresponding I-V plots is shown. Nevertheless, this error can be considered acceptable since, as already remarked in [125], the single-diode model is less precise for low irradiance conditions.

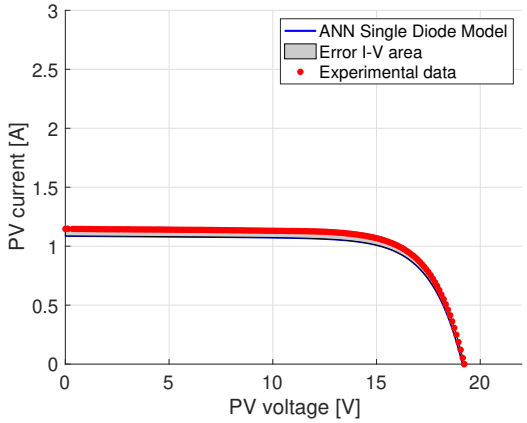

Figure 3.25. Comparison of experimental data and reconstructed single-diode $I-V$ curve with estimated ANN parameters in healthy condition. In this case the error area is 5%

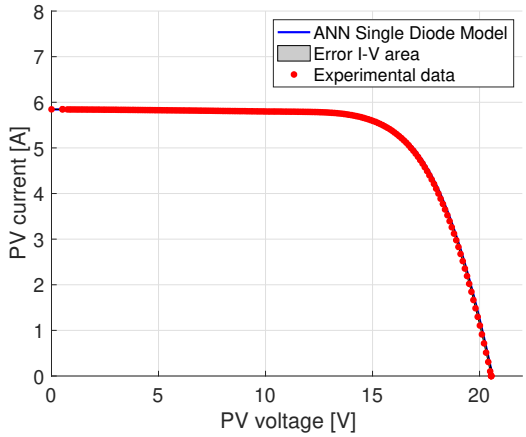

Figure 3.26. Comparison of experimental data and reconstructed single-diode $I-V$ curve with estimated ANN parameters in healthy condition. In this case the error area is 0.5%

3.6 ANN results with simulated degradation on $I-V$ curves

The capability of ANN to detect the degraded SDM parameters is tested in this section by still using emulated degraded curves. Even if this is a limitation with respect to using real degraded curves it allows to corroborate the methods with a well controlled degradation effect introduced artificially. For each k parameter ($k \in [1, .., 5]$), the analysis is carried out by using the following procedure:

- Select randomly N_{test} experimental healthy $I-V$ curves from the NREL database (not used during the ANN training phases) and save the related SDM parameters as the vector $\mathbf{p}$ and environmental conditions (G, T).
- For each selected case
  1. Apply a fixed degradation factor α_k to the k-th parameter of $\mathbf{p}$.
  2. Generate the degraded $I-V$ curve by using equation (**??**)
  3. From the degraded $I-V$ curve select the voltage and current of 3 points equally spaced around MPP and ordered in the vector $[V_1, V_2, V_3, I_1, I_2, I_3]$.
  4. ANN(level #1) estimates the healthy SDM parameters $\mathbf{p_H}$ with $[G, T]$ as input vector.
  5. ANN(level #2) estimates the degraded SDM parameters $\mathbf{p_{deg}}$ with $[G, T, V_1, V_2, V_3, I_1, I_2, I_3]$ as input vector.
  6. Calculate the percentage of parameters variation as follows:

$$\mathbf{\Delta p}_{\%} = \frac{\mathbf{p_{deg}} - \mathbf{p_H}}{\mathbf{p_H}} \cdot 100 \tag{3.51}$$

Figures 3.27-3.30 show some comparison between the degraded $I-V$ curves (blue lines) and the reconstructed $I-V$ curves (light blue lines) obtained by using the $\mathbf{p_{deg}}$ parameters estimated by means of ANN. In each figure the healthy $I-V$ curves (red lines) used to generate the degraded curves and the 3 points passed to the ANN for estimating the SDM degraded parameters are also reported. Of course, in on board operation only steps **3-4-5-6** of the previous procedure are necessary since all ANN input are provided by the real-time measurements.

As mentioned in section 1.3.2, the sensitivity of $I-V$ curve with respect to each SDM parameter, especially close to the maximum power point, is strongly different. In particular variation of few percents on I_{ph} and η produce a significant modification of the $I-V$ curves, while the effect of I_{sat}, R_s and R_{sh} is visible on the $I-V$ curve only for larger percentage variations. For this reason, different percentages of degradation have been considered in the examples shown in figures 3.27-3.30. In Tables 3.12-3.16 the corresponding ANN identification results are reported. The vector ($\mathbf{p_{deg}}$) of degraded SDM parameters estimation is compared with the healthy SDM parameters estimation vector ($\mathbf{p_H}$) to calculate ($\mathbf{\Delta p}_{\%}$) and

find out which parameter has the most significant percentage variation.

It is worth to note that, in order to establish which kind of degradation is most relevant the vector of maximum power variations $\mathbf{\Delta P_{mpp,\%}}$, due to each parameter variation, has been also shown in the tables. It has been estimated numerically as follows:

- Calculate the maximum power in healthy condition P^H_{mpp} by using the single diode model and healthy parameters ($\mathbf{p_H}$).

- For $k \in [1, 5]$

  - replace the parameter $\mathbf{p_H}(k)$ with the corresponding degraded values $\mathbf{p_{deg}}(k)$

  - estimates the maximum power P^k_{mpp} by still using the SDM.

  - calculate the $\Delta P(k)_{mpp,\%} = \frac{P^k_{mpp} - P^H_{mpp}}{P^H_{mpp}} \cdot 100$

The percentage error evaluation allows to appreciate rapidly the ANN capability to detect the degradation on each SDM parameter and the related impact on the P_{mpp}.

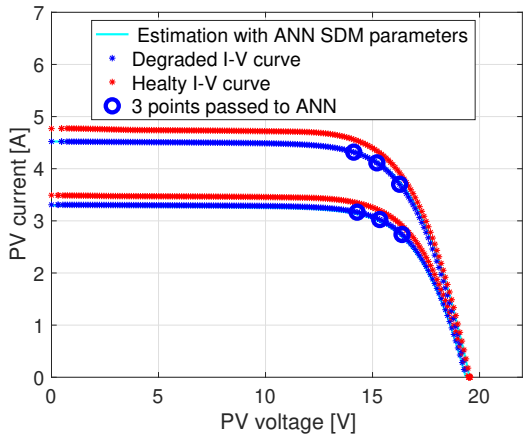

Figure 3.27. ANN identification of degraded curve with -5% of variation on I_{ph} for two different irradiance and temperature conditions.

Table 3.12. SDM parameters estimated with ANN for $I-V$ curves of figure 3.27

applied degradation: $I_{ph}^{deg} = 0.95 I_{ph}$ (-5%)							
G [$\frac{W}{m^2}$]	T [°C]		I_{ph}[A]	I_{sat} [μA]	η [-]	R_s [Ω]	R_{sh} [Ω]
695	49	$\mathbf{p_H}$	3.476	0.996	1.296	0.242	490
		$\mathbf{p_{deg}}$	3.297	0.900	1.284	0.255	277
		$\mathbf{\Delta p_{\%}}$	**-5.13**	-9.6	-0.92	5.4	-43.5
		$\mathbf{\Delta P_{mpp,\%}}$ 0.9	**-5.37**	0.85	-0.96	-0.26	-0.77
955	53	$\mathbf{p_H}$	4.782	0.1562	1.296	0.247	466
		$\mathbf{p_{deg}}$	4.526	0.1480	1.295	0.238	356
		$\mathbf{\Delta p_{\%}}$	**-5.36**	-5.3	-0.04	-3.8	-23.6
		$\mathbf{\Delta P_{mpp,\%}}$ 0.9	**-5.47**	0.39	-0.08	0.22	-0.27

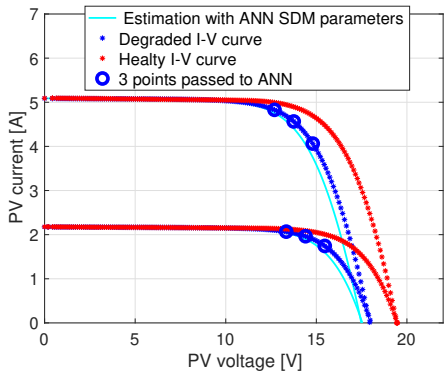

Figure 3.28. ANN identification of degraded curve with 200% of variation on I_{sat} for two different irradiance and temperature conditions.

Table 3.13. SDM parameters estimated with ANN for $I-V$ curves of figure 3.28

applied degradation: $I_{sat}^{deg} = 3 I_{sat}$ (200%)							
G [$\frac{W}{m^2}$]	T [°C]		I_{ph}[A]	I_{sat} [μA]	η [-]	R_s [Ω]	R_{sh} [Ω]
1020	55	$\mathbf{p_H}$	5.083	2.001	1.300	0.248	491
		$\mathbf{p_{deg}}$	5.090	5.730	1.256	0.254	511
		$\mathbf{\Delta p_{\%}}$	0.13	**186**	-3.39	2.4	4.0
		$\mathbf{\Delta P_{mpp,\%}}$ 0.9	0.14	**-9.13**	-3.62	-0.19	0.03
435	42	$\mathbf{p_H}$	2.150	0.645	1.328	0.224	520
		$\mathbf{p_{deg}}$	2.175	1.882	1.288	0.229	559
		$\mathbf{\Delta p_{\%}}$	1.16	**192**	-3.02	2.1	7.4
		$\mathbf{\Delta P_{mpp,\%}}$ 0.9	1.25	**-8.68**	-3.05	-0.07	0.11

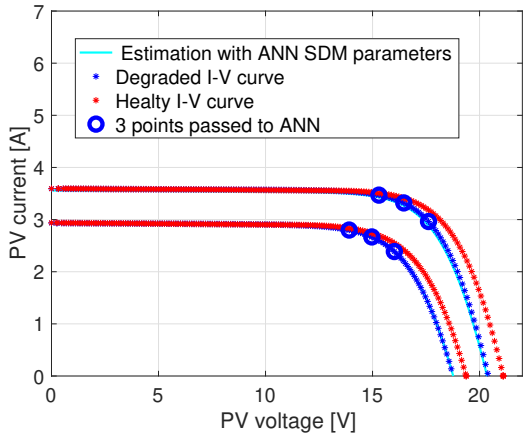

Figure 3.29. ANN identification of degraded curve with -3% of variation on η for two different irradiance and temperature conditions.

Table 3.14. SDM parameters estimated with ANN for $I-V$ curves of figure 3.29

applied degradation: $\eta^{deg} = 0.96\eta$ (-4%)							
G [$\frac{W}{m^2}$]	T [°C]		I_{ph}[A]	I_{sat} [μA]	η [-]	R_s [Ω]	R_{sh} [Ω]
445	31	$\mathbf{p_H}$	2.194	0.204	1.331	0.219	496
		$\mathbf{p_{deg}}$	2.192	0.222	1.290	0.252	538
		$\mathbf{\Delta p}_{\%}$	-0.07	8.8	**-3.06**	15.0	8.4
		$\mathbf{\Delta P_{mpp,\%}}$ 0.9	-0.1	-0.63	**-3.1**	-0.37	0.14
865	41	$\mathbf{p_H}$	4.311	0.445	1.296	0.240	449
		$\mathbf{p_{deg}}$	4.283	0.432	1.239	0.243	446
		$\mathbf{\Delta p}_{\%}$	-0.67	-2.8	**-4.41**	0.85	-0.6
		$\mathbf{\Delta P_{mpp,\%}}$ 0.9	-0.67,	0.23,	**-4.61**	-0.07	-0.01

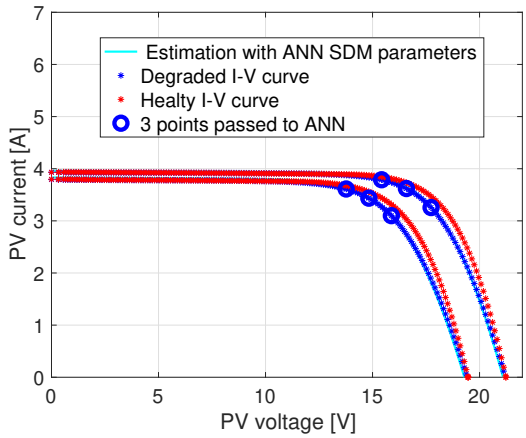

Figure 3.30. ANN identification of degraded curve with 70% of variation on R_s for two different irradiance and temperature conditions.

Table 3.15. SDM parameters estimated with ANN for $I-V$ curves of figure 3.30

applied degradation: $R_s^{deg} = 1.7R_s$ (+70%)							
G [$\frac{W}{m^2}$]	T [°C]		I_{ph}[A]	I_{sat} [μA]	η [-]	R_s [Ω]	R_{sh} [Ω]
755	51	$\mathbf{p_H}$	3.791	1.195	1.293	0.244	490
		$\mathbf{p_{deg}}$	3.834	1.377	1.295	0.390	446
		$\mathbf{\Delta p_{\%}}$	1.16	15.2	0.175	**59.6**	-8.9
		$\mathbf{\Delta P_{mpp,\%}}$ 0.9	1.18	-1.19	0.16	**-3.24**	-0.09
795	26	$\mathbf{p_H}$	3.907	0.094	1.305	0.232	511
		$\mathbf{p_{deg}}$	3.963	0.090	1.294	0.367	449
		$\mathbf{\Delta p_{\%}}$	1.44	-4.0	-0.84	**58.6**	-12.2
		$\mathbf{\Delta P_{mpp,\%}}$ 0.9	1.48	0.31	-0.87	**-2.58**	-0.14

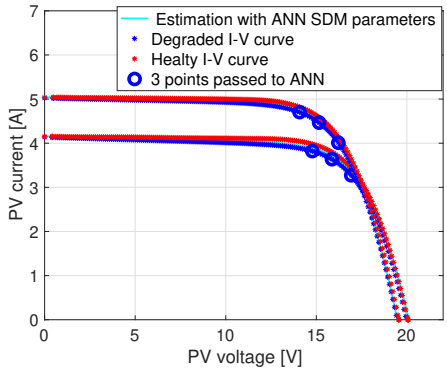

Figure 3.31. ANN identification of degraded curve with -80% of variation on R_{sh} for two different irradiance and temperature conditions.

By analysing the results shown in Tables 3.12-3.16, in particular $\mathbf{\Delta p_{\%}}$, it is evident that the ANN allows to associate, with a good approximation, the degradation effect introduced on the $I-V$ curve to the corresponding SDM parameter. Nevertheless, in some cases, the results of ANN parameters identification are not completely satisfactory. For instance, in the first example of Table 3.12, the ANN estimates a -43.5% reduction of R_{sh} reduction that does not correspond to a real degradation of such parameter. The wrong estimation of R_{sh}, that may occur also for the other SDM parameters, is due to the intrinsic nature of the ANN to provide generalized results when the input data change. Moreover since the $I-V$ curve sensitivity with respect to some parameters is very low, errors on the estimation of these parameters are more likely and more frequent. The results can be improved if the proposed procedure is repeated and the parameters degradation is detected by considering their average values. Some examples are reported in the following section.

Table 3.16. SDM parameters estimated with ANN for $I-V$ curves of figure 3.31

applied degradation: $R_{sh}^{deg} = 0.2R_{sh}$ (-80%)							
G [$\frac{W}{m^2}$]	T [°C]		I_{ph}[A]	I_{sat} [μA]	η [-]	R_s [Ω]	R_{sh} [Ω]
835	44	$\mathbf{p_H}$	4.165	0.615	1.297	0.240	454
		$\mathbf{p_{deg}}$	4.170	0.614	1.304	0.247	107
		$\mathbf{\Delta p}_{\%}$	0.12	-0.1	0.55	2.7	**-76.4**
		$\mathbf{\Delta P_{mpp,\%}}$ 0.9	0.12	0.013	0.57	-0.16	**-3.04**
1000	53	$\mathbf{p_H}$	5.023	1.670	1.301	0.246	493
		$\mathbf{p_{deg}}$	5.051	1.791	1.298	0.243	191
		$\mathbf{\Delta p}_{\%}$	0.56	7.3	-0.18	-1.1	**-61.2**
		$\mathbf{\Delta P_{mpp,\%}}$ 0.9	0.57	-0.6	-0.24	0.09	**-1.06**

3.6.1 Improving the ANN results with repeated tests

By assuming that a degradation phenomenon is occurring permanently, the ANN parameters identification method can be executed frequently (e.g. more than one time per day) without affecting the normal operation of the PV system and the $\mathbf{\Delta p}_{\%}$ can be estimated for all cases. Since the effective degradation of the PV panel is not related to the changes in the environmental conditions, the average values of $\mathbf{\Delta p}_{\%}$ is considered for all tests collected in a short period (e.g one day). Table 3.17 shows the average percentage variation of the SDM parameters estimated with the ANN when the process described in the previous section is repeated for a number of trials $N_{test} = 100$ selected randomly among different environmental conditions. Each row in the table is referring to the parameters variation reported in the first column. For example for the first row, a -4% of induced degradation on I_{ph} is estimated in average with -3.73%.

It worth to note that some residual cross-coupled variations appears in the estimation of the other parameters. Nevertheless if we take into account the different sensitivity of $I-V$ curve with respect to each parameter, these crossed variations can be acceptable. Indeed by considering the sensitivity values reported in (1.4) and by referring to the first row of Table 3.17, the -3.73% reduction in I_{ph} is reflected in a reduction of 3.76% in the delivered power, while a -22.3% of variation in R_{sh} corresponds to 0.69% power reduction.

Another small anomaly is in the second row where the identification of the variation of the saturation current is not detected accurately (+103 %) with respect to an induced degradation of +150% on I_{sat}. In this case part of the induced degradation on I_{sat} is translated in a variation of η. This can be easily justified by the fact that variations on I_{sat} and on η parameters produce the same deformation on the $I-V$ curve (see S2 and S3 effects in figure 1.4), thus for the ANN is more difficult to detect the origin of degradation when they produce similar deformation on the $I-V$ curve.

Table 3.17. Average of SDM parameters variation (in %) estimated with ANN

degradation factor	**estimated param. variation**				
	$\Delta I_{ph,\%}$	$\Delta I_{sat,\%}$	$\Delta\eta\%$	$\Delta R_{s,\%}$	$\Delta R_{sh,\%}$
$I_{ph}^{deg} = 0.96 I_{ph}$ (-4%)	**-3.73** (1.52)	-0.9 (8.8)	0.09 (0.68)	10.5 (13.7)	-22.3 (20.4)
$I_{sat}^{deg} = 2.5 I_{sat}$ (+150%)	0.57 (1.39)	**103.0** (25.2)	-2.96 (0.63)	14.0 (16.0)	0.7 (3.8)
$\eta^{deg} = 0.97\eta$ (-3%)	-0.29 (1.74)	2.8 (8.0)	**-3.30** (0.77)	4.8 (10.6)	0.1 (5.3)
$R_s^{deg} = 1.7 R_s$ (+70%)	0.64 (1.18)	10.1 (8.3)	-0.12 (0.58)	**61.1** (13.3)	-3.0 (7.4)
$R_{sh}^{deg} = 0.2 R_{sh}$(-80%)	0.06 (0.85)	5.9 (8.0)	0.30 (0.54)	10.4 (15.7)	**-64.9** (13.7)
without deg.	-0.87 (1.62)	-3.3 (6.2)	-0.76 (0.44)	-2.2 (15.4)	2.3 (11.1)

(*) in the brackets the standard deviation of the SDM parameter percentage variation

Finally, the last row indicates the average errors on the estimated SDM parameters when no degradation has been applied. Here is evident that in presence of healthy curves the estimation of the SDM parameters variation tends to small values confirming that no degradation is occurring.

3.6.2 Comparison with other ANN solutions

In table 3.18 the main characteristics of the proposed ANN architecture is compared with other ANN solutions proposed in the last years and briefly commented in the introduction. The table includes only the methods suitable for *on-line* diagnosis and faults detection of PV sources.

The comparison is done in terms of *ANN architecture*, *Inputs* required during on-line operation, *Data for the training phase* - usually performed in off-line mode, *PV granularity*, which means the level of applicability of the method (panel-, string- or array-level). The different types of *Detected faults* and the level of *Complexity*, that could have a significant impact on the embedded system implementation, have been also included in the comparison.
It is worth to note that the solution described in [59] uses two independent ANNs, thus similar to the approach developed in this manuscript, but the ANNs architecture and the type of detected faults are completely different. The other methods are mainly devoted to string or array diagnosis, thus not suitable for detecting degradation in a single PV panel.

The comparison also put into evidence that the selection of the appropriate method will strongly depend on the size of the PV source and on what type of faults must be detected.

Table 3.18. ANN techniques for PV diagnosis and faults identification

Ref.	ANN structure	Inputs	Data for the training phase	PV granularity	Detected faults	Complexity
[55]	MLP-ANN or RBF-ANN	V_{mpp}, I_{mpp}, V_{oc}	simulated $I-V$ curves in faulty conditions	PV string	shadow, cell in open circuit, shunted bypass diode, short circuit	Medium
[56]	KELM + SLFN	V_{mpp}, I_{mpp}, V_{oc}, I_{sc}, η,R_s	experimental and simulated $I-V$ curves in healthy and faulty operation	PV string, PV array	partial shading, string degradation, short circuit, open circuit	High
[57]	RBF-ANN	PV power, irradiance	long-term measure of PV production, irradiance	PV array	PV panel disconnection, partial shading	Low
[126]	Deep Learnig ANN	down sampled $I-V$ curves, G, T	simulated or experimental $I-V$ curves	PV array	R_s degradation, partial shading, short circuit, open circuit	High
[58]	PNN	per unit values of V_{mpp}, I_{mpp} V_{oc}, I_{sc}	simulated and experimental $I-V$ curves	PV array	R_s degradation, partial shading, short circuit, open circuit	High
[59]	2 PNN	irradiance, array's temperature V_{mpp},I_{mpp}	experimental healthy $I-V$ curves, simulated $I-V$ curves in faulty conditions	large PV array	number of short-circuited panels	Medium
Proposed method	2 MLP-ANN	3 points around MPP, irradiance panel temperature	Datasheet curves or healthy $I-V$ curves, simulated $I-V$ curves in degraded conditions	PV panel	panel degradation, partial shading, hot spots, by-pass diode failure	Low

3.7 ANN results with experimental degraded $I-V$ curves

The developed method has been also tested with experimental $I-V$ curves where the series resistance degradation is applied by connecting in series to the PV module a small resistance of value (ΔR_s). The experimental data refer to a *Isofotón I-53* PV module installed on the roof of the *Department of Applied Physic II* at the University of Málaga. The measurement setup is discussed in section 2.3.1 and the main data of PV panel are summarised in Table 2.4. The measurement equipment acquires simultaneously the $I-V$ curves, the in-plane irradiance (G) and the PV module temperature (T).

Figure 3.32 shows the effect of the induced R_s degradation on the $I-V$ curves at the same environmental conditions. We assume that the acquired $I-V$ curves with $\Delta R_s = 0$ correspond to the healthy conditions. The red points on the curves are the only values passed to the ANN together with G and T for estimating the degraded SDM parameters.

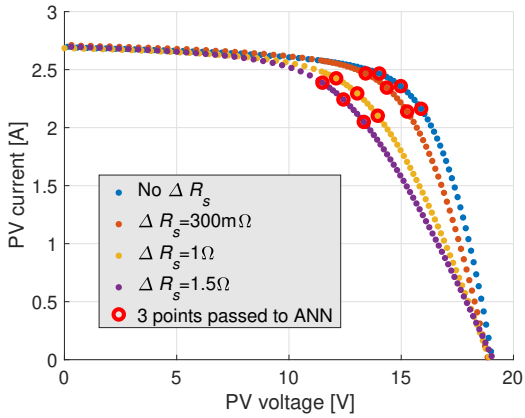

Figure 3.32. Experimental $I-V$ curves with added series resistance for the same environmental conditions

The ANN is trained only by using the healthy $I-V$ curves in combination with the single diode model for emulating the degraded curves, as described in the flowchart of figure 3.17.

The experimental degraded curves are obtained with $\Delta R_s = 300m\Omega$, $\Delta R_s = 1\Omega$ and $\Delta R_s = 1.5\Omega$. For the healthy conditions $R_s = 364m\Omega$ thus the induced degradation is 82%, 274%, 412% respectively. The SDM parameters variation estimated with the proposed ANN architecture are reported in figure 3.33 for different irradiance conditions. In that figure, the R_s parameter shows a trend that is in agreement with the expected values. The saturation current is a little

bit changing only at high irradiance, thus cannot be associated to a permanent degradation effect, while the other parameters do not exhibit a significant variation with respect to the values estimated in healthy conditions.

It is worth to note that the variation of I_{sat} for high irradiance values, that is not associated to a real degradation effect, could be due to a limited dataset used to train the ANN. Indeed, only 75 healthy experimental $I-V$ curves are available for this experimental example and they are not enough to cover all the operating conditions. An exhaustive experimental campaign should be executed that could lead to further improvement of the performance of the proposed method. Nevertheless also for this reduced dataset the proposed approach is able to isolate the main degradation effects by using the SDM parameters estimation as indicators of possible faults that could happen in the PV modules.

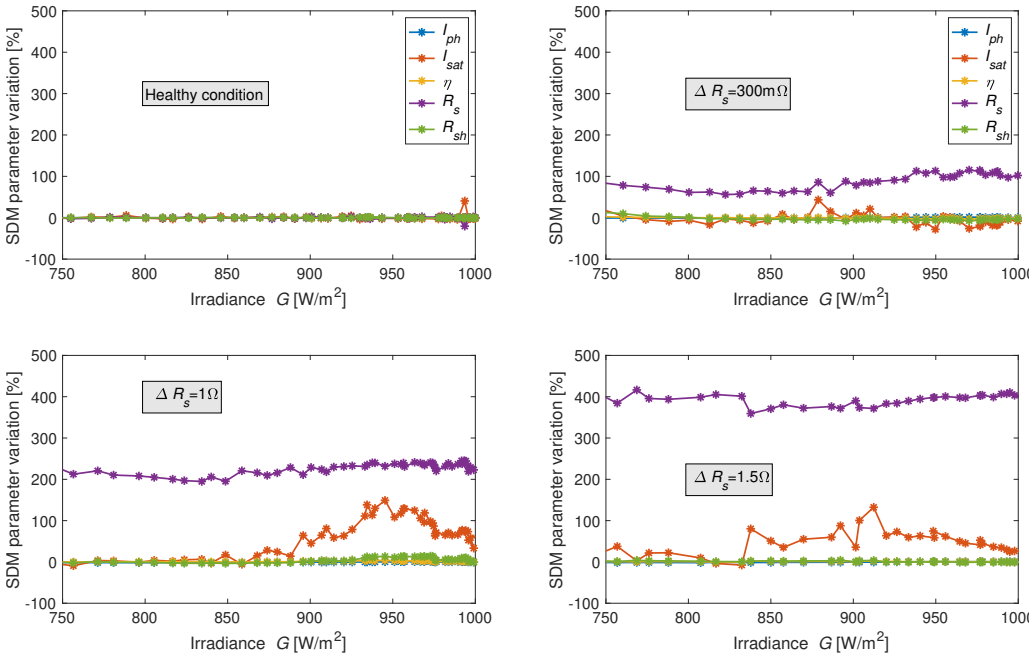

Figure 3.33. ANN identification of series resistance for different induced degradation effect and for different environmental conditions

3.8 Extending the methodology to other PV panels and technologies

The ANN architecture proposed in section 3.3 uses the data targets that are generated with a fitting procedure for obtaining the set of five parameters representing every I-V curve. Therefore this procedure impacts positively or

negatively the performance of the neural network. Since the set of five parameters identified in section 3.5 presented a variation particularly concentrated from low up to medium irradiance level, this section seeks to analyze this behavior for improving the quality of the target values generated as reference for the ANN.

Figure 3.34 shows the trends for the set of five parameters in a temperature range of [35-36] °C. Here, it is visible a pronounced non-linear behavior in four parameters (I_{sat}, η, R_s, and R_{sh}), especially at low irradiance (from 200 to 500 $[W/m^2]$). Additionally, it associates the percentage confidence interval error for every parameter. The I_{sat} and the R_{sh} parameters show high error in the whole irradiance range, while the R_s error is notable at low irradiance. I_{ph} and η illustrate high reliability based on their low errors along the whole irradiance range. Table 3.19 presents the minimum and maximum values of the percentage CI error for every parameter. Here it is evident the high variations previously associated to I_{sat}, R_s, and R_{sh}.

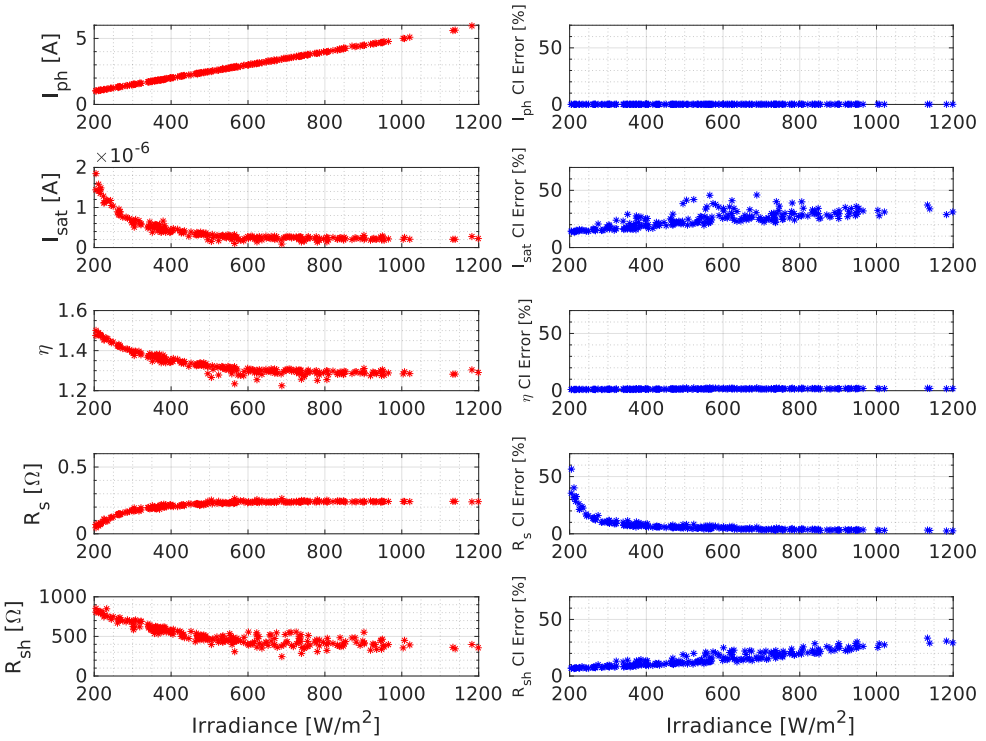

Figure 3.34. Trend of the set of five parameters and their percentage confidence interval error for a temperature range of [35-36] °C

Figure 3.34 demonstrates the high complexity of identifying the set of five parameters since they present a combination of non-linear behaviours. However, it also remarks the relevance in the reliability of the targets since they are the

Table 3.19. CI error ranges for the set of parameters (Fig.3.34)

	CI Error range [%]		
Parameter	**min**	**max**	**mean**
I_{ph}	0.06	0.17	0.09
I_{sat}	**13.64**	**45.93**	**24.53**
η	1.00	2.65	1.52
R_s	2.48	**56.52**	7.33
R_{sh}	6.61	**33.49**	15.21

samples from which the system will learn. Thus, some refinements are proposed for enhancing the quality of the targets and, as a consequence, the accuracy of the solution.

Since the database has data under outdoor conditions, it is possible to guess that some outliers could be present in the available data. A deep analysis of the samples has shown that some valid and stable I-V curves with same G and T have a considerable difference in the expected current value. This issue could be a result of dust or shadowing effect affecting the normal operation of the PV panel, thus, an additional condition can be applied for filtering the input data. In this way, the neural network will take clean information avoiding noisy data that will not contribute in the learning process. The database provides the measured values of I_{sc} of every I-V curve, moreover, the value of I_{sc} at standard test conditions (STC). Therefore, assuming that $I_{ph} \approxeq I_{sc}$, the expected current could be approximated by using equation 3.52 given specific G and T values [41].

$$I_{ph\_expected} = \left(\frac{G}{G_{STC}}\right) * [I_{ph,STC} + \alpha_i(T - T_{STC})] \tag{3.52}$$

Thus, the value of the $I_{ph\_expected}$ can be compared against the I_{sc} value measured for every I-V curve in the database. A range of 5% of the $I_{ph\_expected}$ is configured for filtering the I-V curves that fulfil the condition 3.53:

$$0.975 * I_{ph\_expected} < I_{sc} < 1.025 * I_{ph\_expected} \tag{3.53}$$

An additional improvement has been investigated regarding the cost function of the problem. In the current implementation, the MSE was used as the cost function to minimize searching for the solutions to the parameter identification using an iterative solution as the fitting approach. An additional revision has shown that in [132], [133],[134], and [44] the authors used the root mean square error (RMSE) as the cost function with good results on the parameter estimation using iterative and optimization approaches.Therefore, the cost function was updated to use the RMSE (Eq 3.54) for performing the fitting approach.

$$RMSE = \sqrt{\frac{\sum_{i=1}^{N}(I_{i,experimental} - I_{i,estimated})^2}{N}} \tag{3.54}$$

Figure 3.35 illustrates the trends obtained for the set of five parameters using the RMSE as the cost function and the additional filter implemented by means of equations 3.52 and 3.53. The assessment was implemented using the same conditions (G and T ranges) applied in Figure 3.34. Here, it is worth noting that the new set of parameters has more stable values, especially in the I_{sat} and η parameters. The strong non–linear effect in the irradiance level of 200 to 500 $[W/m^2]$ has been smoothed in all parameters. In the same line, the percentage CI error has also been reduced. Figure 3.35 depicts a more reliable CI error for the I_{sat} and the R_s.

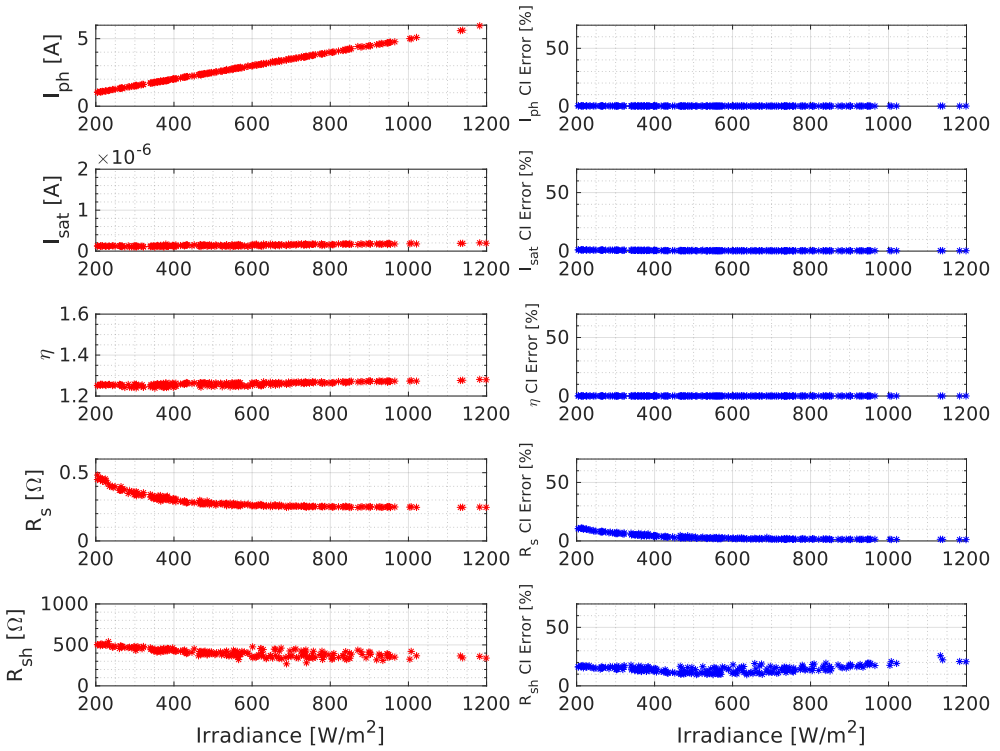

Figure 3.35. Percentage confidence Interval error for every parameter in a temperature range of [35-36] °C

Although the R_{sh} parameter continues to have a considerable non-linearity, this condition is in agreement with the results obtained in [135] where the approximation of this parameter shows high variability from low to high irradiance levels. Thus, it is considered an acceptable representation for the parameter

Table 3.20. CI error ranges for the set of parameters (Fig.3.35) calculated with the RMSE cost function

	CI Error range [%]		
Parameter	**min**	**max**	**mean**
I_{ph}	0.08	0.28	0.14
I_{sat}	0.25	**1.16**	**0.48**
η	0.02	**0.10**	**0.04**
R_s	1.06	**10.91**	**3.54**
R_{sh}	9.52	25.77	14.36

despite the visible non-linear trend. In fact, it remarks again on the non-linearity behavior of the PV panels through their characteristic parameters. Table 3.20 confirms a notorious reduction in the CI error for the I_{sat}, η, and R_s parameters. It validates the good reliability of the new set of parameters for describing the behaviour of the PV panel under study by using the RMSE cost function.

The methodology previously presented for the experimental campaign in section 3.3 focused on data from a particular PV panel. To assess the robustness of the proposed solution, especially the improved steps applied in the current section, the analysis could be extended to other PV panels with the same or different technology. Thus, the methodology is assessed with two additional PV panels presented in Table 3.21. PV panel B has the same type of technology as the PV panel studied in section 3.3 with the half area, while PV panel C differentiates in the kind of technology (Single-crystalline).

Table 3.21. Characteristics of the PV panel under study and ranges of the data measured.

Parameter	**PV panel B**	**PV panel C**
Technology	Multi-crystalline silicon	**Single-crystalline silicon**
Number of cells	36	36
Module Area	**0.342** [m^2]	0.647 [m^2]
STC Parameters		
I_{sc}	2.666 [A]	4.983 [A]
V_{oc}	22.040 [V]	21.946 [V]
I_{mp}	2.455 [A]	4.487 [A]
V_{mp}	18.064 [V]	17.39 [V]
Plane of Array irradiance	(200 - 1300) [W/m^2]	
Range of Temperature	(20 - 65) [° C]	
Number of points for each $I-V$ curve	[180 - 190]	

Figures 3.36 and 3.37 show that the data filtered and modeled with the RMSE cost function have smooth trends in almost the whole set of parameters. Tables 3.22 and 3.23 confirm the reliability of the parameters in terms of the low percentage CI

error for every parameter. In general, I_{ph}, I_{sat}, and η present a short percentage CI error. The R_s and the R_{sh} depict clear non-linear trends with a low CI error, which means good reliability on the value given to the parameter.

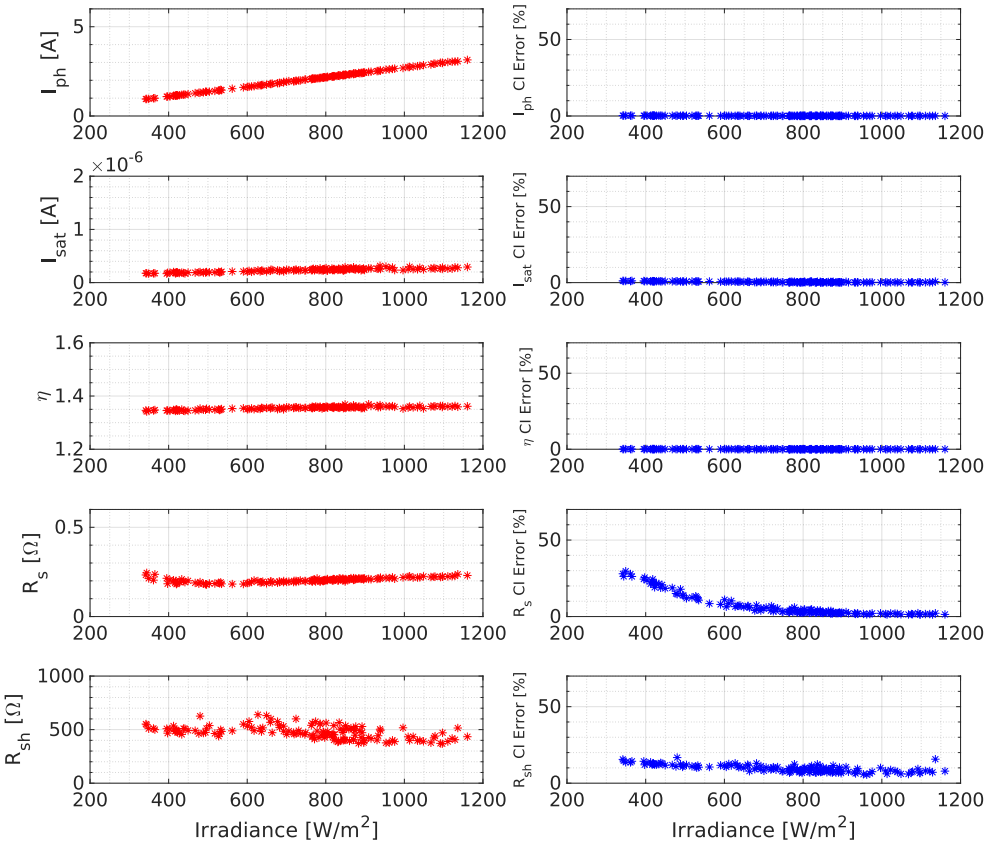

Figure 3.36. Percentage confidence Interval error for the set of five parameters of PV panel B in a temperature range of [35-36] °C

Table 3.22. CI error ranges for the set of parameters (Fig.3.36) calculated for the PV panel B

	CI Error range [%]		
Parameter	**min**	**max**	**mean**
I_{ph}	0.05	0.27	0.11
I_{sat}	0.14	1.16	0.46
η	0.01	0.10	0.04
R_s	1.22	29.66	7.04
R_{sh}	5.57	16.73	9.66

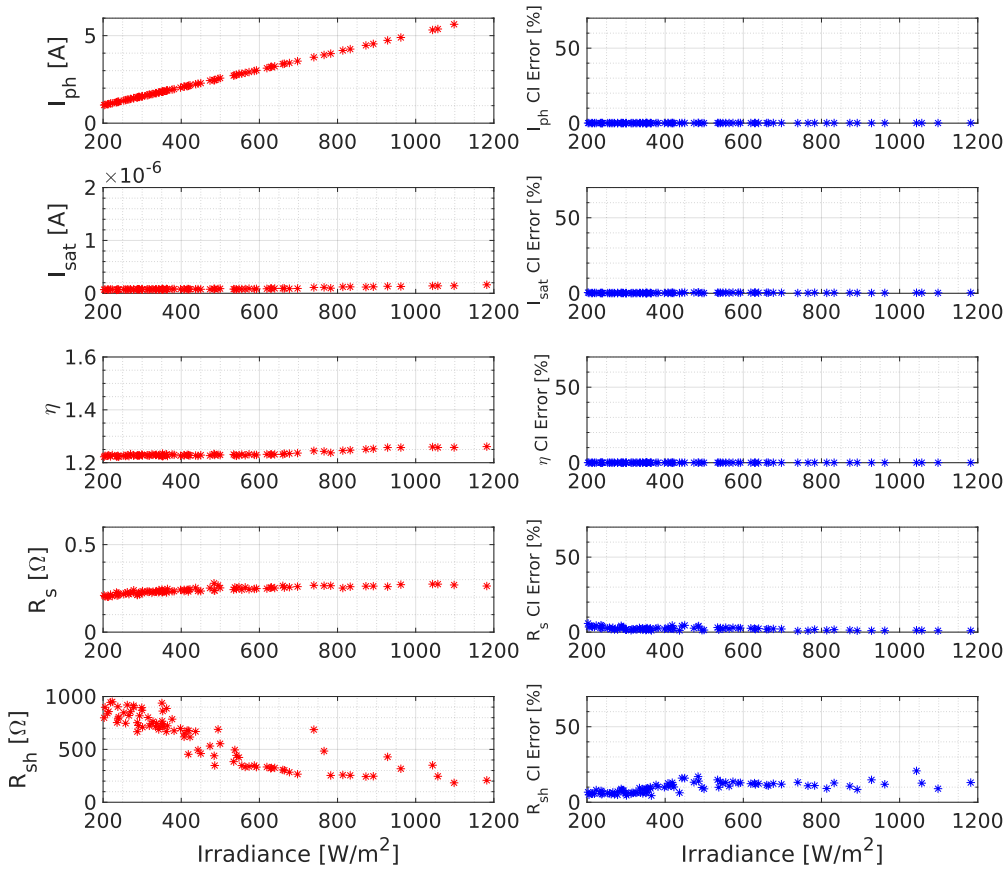

Figure 3.37. Percentage confidence Interval error for the set of five parameters of PV panel C in a temperature range of [37-38] °C

Table 3.23. CI error ranges for the set of parameters (Fig.3.37) calculated for the PV panel C

	CI Error range [%]		
Parameter	**min**	**max**	**mean**
I_{ph}	0.03	0.16	0.08
I_{sat}	0.08	0.57	0.26
η	0.01	0.05	0.02
R_s	0.79	5.80	2.38
R_{sh}	4.37	20.78	9.55

The current improvement shows a better way of getting the targets representing every I-V curve analyzed. It has the possibility of extending to other types of PV panels preserving a good representation of the SDM as targets of the system. It will enhance the ANN performance due to the high reliability of the parameters and the reduced non–linearities, especially in some of them, for being used as

targets for the learning process. In general, the improvement in the way of representing the problem leads to make easier the use even of other types of regressors for representing the problem.

3.8.1 Performance analysis of ANN used as regression model

The general schema (Figure 3.17) proposed for getting the estimation of the parameters in two stages used neural networks as regressors and obtained good performances. However, each stage could use a different technique for obtaining the corresponding representation. The Regression Learner tool of Matlab gives the possibility of having a fast assessment of the performance of multiple common machine learning techniques for having a preliminary view of the performance of the regression implemented for each technique. This tool helped to analyze other alternatives. Figures 3.38 and 3.39 show the performance of different machine learning techniques for estimating the series resistance R_s parameter for stage 2 of flowchart 3.17, it means, data in degraded conditions. This data has been chosen because is more challenging in terms of complexity.

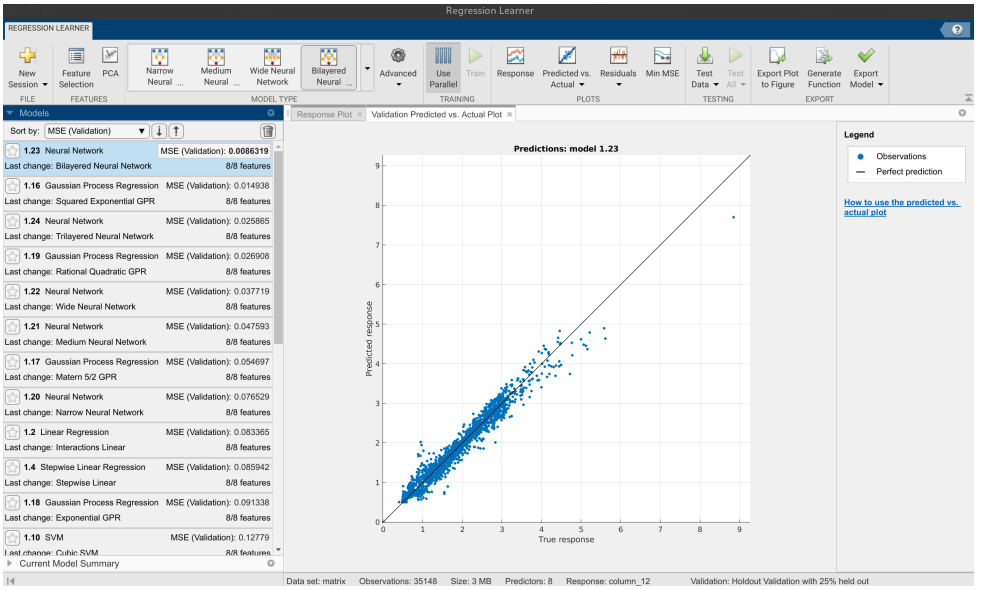

Figure 3.38. Performance of different machine learning techniques for characterizing the degradation effect on the set of five parameters: *Stage 2* of the figure 3.17

The list is ordered by the smaller MSE values. Figure 3.38 shows a situation where the application assesses multiple regressors with a basic configuration. A particular architecture of ANN reached the best performance in terms of MSE. But, it is clear that the different methodologies require optimizing their

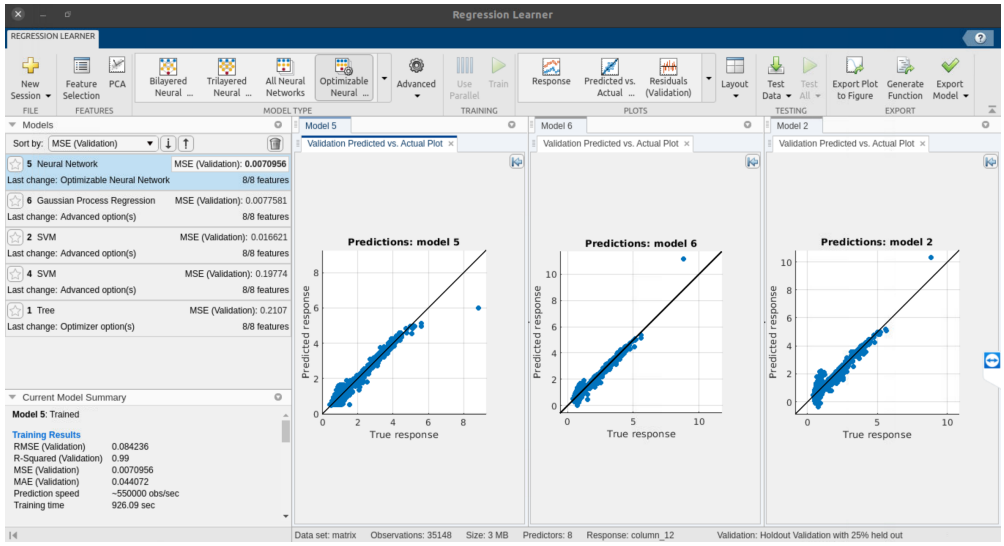

Figure 3.39. Performance of different machine learning techniques with a optimized procedure for detecting the degradation effect on the set of five parameters: *Stage 2* of the figure 3.17

internal hyperparameters for obtaining better outcomes. Figure 3.39 shows the assessment of different regressors in a training phase where the software optimizes automatically the hyperparameters of each method by using bayesian optimization. Again, the neural networks show good performance at the same level that other methods.

Table 3.24. Summary of the main characteristics of the regressors assessed

Method	**General Configuration**	**Validation stage**			
		RMSE	**R-Squared**	**MSE**	**Training Time [s]**
Neural Network	Three layers: [266 6 3]	0.0842	0.99	0.00709	**926.09**
Gaussian Process Regression (GPR)	Kernel function: Isotropic Rational Quadratic Kernel scale: Automatic	0.088	0.98	0.00775	4610.9
Suport Vector Machine (SVM)	Kernel function: Gaussian Kernel scale: Automatic	0.1289	0.97	0.0825	12037

Table 3.24 reports the general outcomes of the three best performances obtained by the software. Here, it is worth noting that neural networks obtained similar performance to the second-best regressor, but, with a notable difference in the training time, which means less complexity with high performance. It demonstrates again the applicability of neural networks in systems with medium-low computational resources.

3.9 Conclusions

In this chapter, the MLP artificial neural network is used for isolating faults and degradation phenomena affecting photovoltaic panels. The parameters of the single diode model have been used as indicators of the main degradation phenomena. The SDM parameters are strongly different from panel to panel and depend on environmental conditions, PV technology and manufacturing process. To identify the PV degradation through the SDM parameters, the proposed method exploits two independent MLP-ANN architectures. The first one is trained to estimate the SDM parameters of the healthy PV panel for the measured environmental conditions. Since only G and T are the inputs for this MLP-ANN, it is able to reproduce the non-linear relations existing among the SDM parameters of the healthy PV panel and the environmental conditions. The second MLP is trained to estimate the SDM parameters of the PV panel in presence of degradation phenomena affecting the $I-V$ curve for the measured environmental conditions. This second MLP-ANN requires as inputs G,T and 3 points of the $I-V$ curve measured close to the MPP, thus it estimates the SDM parameters including environmental and degradation effects. To isolate the degradation effect the difference among the two MLP-ANNs is used.

The main benefits of the proposed solution are:

- simple ANN architectures that allows an easy implementation on embedded system
- the ANN training process requires only experimental healthy $I-V$ curves
- does not require the complete $I-V$ scan during the online operation since the ANN accept as input only 3 experimental points measured around the MPP.
- The methodology exploits the reliability of the SDM for generating data able to emulate reliable degraded conditions. This kind of data is not present in generic databases since it requires long-time experimental campaigns and high investment of money.

The method has been validated with simulation and experimental results showing a good agreement between induced and estimated degradation.

In line with the recent expansion of IoT technologies for PV monitoring, the proposed approach represents a useful and relevant AI-based diagnosis tool that can be used to optimize operation and maintenance activities as well as enhance decision making processes, thus facilitating the integration of PV systems in smart grids.

It is worth noting that the idea proposed in the current chapter has inspired other research published later in different aspects. In [136] is presented a methodology that uses the closest information around the MPP as the starting point. In this case, the goal is to determine the presence of mismatch conditions for classifying the I–V curve as healthy or faulty. Furthermore, it exploits the reliability of the SDM for generating synthetic data. Finally, this paper agrees with the use of ANN as a suitable tool able to process the inputs and targets generated. Additionally, the paper COOP1 (from list of publications) also exploits points around MPP for detecting mismatch, especially due to partial shading conditions. Here, different machine learning techniques were used for assessing their performance in approximating the solution to this problem. The current thesis collaborated with the development of this paper with some basic ideas about the foundation of the problem and methodologies for taking experimental data. But, this paper is not covered in this document since the current thesis will aboard the same type of issues by applying a different innovative approach that uses frequency–domain techniques such as impedance spectroscopy.

Impedance Spectroscopy for Diagnosis of Photovoltaic Modules under Outdoor Conditions

4.1 Introduction

Photovoltaic (PV) panels operating under outdoor conditions inevitably generate degradation processes due to multiple reasons, such as operation in non–optimal conditions (e.g. partial shading, hot spots), and environmental conditions. These processes gradually decrease the performance of the PV devices leading to the reduction in power production, lifetime, and money earnings. These undesirable effects support the importance of early detection for planning the minimization of such outcomes [137].

In chapters 2 and 3, the proposed methodologies exploited the SDM for addressing the detection of degradation effects. Although the SDM can reproduce correctly the static I–V characteristic of a PV device, it cannot deal with its dynamic response, which requires an analysis in the frequency domain [138]. This analysis should provide additional information helping to better identify the degradation phenomena.

Many studies on PV panel degradation are performed in laboratory at cell level (Table 4.43), they have great validity, but only cover controlled conditions. In contrast, outdoor implementations have to deal with arbitrary meteorological conditions meaning a true–operating environment. Those operating conditions generate challenges linked to the temperature, irradiance, wind, humidity, and other factors that impact the PV performance, giving great importance to outdoor research studies. They will confront and assess the PV panel to the true–operative conditions while producing power [139, 140].

Thus, this chapter mainly contributes to validate the using of the EIS methodology

for commercial PV panels for detecting degradation effects under real–operating outdoor conditions. It means, there is no control over the environmental variables that continuously modify the PV panel operating point. Due to the strong sensibility of the PV panel impedance regarding the operating point, a method to correlate the measured impedance with the outdoor–operating condition is proposed. Hence, this work concentrates on performing the EIS methodology at the maximum power point (MPP) of the system since its impedance spectrum exhibits a particular correlation with the PV current and voltage measured in MPP.

This chapter has assessed the EIS methodology as a diagnosis tool by using simulations and experimental campaigns. The methodology has included series resistance degradation and mismatch conditions as the situations to study. Mismatching or mismatch conditions are referred to situations where the PV panels operate in non-optimal conditions leading to energy losses and reduced profit inducing early degradation of PV cells [141].

The mismatched effects, associated to the non-uniform operation of a single cell or groups of cells, can be induced by internal or external effects. Internal issues are associated with poor solder bonds, impurities in the silicon crystal, and failures. External problems could be linked to converter losses, irregular heat dissipation, obstructions such as trees, buildings, bird droppings, clouds, or dirt and dust accumulation. However, the main mismatch problems can appear with the shadows between panels or part of the same panel. Since shaded cells operate in the negative voltage region, thus with power dissipation, by-pass diodes are usually connected in parallel to small groups of cells inside the PV panel for mitigating the power dissipation. The presence of by-pass diodes leads to multiple MPPs and the MPPT tracker can stick in a local maximum by reducing the power production and accelerating the PV degradation process [142].

4.2 Impedance Spectroscopy simulations for partial shading detection

This section is aimed to demonstrate the usefulness of the EIS methodology for detecting and analyzing the mismatch conditions at the panel level without the scan of the I-V curve but only operating close the local MPP. The main benefit of this analysis is to detect the presence of multiple MPPs as soon as they appear, thus to perform the tracking of the GMPP only when is strictly necessary. Moreover, even if not afforded in this thesis, since the EIS spectra of PV panel is also affecting by the presence of by-pass diodes, the EIS analysis in presence of mismatch can be also used for the diagnosis of the by-pass diodes that are the mandatory devices to prevent the power dissipation of mismatched PV cells.

To the best author's knowledge this is the first attempt to apply the EIS methodology on these operating conditions, for this reason the initial analysis is carried out by electrical simulations. Thus, it will allow a fast assessment of the advantages and disadvantages of the methodology. Hence, this information will be relevant in a subsequent experimental stage.

This section is composed of three pieces that give a complete review of the argument described in the previous introduction. Subsection 4.2.1 is devoted to the construction of the dynamic model used to represent the PV panel including by-pass diodes. Subsection 4.2.2 shows the simulations of the equivalent electrical circuit representing the PV panel in uniform and mismatched conditions. Finally, subsection 4.2.3 reports the main results and discussion related to the analysis of partial shading conditions using EIS in simulations. Conclusions and improvements close the discussion of the arguments developed in this section.

4.2.1 PV panel modelling and circuit configuration

In order to analyse the dynamic behaviour of the PV panel, by-pass diodes must be also included. The analysis was carried out by using LTSpice because it accounts for all the electric characteristics of each element representing the circuit, including their intrinsic non-linearities. It is important because in this way the simulation will deliver trends and results close to the real behaviours.

In LTSpice, the SDM electrical circuit is used for representing the groups of cells connected in parallel to each by-pass diode. Fig. 4.40 illustrates the electrical configuration that represents a single panel composed of three groups of cells with their own by-pass diode used for protecting the cells from reverse polarisation.

Table 4.25. Kyocera KC175GHT-2 datasheet characteristics at STC and SDM parameters.

V_{oc}	29.2 [V]	**SDM**	I_{ph}	8.09 [A]
I_{sc}	8.09 [A]		I_s	2.0722 [nA]
MPP	23.6 [V], 7.42 [A]		η	1.0730
Thermal Coefficients	$\alpha_v = -109$ $[mV/°C]$, $\alpha_I = 3.18$ $[mA/°C]$		R_s	0.2185 [Ω]
Number of Cells	48		R_{sh}	93.0571 [Ω]

The parameters of the equivalent electric circuit shown in Fig. 4.40 are configured for modelling the Kyocera KC175GHT-2 PV panel and have been fixed according to the information given by the datasheet. Table 4.25 describes the electric characteristics given by the manufactures and the five parameters of the SDM tuned for representing 16 cells grouped in each module. Table 4.26 summarises

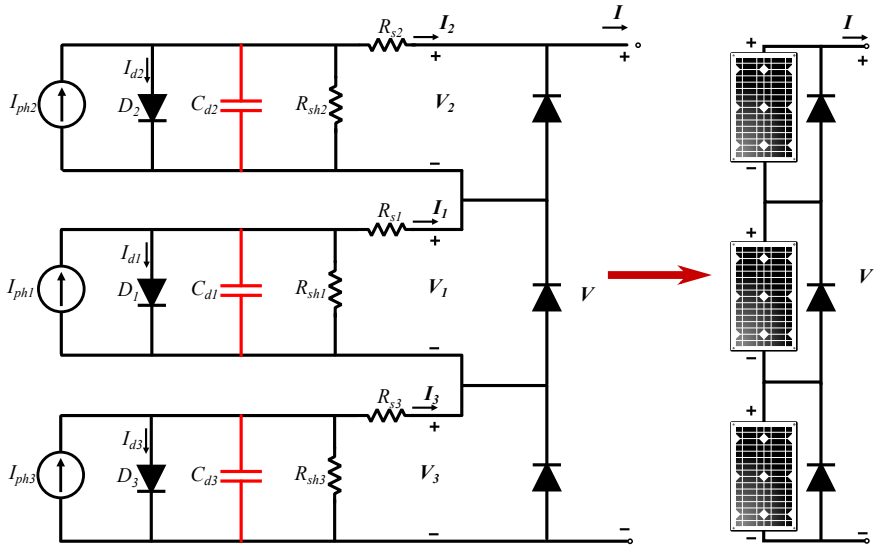

Figure 4.40. Module configuration by using SDM for simulation on LTSpice

Table 4.26. Characteristics of the by-pass diode VSB2045 (PV solar cell protection Schottky rectifier)

Characteristic	Value
Reverse breakdown voltage	45 [V]
Reverse breakdown current	23.4 [μA]
Zero-bias junction capacitance	2050 [pF]
High-injection knee current	20 [A]

the main characteristics of the by-pass diode model employed for this simulation. The VSB2045 by-pass diode is typically used inside the solar cell junction box for protection using DC forward current without reverse bias.It is worth to note that in this preliminary analysis, we used the parameters of a well know commercial panel which is used in several papers, thus the SDM static parameters might be considered well assessed.

The capacitance C_d has been chosen according to the values reported in Kumar et al [79]. Here, a single-crystalline silicon solar cell of (2x2) [cm^2] has been used for detecting the capacitance value. A C_p of 229.1 [nF] is obtained after different tests under multiple irradiance conditions. By assuming similar behaviour for the PV panel Kyocera KC175GHT-2 its internal capacitance can be estimated by accounting the linear dependency of capacitance with respect to the PV cell surface. Since the Kyocera KC175GHT-2 is characterised by cells of (15x15.5) [cm], a scaling factor of 58.125 must be applied. Moreover the SDM model is representing a series connection of 16 PV cells, thus the equivalent capacitance is

given by:

$$C_d = C_p * \frac{58.125}{16} \simeq 832nF \tag{4.55}$$

Although the estimated capacitance is not corresponding to the real capacitance of the selected panel, in absence of experimental data it will be considered a good approximation since it is referring to a PV cell of the same technology.

Fig. 4.41 depicts the outcome of the simulation for the LTSpice electric circuit in blue points and the SDM output (red points) calculated by means of equation (1.1). The small difference in the I-V curves obtained respectively with the model and the electrical circuit is justified by the fact that the model only uses the ideal behaviour of the diode while electric device simulation considers all the dynamics of it.

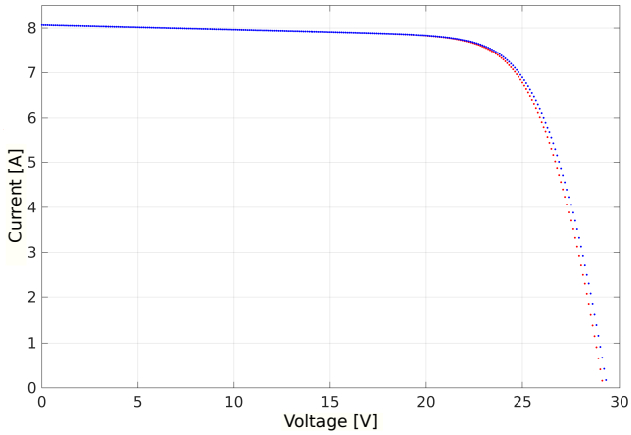

Figure 4.41. I-V curves of the Kyocera KC175GHT-2 using the SDM equation (red) and the LTSpice circuital setup (blue)

4.2.2 Simulation of the PV Module under Mismatched Conditions

For performing the EIS it is necessary to inject an AC stimulus into the device. Commonly, the amplitude must be in the range of few millivolts and the frequencies in a scale from 10 [Hz] to 100 [KHz]. This very small stimulus does not affect the normal operation of the device, thus for each frequency stimulus, the PV impedance value is calculated with equation (1.8) as described in section 1.5.2. The PV impedance spectrum can be then plotted for analyzing its behaviour and intrinsic characteristics [68], [66].

Although circuital solution for the EIS implementation on a PV panel are

appearing in literature [143], the analysis of the mismatching effects has been never faced. The PV circuit of fig.4.40 is configured as shown in Fig. 4.42 to perform the EIS in mismatched condition. In the scheme the sinusoidal current source is used for injecting the AC stimulus (S_2). It was set to 0.150 [A] with a range of frequencies between 10 [Hz] and 100 [KHz] on a logarithmic scale. The DC source (S_1) is used for polarizing the PV panel at different operating conditions.

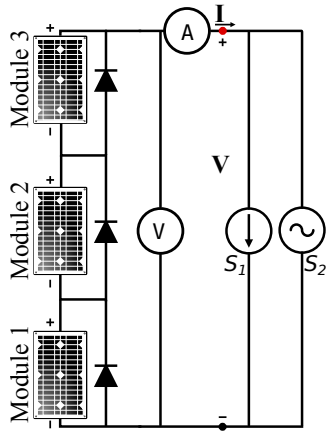

Figure 4.42. Scheme for the PV panel stimulation for performing the EIS.

The main contribution of this section is to show how it is possible to detect the presence of partial shading on the PV panel only by analysing the EIS spectra calculated around the MPP. It is worth to note that this information can be very useful for avoiding that the MPPT algorithm could be trapped in a local maximum [142]. For explaining this concept three cases with different working conditions have been fixed.

Table 4.27 summarises the information and parameters values for the three cases. In particular the first configuration refers to the uniform conditions where the currents of all modules have the same value. The second case illustrates a partial shading condition where one of the modules is generating the half value of the current compared against the other two modules. This could be associated to the typical condition induced by the partial shading where the shadowed part of the panel is subjected only to the diffuse solar radiation, that is significantly lower than the direct solar radiation. Finally, a case in a uniform low irradiance condition where the MPP point is similar to the one with mismatch conditions is tested.

Fig. 4.43 shows the simulated I-V curves of Kyocera KC175GHT-2 in uniform and mismatched condition. For the case #1 the PV panel is configured at the STC. It means that the whole panel receives homogeneous irradiation and the modules

Table 4.27. Testing cases for analysing the effect of mismatch on the EIS spectra.

Case	Condition	Configuration	MPP [V,A]	Power [W]
1	(STC)	$I_{Iph1} = I_{ph2} = I_{ph3}$=8.09A	[23.9, 7.38]	176,48
2	(**Mismatch**)	$I_{ph1} = I_{ph3}$=8.09A, $I_{ph2} = \frac{I_{h3}}{2}$	[15.10, 7.36], [25.8, 3.74]	111.28, 96.62
3	(Low irradiance)	$I_{ph1} = I_{ph2} = I_{h3}$=4.1A	[23.7, 3.62]	85.94

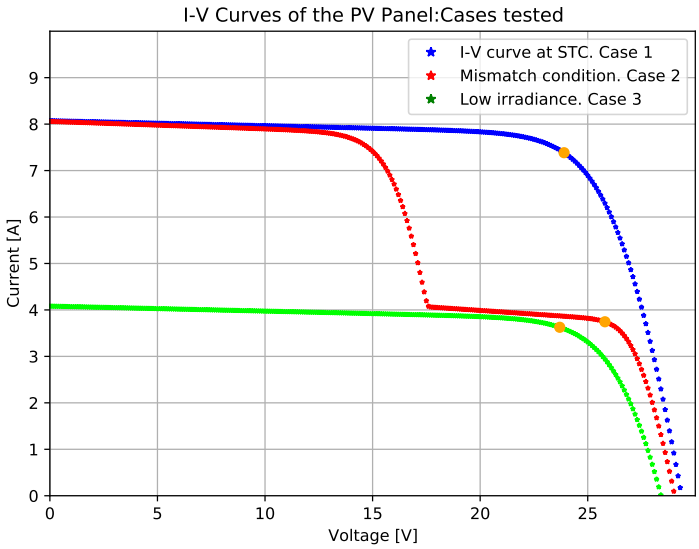

Figure 4.43. Simulated I-V curves of Kyocera KC175GHT-2 in uniform and mismatched condition.

generate the same amount of energy. In case #2 the low mismatch condition of module 2 is generating half of its nominal capacity. Here, the by-pass diode is active for protecting the panel and it generates an I-V curve with two possible MPP values (two knees). This deformation of the curve can affect the MPPT algorithm for searching the global maximum. For this analysis, the MPP was fixed at the second knee of the curve. Finally, case 3 represents a condition where all modules receive a homogeneous irradiance with low intensity. It is different from the mismatch case because the amount of energy produced is under normal conditions depending only on the amount of irradiance at that specific moment.

By comparing case #2 and #3 it is evident that they have very similar MPPs thus, without any additional information, the mismatched condition cannot be detected. The idea proposed in this thesis is to profit of the EIS analysis around the MPP to seek additional features able to differentiate remarkably the two cases, since they are completely different with respect to the environmental conditions.

4.2.3 EIS analysis and discussion of simulation results

The Nyquist plot in Fig. 4.44 illustrates the resulting impedance from case #1 at STC. According to the results achieved by Olayiwola et al [87], this behavior is in agreement with the typical conduct of a solar cell due to the curved shape obtained and the association of the trend and the frequency scale. Analyzing only the x-axis, points close to the origin represent outcomes for high frequency (until 100 [KHz]), while, the furthest points from it represent the values at low frequencies (from 10 [Hz]). The highest values in the real part of the impedance values are grouped at low frequencies. In contrast, this real part will decrease with higher frequency values.

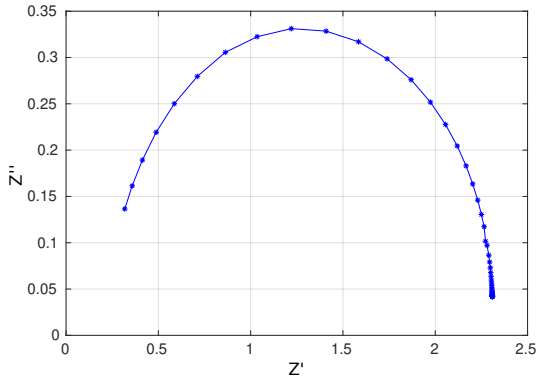

Figure 4.44. Impedance diagram at STC of the PV panel simulated with LTSpice

This response represents the ideal condition where the PV panel should remain for an optimal operation. But, environmental variations and mismatch conditions will always appear and will affect the behavior of the PV panel. Fig. 4.45 illustrates the comparison of the responses of the ideal case (Fig. 4.44) against the cases presented in Table 4.27 and Fig. 4.43.

Despite the MPP point of cases #2 (red points) and #3 (green points) are placed around the same coordinates in the I-V plane, the corresponding EIS spectra in the Nyquist plot exhibit different trends. For cases subjected to uniform condition (blue and green lines) the EIS spectrum changes due to uniform environmental fluctuations (irradiance variations). In particular the decrease in the irradiance level extends the arc and the impedance components (real and imaginary) will grow. In contrast, in presence of mismatch, the imaginary impedance component will decrease especially from medium to high frequencies. There is a considerable difference in the values of the imaginary components at STC or low-irradiance

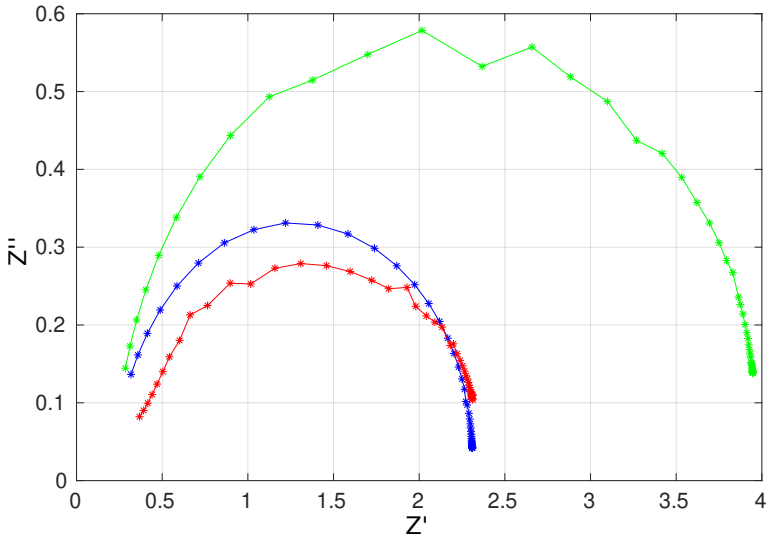

Figure 4.45. Comparison of impedances resulting from the studied cases of mismatching. Blue points represent the ideal state at STC. Green points show a normal operation under low irradiance conditions. Red points depict the mismatch condition presented in table 4.27.

conditions (blue and green points) against the mismatched points (red).

Another important aspect is related to the ending of the semicircles or arcs. The cases with uniform conditions (blue and green points) show a clear arc ending with close real and imaginary components at the highest frequencies. In contrast, the mismatch condition changes the ending of his semicircle and finishes with a different impedance value far from the typical values in uniform conditions.

Finally, Fig. 4.46 shows the EIS spectra for different irradiance conditions and mismatch levels. The red arcs refer to the mismatched cases, while the green ones are for the uniform conditions. The nominal current (I_n) represents the current at STC. For the cases with uniform conditions (green points), the I_n is the same for all the modules but divided by a factor. On the other hand, for mismatch cases (red points), the I_n expresses the current in the module affected by the shaded effect. Fig. 4.46 shows different trends between uniform and mismatched cases at the highest frequency points. There are two regions. The first one where all the uniform conditions arrive. The second one where the different levels of mismatch conditions converge. Therefore, there is a possibility of using the convergence of the values at medium and high frequencies for recognizing the state of mismatching.

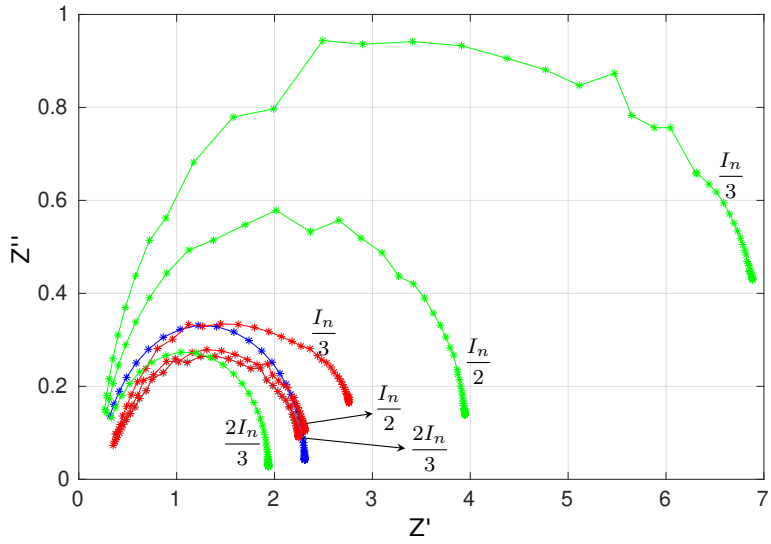

Figure 4.46. Variation of EIS for different levels of mismatch and low irradiance cases

In general, simulations of the PV modules based on the dynamic model of the SDM have allowed differentiating uniform operation from mismatch conditions. First, in uniform operation, the PV impedance increases its values according to the reduction of irradiance. This tendency is highlighted in Fig. 4.46 where the green arcs rise with decreasing values of current. In contrast, the red curves depict the characteristic trend of mismatching cases. Thus, a clear reduction of the impedance values is concentrated in a specific region at high frequencies. These two tendencies can help to separate and identify the mismatch cases for taking action about it.

The electrical simulations showed that the effects of partial shading conditions were notable in the impedance spectra captured using the EIS methodology. But, it is necessary to move forward to experimental analysis that supports the promising results obtained in simulations. The use of experimental campaigns could help to describe and connect the true values of the dynamic model elements with the degradation effects.

4.3 Measurement setup and EIS data validation

4.3.1 Configuration of the EIS instrumentation

The measurement system, provided by *Biologic* manufacturer [144], is composed of a EIS analyzer (SP-200) able to perform EIS analysis from 10 μHz up to 7 MHz interfaced with a booster (HCV-3048) supplying up to 30 A at a voltage of 48 V. It is equipped with a visual interface that must be programmed with the measurement setup for performing the sequence of tests. Unfortunately, this interface did not offer the facility to perform automatically the EIS in MPP because it requires setting in advance the references (voltage for potentiostatic tests or current for galvanostatic tests) corresponding to the operating point in which the EIS has to be performed.

This issue has been fixed by adding a Python script that searches the MPP on the acquired I-V curve and set the corresponding voltage for the experimental EIS measure executed in sequence. It is worth noting that, manual identification of MPP might delay too much the EIS test by making it not coherent with the measured I-V curve.

Figure 4.47 presents the interface configuration box and the graphical results at the end of each test. Table 4.28 shows how the developed Python "Automator" works .

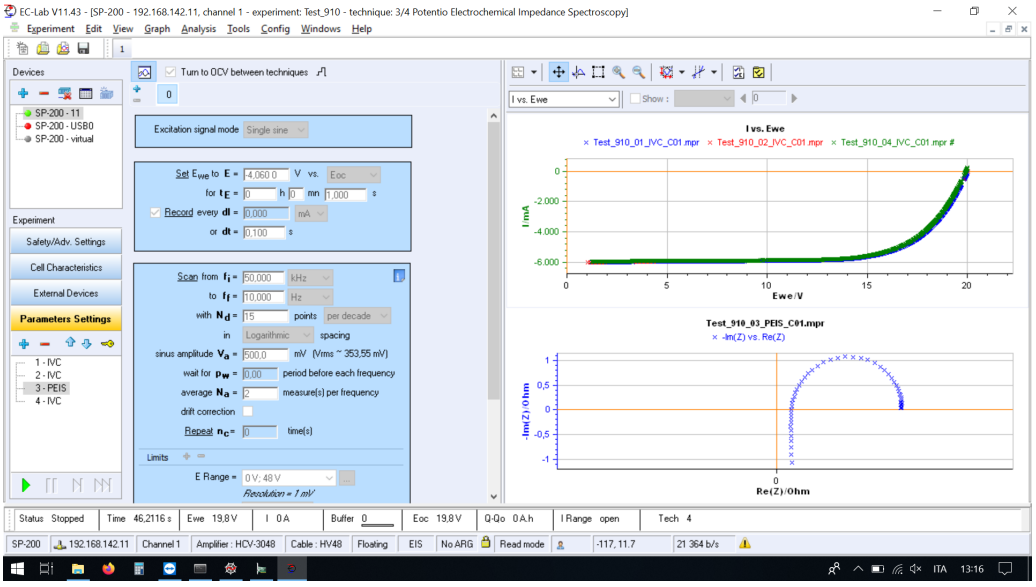

Figure 4.47. Biologic configuration tool

At the end of each test, a Matlab script is used to export the experimental data,

Execute Automator	
step 1	Configure the Biologic instrumentation for scanning the reference I-V curve
step 2	Search on the acquired I-V curve the point corresponding to the maximum power in which must be performed the EIS
step 3	Configure the Biologic instrument with V_{MPP} as reference voltage for the EIS measurement
step 4	Save data in an assigned folder

Table 4.28. Python Automator functions

which are available by the instrumentation software in a proprietary format, in a MATLAB data structure. Table 4.29 shows an example of the data structure associated with each I-V curve scan. Table 4.30 shows how are collected the data for the EIS experiment. The environmental conditions (G and T) are reported in both data structures because they are acquired at the beginning and the end of each test, and they could vary during the I-V scan and EIS measure. The comparison among that environmental data are used to validate the coherence among the two types of experimental test. If the environmental conditions are changing during two consecutive tests, the I-V curve and the corresponding EIS spectrum are discarded.

The data structures also contain two vectors with the results of the parameters identification process associated respectively to the PV static model (SDM=Single Diode Model) and the one associated to the dynamic model (CPE=Constant Phase Element). Details on the methods used to calculate the parameters of the static and dynamic model have been provided in the modelling sections.

dataIV	
panelName:	'PV_Series'
NameIVFile:	'Test_43_01_IVC_C01.txt'
Date:	'20/12/2021'
Voltage:	[312×1 double]
Current:	[312×1 double]
Isc:	3.0294
Voc:	19.923
Vmpp:	17.305
Impp:	1.9324
numCells:	32
timestamp_initial_final:	{2×1 cell}
G_IV_PV1_initial_final:	[557.72 559.57]
T_IV_PV1_initial_final:	[38.912 38.915]
G_IV_PV2_initial_final:	[395.51 396.88]
T_IV_PV2_initial_final:	[35.072 35.065]
SDM_Params:	[5×1 double]

Table 4.29. Data structure for the I-V curve measurements

dataEIS	
panelName:	'PV_Series'
NameEIS:	'Test_43_03_PEIS_C01.txt'
Date:	'20/12/2021'
frequency:	[74×1 double]
real:	[74×1 double]
imaginary:	[74×1 double]
Voltage:	[74×1 double]
Current:	[74×1 double]
timestampEIS_init_middle_final:	{3×1 cell}
G_EIS_PV1_init_middle_final:	[560.5 557.35 554.9]
T_EIS_PV1_init_middle_final:	[38.968 38.318 37.991]
G_EIS_PV2_init_middle_final:	[397.01 394.99 393.16]
T_EIS_PV2_init_middle_final:	[35.106 34.534 34.37]
CPE_Params:	[6×1 double]

Table 4.30. Data structure of the Impedance Spectroscopy measurements

4.3.2 Experimental Platform Description

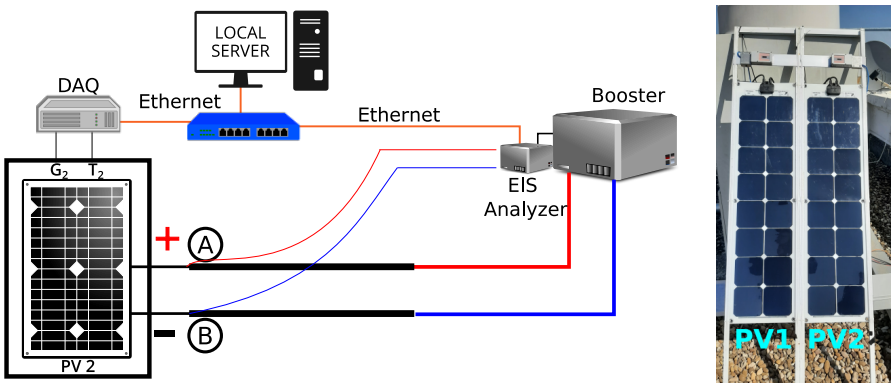

(a) General diagram

(b) Physical PV arrangment

Figure 4.48. Hardware setup arranged for the experimental process.

Fig. 4.48 presents the setup employed for characterizing a commercial single-crystalline silicon PV module placed on the roof of the *Engineering Building* of the *University of Salerno* (Italy). The main features of this PV module can be seen in Table 4.31 [145]. A sensor for measuring the irradiance G [W/m^2] on the plane of the solar module is connected to the measurement system (see the technical information in [146]). In addition, a temperature probe [147] is also attached on the module back surface to measure the cell temperature T [°C]. Table 4.32 summarizes the technical information of these sensors.

Table 4.31. Nominal parameters of the Solbian FLEXSP50L PV panel

Parameter	Value
Peak Power (+/- 5%) - $P_{\max}$	51 [W]
Rated Voltage - V_{mpp}	9.0 [V]
Rated Current - I_{mpp}	5.7 [A]
Open–Circuit Voltage - V_{oc}	10.9 [V]
Short–Circuit Current - I_{sc}	6 [A]
Temp. coeff. P_{mpp}	-0.38 [%/°C]
Temp. coeff. V_{oc}	-0.27 [%/°C]
Temp. coeff. I_{sc}	0.05 [%/°C]
Lenght	43.66" (1109 mm)
Width	11.50" (292 mm)
Thickness	0.079" (2 mm)
Weigth	1.76 lbs (0.8 kg)
Number of cells	16

Table 4.32. Basic information of the environmental sensors used for sensing the ambient conditions.

Sensor	Litemeter LM1-10V PRO	
Output	2 analog channels	
Input Range	Irradiance	$0 \rightarrow 1200$ [W/m^2]
	Spectral Range	$0.3 \rightarrow 1.1$ [μm]
	Temperature	$(-30) \rightarrow (+85)$ [°C]
Output	Irradiance	$0 \rightarrow 10$ [V] for $0 \rightarrow 1200$ [W/m^2]
	Temperature	$0 \rightarrow 10$ [V] for $(-20) \rightarrow (+80)$ [°C]
Output precision	Irradiance	$\pm 3.5\%$
	Temperature	± 1.5 [°C]
	Response time	<100 [ms]
Supply		$12 \rightarrow 30$ VDC
Sensor	Texas Instruments LM35	
Output	1 analog channel	
Input Range	Temperature	$(-55) \rightarrow (+150)$ [°C]
Output	Voltage	$(-1) \rightarrow (+6)$ [V]
	Current	10 [mA] (max)
Output precision	Temperature	± 0.5 [°C]
Supply		$4 \rightarrow 30$ VDC

A DAQ system monitors the environmental variables and saves them in a database placed on a local server with a sampling frequency of 1 s. Additionally, the EIS analyzer is connected to the local server through an Ethernet communication for controlling the test and saving the data.

It is worth to note that, although the EIS equipment is a laboratory testing system, the proposed configuration performs an impedance analysis in a real scenario. Firstly, using an outdoor experimental platform for providing the EIS spectrum under non–controlled environmental conditions (irradiance and temperature) that a solar panel could find in a real PV system. Secondly, utilizing low–cost sensors for acquiring the data. Naturally, for arriving to the on–board implementation

of the EIS technique the lab equipment must be replaced with another hardware implementation.

Currently, different works have demonstrated that the EIS technique can be carried out using the same DC–DC converter present in standard PV installations [73, 83, 143]. Thus, the spotlight of this research work is not focused on hardware development. On the contrary, it seeks to exploit the EIS analysis for diagnosis purposes and degradation effects in real systems at the PV panel level working in real–outdoor conditions.

4.3.3 Selection of the operating point for measuring stable EIS spectra

During the outdoor EIS measurements, the environmental conditions are not controlled, thus, some preliminary analysis are performed for discarding noisy spectra. EIS measurements are considered reliable if were acquired in stable environmental conditions. This is checked by verifying that current and voltage are confined in a small range of variation during the EIS test, nevertheless the PV operating point could be different for each EIS test. Additionally, as discussed in section 4.3.4, the well-known Kramers–Kronig test was used for validating the quality of the experimental impedance measurements [66, 70, 148].

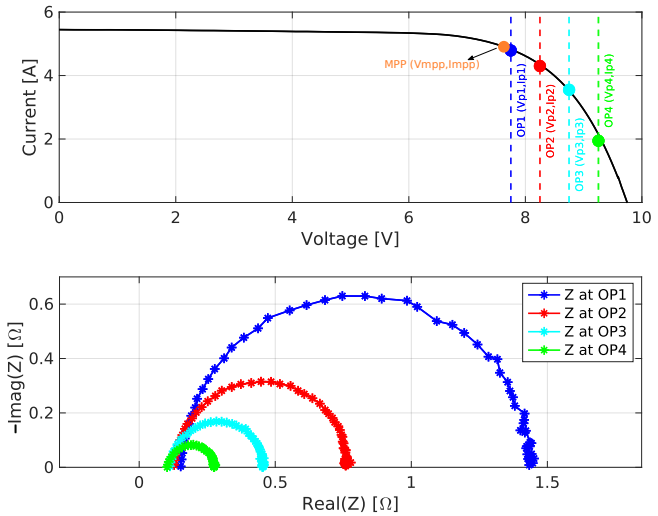

Figure 4.49. Relationship between the I–V curve and the impedance values in the complex plane with different operating points at a particular environmental condition ($G = 951$ W/m^2 and $T = 52$ °C).

Fig. 4.49 shows four PV panel operating points of the I–V curve (upper plot) where the EIS methodology is applied and their respective impedance spectra are

measured (lower plot). The inductive effect, as shown in Fig. 1.8, is not plotted for a better visualization of impedance semi–arcs appearing in the first quadrant of the complex plane. In these tests the reduction in the real and imaginary parts visible in the impedance spectra is only related to the operating point changes from V_{mpp} to the V_{oc}. In fact, [149] demonstrates that increments in the polarization voltage increase the junction capacitance and decrease the cell dynamic resistance. The cell dynamic resistance decrement is evident in the measurements close to zero frequencies ($\omega \approx 0$), while the increment in the junction capacitance produces smaller impedance values due to the equivalent impedance of the capacitance ($Z_c = 1/j\omega C$).

The obtained impedance spectra are not comparable among them since the working conditions affect significantly the parameters of the PV dynamic model [66]. In [148], a study performed in perovskite solar cells showed the same trend, reaching huge impedance values when the system was setting very close to the I_{sc}.

In Fig. 4.49, no EIS spectrum was measured at the left side of the MPP point because at outdoors is almost impossible to have a perfectly constant irradiance condition and, as a consequence, a clean EIS measurement in the left part of the *I–V* curve. Here the current is almost independent on the voltage and strongly sensible to the irradiance, thus EIS will provide noisy spectra not useful for diagnostic purposes.

The choice of the operating point is the first issue that must be solved when the EIS technique is applied for outdoor measurements instead of lab test.

In [148], an analysis concerning the relationship between solar cell operating points and the EIS methodology is carried out. It concludes that the open–circuit voltage (V_{oc}) is the most suitable point because it fulfills the best conditions in terms of linearity and stability. Although the V_{oc} is the most recommended operating point for assessing the EIS methodology, it is not convenient in practical applications where PV panels are usually connected to power electronics for performing the Maximum Power Point Tracker (MPPT) algorithm that allows to maximize the power production. Therefore, useless modifications of its working conditions are not justified since the system could have power and money losses when it goes far from the MPP state. Regarding the MPP, it is stated that it is the most interesting but challenging point due to the high sensibility of the impedance spectra with respect to the operating point. Indeed, by comparing the impedance spectra in OP1 and OP2 of Fig. 4.49, there is a significant change in the impedance response over a small variation of the operating point. From a diagnostic point of view, the exact knowledge of the EIS operating point is fundamental for distinguishing the variations in the impedance parameters due to the PV degradation phenomena with respect to the intrinsic variation caused by the environmental conditions or to the changes in the operating point.

In this sense, the MPP is the best choice since in normal operation of the PV systems the voltage and current are constantly measured and the MPPT algorithm operates for staying continuously close to the V_{mpp} and I_{mpp} values.

Moreover, MPP is the only point that benefits of the property that the differential resistance ($\partial V/\partial I$), which in the static PV small signal model, is equal to the ratio $R_{mpp} = V_{mpp}/I_{mpp}$. This property is a direct consequence of the maximum power condition $\partial P/\partial V = 0$ that is valid only in MPP. In whichever other operating point, the differential resistance is a complicated expression derived by the SDM equation. More details on the PV panel differential resistance can be found in [150].

The MPP property can be exploited to verify if the EIS spectra is effectively measured in that operating point. Indeed, under the assumption that the impedance value, associated to the PV dynamic model of Fig. 1.6 and calculated at zero frequency ($Z_{eq}(0)$), must converge to the differential resistance R_{mpp}, the following condition must be fulfilled:

$$Z_{eq}(0) = R_0 + R_1 \simeq R_{mpp} = \frac{V_{mpp}}{I_{mpp}} \tag{4.56}$$

In this work it will be verified that the previous test allows to validate that different spectra, acquired along the time, are always associated to the MPP operating point. The choice of the operating point is also linked to the configuration of the perturbation signal. According to [66], a rule for fixing the amplitude of the small input signal is 1%–2% of the V_{bias}. In this work, taking into account that V_{bias} corresponds to the V_{mpp}, 100 mV was the amplitude established for performing the EIS analysis.

4.3.4 Reliability of the spectra at MPP

Previously, the condition for assuring the reliability of the spectra regarding the operating point was defined. However, it is also necessary to evaluate the quality of the impedance spectra estimated at that operating point.

Kramers–Kronig test is a consolidated method for validating the quality of the experimental impedance measurements based on four criteria as *Linearity*, *Causality*, *Stability*, and *Finiteness*. If the system fulfills these criteria, the relations (4.57)-(4.58) allow calculating the real part of a complex system using only the imaginary part and vice-versa [66, 70, 148].

$$Z_{Im}(\omega) = -\frac{2\omega}{\pi}\int_0^\infty \frac{Z_{Re}(x) - Z_{Re}(\omega)}{x^2 - \omega^2}\, dx \tag{4.57}$$

$$Z_{Re}(\omega) = R_{\infty} + \frac{2}{\pi}\int_{0}^{\infty} \frac{xZ_{Im}(x) - \omega Z_{Im}(\omega)}{x^2 - \omega^2}\, dx \tag{4.58}$$

The difficulty of covering the infinitive integration limits in these equations for experimental measurements has made the authors search for alternative approaches for overcoming these issues. The "Lin–KK tool" [151] is an alternative tool that allows assessing the experimental data for qualifying the integrity of the data [152], [153]. This tool evaluates the reproducibility of the experimental impedance data using a KK compliant equivalent circuit model (ECM) of series connected RC elements. If there is a combination of RC circuits able to fit the experimental data, then this data describes a time–invariant system. The quantification of the data integrity is expressed using the percentage of residuals that are deviations between the experimental data and the Kramers–Kronig ideal fitted spectrum for the real and imaginary parts. In general, some cases can appear for assessing the data. First, the smaller the residuals, the better the spectrum quality. Secondly, noise–like residual can emerge and indicate noise in the measurements, but, this is a normal condition in experimental measurements. On the contrary, if biased residuals arise especially at low frequencies, it could mean time–variances in the system and the spectrum is likely invalid [154].

Then, for assessing the validity of the measurements at the chosen operating point, the Kramers–Kronig analysis was tested using the Lin–KK tool at V_{oc} and MPP. The V_{oc} point is used as a reference since this operating point theoretically is the most suitable point.

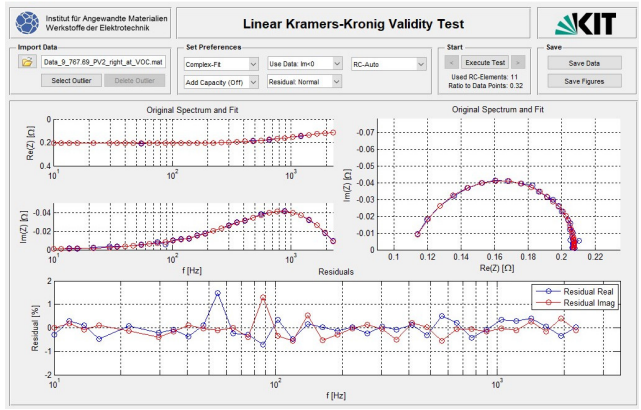

Figure 4.50. Validation of the Lin-KK tool for a impedance measurement at V_{oc}

Fig. 4.50 illustrates the validation of an experimental measurement at V_{oc}. The real and imaginary parts are well–fitted. The semicircle is well reconstructed using 11 RC circuits. The residuals are small, and the trends do not show considerable bias deviation. It indicates a good quality of the experimental impedance

measurement. This behavior is in line with the considerations expressed in [154] and the aforementioned features regarding the suitability of V_{oc} as operating point for implementing EIS measurements.

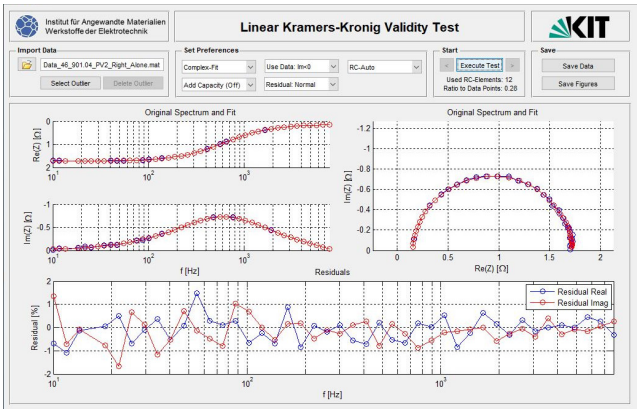

Figure 4.51. Validation of the Lin-KK tool for a impedance measurement at MPP.

Fig. 4.51 display the Lin–KK test at the MPP. In this case, the residuals are higher than the ones obtained with V_{oc} as operating point. Both residual trends (real and imaginary) show noise in the measurements, especially at low frequencies, but still acceptable since they are less than 1% for almost all the frequency range. However, there is not a biased tendency because all data is around zero. According to the technical report of the Lin–KK tool [154], noisy spectra are normal, and they can represent a time–invariant system. Thus, the data captured for this work is valid for continuing to analyze the dynamic of the PV panel.

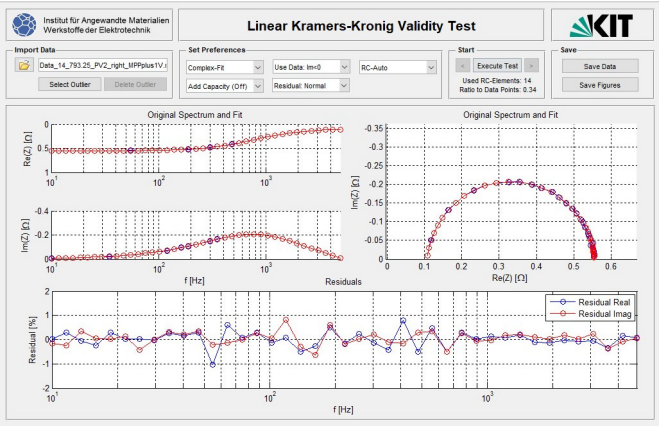

Figure 4.52. Validation of the Lin-KK tool for impedance measurements at (MPP + 1 [V])

Fig. 4.52 presents an operating point placed 1 [V] ahead of the MPP. In general,

there is no bias tendency, and the residual percentage is small. There are a few points that contain noise. As a result, the system can be considered time–invariant and fulfill the Kramers–Kronig conditions. Thus, the Lin–KK tool helped to verify the quality of all the measured impedance spectra of this implementation.

4.4 Impedance spectroscopy for online series resistance monitoring

Section 4.2 simulated the study of partial shading conditions employing PV modules in series, but, before arriving at that level of complexity, the first EIS experimental campaigns are referred to a single PV module. The first experimental analysis not only allowed to understand the most basic implications of the dynamic behaviour for the PV module under test, but also to connect the dynamic analysis provided in this chapter with the research activity discussed in the previous ones, where the performance evaluation of PV panel is done through the static Single Diode Model [155, 156]. In particular section 1.3.2 shown the relevance of estimating the R_s as a parameter that can reveal important degradation effects in PV devices.

This section shows that the measured impedance spectrum in MPP allows for building an accurate identification of the series resistance (R_s) degradation by using the PV small–signal dynamic model and the EIS technique.

As already highlighted previously, methods proposed in the literature commonly need to measure the whole I–V curve or part of it to estimate R_s through static models, e.g, the SDM. These methods require to bias the system far from the MPP with energy and money losses, as well as negative impact on the electronic system equipment due to the frequently changes in the operating conditions. On the contrary, the EIS methodology estimates the series resistance without changing the operating point, thus still working in MPP. To the best of authors' knowledge, this is the first time that the series resistance degradation is estimated by using only the impedance spectrum measured at MPP.

4.4.1 Analisys of experimental EIS for a single PV module

For analyzing the degradation effects caused for variations in the series resistance, an external resistor of $\Delta R = 0.175\ \Omega$ was connected to the PV module terminals. This value has been chosen as a testing case because it produces a PV power loss of about 8% at high irradiance ($G \geq 750\ \mathrm{W/m^2}$), thus might be assumed, for the module under test, as a reference value for considering the PV module in a degraded condition. The experimental EIS spectra obtained by the PV module at nominal conditions (without the external resistor) against the EIS measurements

with the external resistance was analyzed and fitted with the PV dynamic model for detecting the ΔR value.

Just before every EIS measurement, an I–V curve measurement is acquired. This is used for settling the EIS system to operate at MPP. Additionally, the experimental I–V curve allows to identify the parameters of the classical SDM and, in particular, the series resistance value (R_s) that is used as reference for comparing the resistance variation obtained with the EIS analysis.

Table 4.33. Parameter estimation by using the CPE model at MPP under different irradiance levels.

Environmental Data			**EIS (Dynamic Model)**						**I–V Curve Data**		
#	G [W/m^2]	T[°C]	L [H] ± CI[%]	$R_0[\Omega]$ ± CI[%]	$R_1[\Omega]$ ± CI[%]	Q ± CI[%]	β ± CI[%]	C_{eq}[F]	V_{mpp}[V]	I_{mpp}[V]	$R_s[\Omega]$ ± CI[%]
1	245	23.2	2.19E-06 ± 1.7	0.270 ± 4.2	10.917 ± 1.1	4.04E-05 ± 5.8	0.955 ± 0.7	2.80E-05	8.669	0.840	0.305 ± 10.2
2	286	23.4	2.28E-06 ± 2.2	0.232 ± 7.5	9.149 ± 3.3	6.59E-05 ± 11.8	0.913 ± 1.3	3.26E-05	8.783	1.044	0.258 ± 9.5
3	348	25.2	2.23E-06 ± 1.7	0.200 ± 13.7	6.481 ± 3.6	7.77E-05 ± 15.4	0.934 ± 1.7	4.55E-05	8.784	1.422	0.217 ± 6.5
4	400	25.6	2.12E-06 ± 3.8	0.188 ± 5.8	4.956 ± 1.7	9.73E-05 ± 12.6	0.939 ± 1.4	5.90E-05	8.778	1.724	0.175 ± 7.1
5	448	28.9	2.13E-06 ± 2.2	0.169 ± 2.8	3.823 ± 1.2	1.19E-04 ± 8.6	0.948 ± 1.0	7.84E-05	8.660	2.176	0.133 ± 6.0
6	482	28.7	2.17E-06 ± 2.8	0.166 ± 2.3	3.337 ± 0.9	1.31E-04 ± 6.3	0.949 ± 0.7	8.61E-05	8.602	2.435	0.146 ± 6.2
7	535	30.7	2.16E-06 ± 2.4	0.168 ± 2.4	3.025 ± 1.2	1.79E-04 ± 6.8	0.902 ± 0.8	7.95E-05	8.472	2.705	0.108 ± 5.6
8	599	33.6	2.01E-06 ± 2.8	0.154 ± 9.9	2.766 ± 2.1	3.86E-04 ± 16.7	0.817 ± 2.1	8.35E-05	8.385	3.022	0.070 ± 5.7
9	631	33.8	2.02E-06 ± 2.7	0.154 ± 8.7	2.613 ± 2.8	3.64E-04 ± 17.2	0.835 ± 2.1	9.18E-05	8.351	3.163	0.071 ± 4.2
10	754	34.2	2.04E-06 ± 2.5	0.148 ± 5.5	2.065 ± 1.9	3.68E-04 ± 19.0	0.852 ± 2.3	1.06E-04	8.364	3.863	0.055 ± 4.5
11	878	37.2	1.84E-06 ± 2.3	0.145 ± 1.7	1.679 ± 1.7	2.34E-04 ± 8.6	0.935 ± 1.1	1.36E-04	8.272	4.502	0.050 ± 3.0
12	908	42.3	2.10E-06 ± 2.3	0.143 ± 2.0	1.657 ± 1.7	1.93E-04 ± 10.8	0.973 ± 1.3	1.55E-04	8.143	4.794	0.046 ± 3.3

Table 4.33 and Table 4.34 show the parameters of the dynamic model of Fig. 1.6 found by using a fitting procedure. The first column is the identifier of every test. For each testing condition, the confidence intervals of the parameters (expressed as a percentage of variation with respect to the nominal value) are relatively low by assuring a well fitted model. Table 4.33 presents the parameters values at nominal conditions whereas Table 4.34 represents the parameters values with the additional external resistance ΔR. The information regarding the environmental conditions, the MPP coordinates and R_s estimated by fitting the I–V curve with the single-diode model are also listed in the tables.

By comparing the estimated inductance in the two testing conditions is easy to justify the increase of L in presence of the external resistance. Indeed, the ΔR is connected to the commercial PV module through a further MC4 connector that is in series to the system under test, thus by increasing the parasitic inductive effect.

For confirming that the EIS spectra have been really performed at MPP, the

Table 4.34. Parameter estimation by using the CPE model at MPP under different irradiance levels with an additional external resistor.

Environmental Data			EIS (Dynamic Model)						*I–V* Curve Data		
#	G [W/m^2]	T[°C]	L [H] ± CI[%]	$R_0[\Omega]$ ± CI[%]	$R_1[\Omega]$ ± CI[%]	Q ± CI[%]	β ± CI[%]	C_{eq}[F]	V_{mpp}[V]	I_{mpp}[V]	$R_s[\Omega]$ ± CI[%]
1	250	22.4	3.61E-06 ± 1.7	0.456 ± 4.7	9.940 ± 5.1	4.43E-05 ± 14.1	0.949 ± 1.4	2.93E-05	8.505	0.853	0.479 ± 4.4
2	334	25.4	3.57E-06 ± 1.3	0.396 ± 3.3	6.012 ± 1.0	6.79E-05 ± 6.0	0.966 ± 0.7	5.18E-05	8.421	1.344	0.381 ± 3.4
3	420	27.5	3.58E-06 ± 1.0	0.365 ± 1.4	4.172 ± 1.0	9.34E-05 ± 5.8	0.968 ± 0.6	7.20E-05	8.315	1.877	0.326 ± 2.6
4	520	30.3	3.28E-06 ± 5.9	0.343 ± 3.8	2.975 ± 1.5	1.42E-04 ± 10.6	0.960 ± 1.4	1.02E-04	8.182	2.511	0.297 ± 2.0
5	650	30.5	3.30E-06 ± 1.1	0.330 ± 1.5	2.232 ± 1.1	1.84E-04 ± 7.7	0.958 ± 0.9	1.31E-04	8.037	3.267	0.269 ± 1.9
6	755	34.6	3.39E-06 ± 2.8	0.325 ± 1.8	1.867 ± 1.2	2.30E-04 ± 8.8	0.953 ± 1.0	1.57E-04	7.801	3.860	0.252 ± 1.2
7	828	39.7	3.36E-06 ± 3.3	0.317 ± 2.3	1.583 ± 1.8	2.81E-04 ± 13.5	0.943 ± 1.8	1.77E-04	7.616	4.220	0.248 ± 1.0
8	886	35.6	3.35E-06 ± 3.6	0.319 ± 2.3	1.416 ± 1.5	2.38E-04 ± 13.2	0.968 ± 1.7	1.83E-04	7.676	4.487	0.242 ± 0.8
9	975	38.6	3.24E-06 ± 4.6	0.318 ± 1.8	1.259 ± 1.1	3.11E-04 ± 13.4	0.949 ± 1.9	2.04E-04	7.517	4.836	0.229 ± 0.4
10	1028	38.5	3.17E-06 ± 5.6	0.318 ± 1.9	1.219 ± 1.5	2.71E-04 ± 15.2	0.969 ± 1.7	2.10E-04	7.487	5.084	0.231 ± 0.6

condition expressed in Eq. 4.56 is evaluated by using the values reported in Table 4.33 and Table 4.34. Fig. 4.53 shows the R_{mpp} values calculated by using the experimental (V_{mpp}, I_{mpp}) data (red points). Blue markers are the values of the dynamic CPE model calculated at zero frequency $Z_{eq}(0) = R_0 + R_1$.

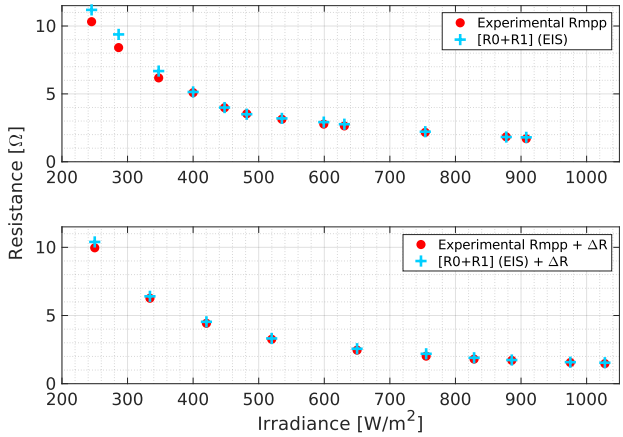

Figure 4.53. Comparison of the experimental R_{mpp} values and the impedance ad zero frequency using the CPE model. Upper plot: PV module at nominal conditions. Lower plot: PV module with the external resistor.

The percentage error among R_{mpp} and $Z_{eq}(0)$ for the medium and high irradiance is very small, less than 2% for both nominal condition and in presence of ΔR. At low irradiance, as visible in the Fig. 4.53, the maximum percentage error is respectively 11.5% for the nominal condition and 8.4% with ΔR. This discrepancy

is justified by the difficulty of finding exactly the MPP at low irradiance because the power versus voltage curve is flat around the MPP and, due to the finite resolution of the measurement system, small differences can be introduced in settling the operating point during the EIS. If the error at low irradiance is considered unacceptable such measure should be discarded. In the following, all the measurements shown in Fig. 4.53 are assumed to be valid, thus the dynamic CPE model is considered properly tuned for describing the behavior of the PV module at MPP for both cases, nominal condition, and with the additional resistance in the full range of the environmental conditions. It is worth to note that the data required to perform this test are only the EIS spectra and the measured voltage and current, thus it is suitable for the on-board execution giving the possibility to guarantee the coherence of the experimental EIS data with the MPP operation with a simple check.

4.4.2 Identification of the series resistance degradation

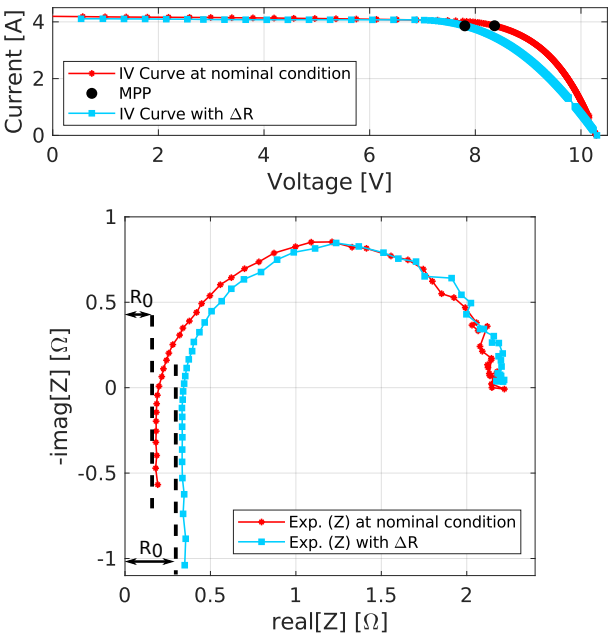

Figure 4.54. Comparison of test cases #10 (red markers) and #6 (blue markers) from Tables 4.33 and 4.34 respectively.

Fig. 4.54 graphically illustrates the effect of series resistance degradation in the I–V curves (upper plot) and the impedance values measured with the EIS methodology (lower plot) in the same environmental conditions. It is well-known that an increase in the series resistance impacts on the slope of the I–V curve in

proximity of V_{oc}, which is reflected on a displacement of the MPP. Differently, the impact of the series resistance variation produces an horizontal translation on the impedance spectra, that is visible at high frequency and mainly affects the R_0 value.

The identification of the series resistance degradation by using the I–V curves requires to measure voltage and current around V_{oc} for calculating the slope of the I–V curves and then estimates the R_s variation. On the contrary, the EIS methodology requires only to estimate the parameters of the PV dynamic model by using the impedance spectra measured at MPP and then approximate the series resistance degradation through the R_0 parameter variation.

A further experimental campaign has been carried out on the PV panel under test by performing the impedance measurement in different points of the right part of the I–V curve. Both healthy (nominal) and degraded conditions were analyzed. Fig. 4.55 shows the values of the CPE dynamic model parameters for the PV panel operating in healthy and degraded condition for different operating points spreading from V_{oc} up to the left of MPP.

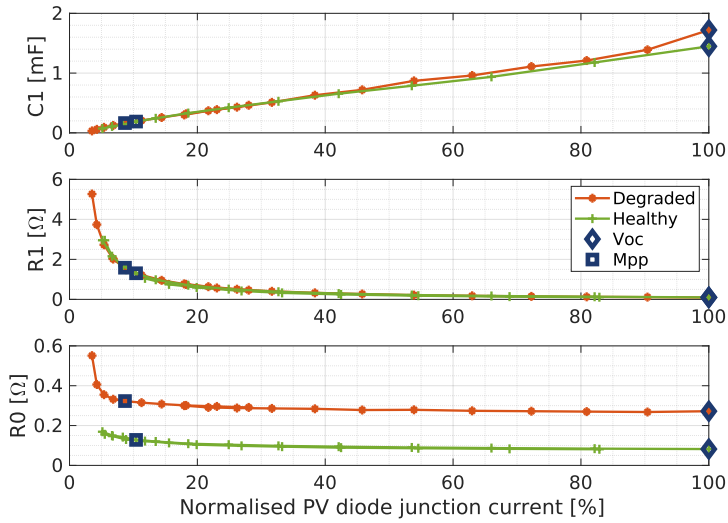

Figure 4.55. Parameters variation of the CPE dynamic model as function of the operating point of the I–V curve

It is worth to note that the additional series resistance change the slope of the I–V curve by making not comparable the impedance spectra for the same testing point when the panel operates in healthy or emulated degraded condition, for this reason the parameters have been plotted as function of the normalized current flowing in the p–n junction. The latter is calculated as the difference between the short–circuit current and the current delivered by the PV panel for each point of the I–V curve where the impedance spectrum has been measured.

The graphs clearly show how the additional resistance only impact on the R_0 parameter how already confirmed by the analysis performed only in the MPP point.

For forward biased solar cells the capacitive effect is dominated by the diffusion capacitance [63], which is linear with respect to the current flowing in the p–n junction, as confirmed by C_1 plot in Fig. 4.55. As concerns the resistive effect of the p–n junction, which is described by the R_1 parameter, the plot of Fig. 4.55 clearly put into evidence that its variation is much more pronounced around the MPP, thus it is expected that it could be a further indicator for detecting other degradation phenomena when the solar cells operate in MPP.

Table 4.35 shows a comparison of the series resistance for the cases with and without the external resistor having similar irradiance and temperature conditions. These three values gives a preliminary analysis at low, medium, and high irradiance levels. The change expressed by the dynamic CPE model in its R_0 parameter shows a better estimation of the true additional resistance ($\Delta R = 0.175\ \Omega$).

Table 4.35. Preliminary comparison of the series resistance variation found by the SDM and the dynamic CPE model.

Additional Resistance				**Nominal Case**				**Variation**	
G [W/m^2]	T [°C]	$R_s[\Omega]$	$R_0[\Omega]$	G [W/m^2]	T [°C]	$R_s[\Omega]$	$R_0[\Omega]$	$\Delta R_s[\Omega]$	$\Delta R_0[\Omega]$
250	22.4	0.479	0.456	245	23.2	0.305	0.270	0.174	0.186
520	30.3	0.297	0.343	535	30.7	0.108	0.168	0.189	0.175
886	35.6	0.242	0.319	878	37.2	0.050	0.145	0.192	0.174

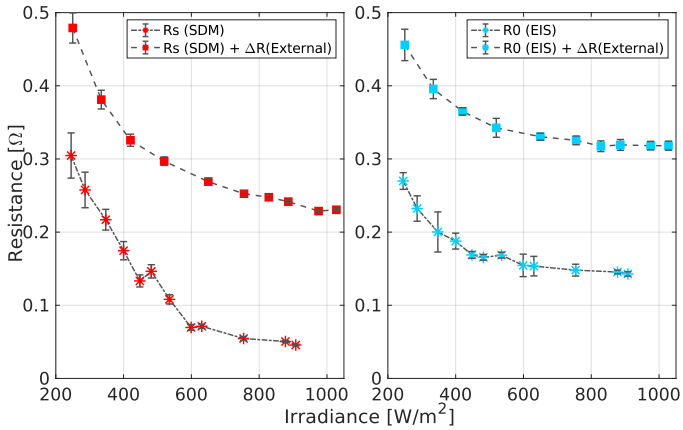

Figure 4.56. Left plot: R_s estimated by using SDM. Right plot: R_0 estimated by using EIS spectra. The asterisks refer to the parameters in nominal conditions. The square markers refer to the tests with the external resistance.

Fig. 4.56 shows the trend of the series resistance parameters R_s and R_0

evaluated by fitting the static model (SDM) and the dynamic model (CPE model) respectively with the *I–V* curves and the EIS spectra in the different environmental conditions reported in Table 4.33 and Table 4.34. All the values display the confidence interval given by the fitting procedure. Despite the resistance values obtained from the static (SDM) and dynamic models cannot be directly compared because derived from different experimental data, both recognize a similar degraded effect introduced by the external series resistance. The difference in the series resistance estimation is also justified by the fact that the two models describe different characteristics of the PV module. Indeed the SDM reproduces the static non-linear behavior and its *I–V* profile using some non-linear elements as a diode. In contrast, the CPE model is a dynamic small signal model used for representing the dynamic response of the PV module at a specific operating point thus the meaning of R_s and R_0 is not exactly the same, nevertheless both refer to the ohmic losses and then exploitable for detecting degradation phenomena in the PV module.

A comparison by using all the experimental cases reported in Table 4.33 and Table 4.34 has been done by introducing a regression curve for describing the parameters (R_s) and (R_0) as function of the irradiance. Eq. (4.59) shows the general expression that best fits the experimental data. It is worth to note that the actual outdoor experimental campaign is referring to a short period (few weeks) that did not allow to cover a wide combination of different irradiance and temperature conditions. Indeed, the outdoor environmental conditions are strictly correlated during the days of the same season and only by considering long testing period it is possible to have an experimental campaign covering a large range of temperature (e.g. by considering summer and winter period). For this reason, the temperature variation encountered in the actual experimental tests has been considered having a negligible impact on the series resistance estimation and not accounted in the regression function as an additional predictor. Table 4.36 shows the parameter values of the regression curves describing the series resistance found by the static (SDM) and dynamic (CPE) models.

$$R = a + \left(\frac{b}{G}\right) \tag{4.59}$$

Table 4.36. Parameters of the regression curves for the series resistance values found using the SDM and the dynamic model (EIS).

Model	**Regression**	**Parameters**	
		a	b
Static Model (SDM)	Regression 1	-0.066	93.040
	Regression 2	0.147	80.374
Dynamic Model (EIS)	Regression 3	0.090	40.774
	Regression 4	0.266	44.975

Fig. 4.57 displays the resistance values of the models for every irradiance level. The

regression curves modelled using the SDM show two not–aligned tendencies that generate unbalanced approximations for the series resistance variations, especially at low irradiance. In contrast, the regression curves calculated with the dynamic CPE model show a more uniform difference throughout the whole irradiance range. It indicates a more stable and reliable approximation of the series resistance variation at all irradiance levels.

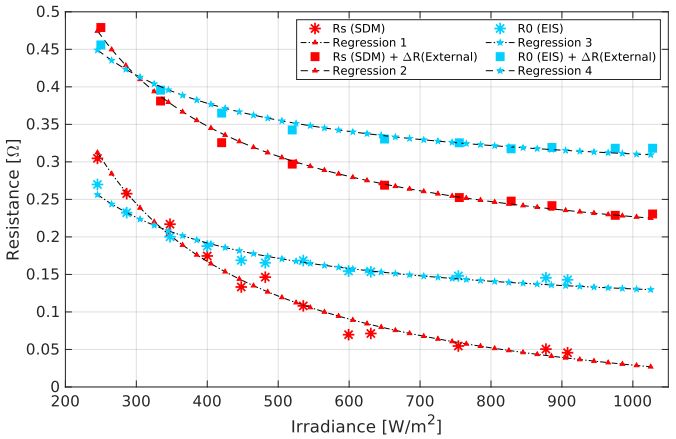

Figure 4.57. Regression process for the values calculated using the SDM and the dynamic model in the two test cases.

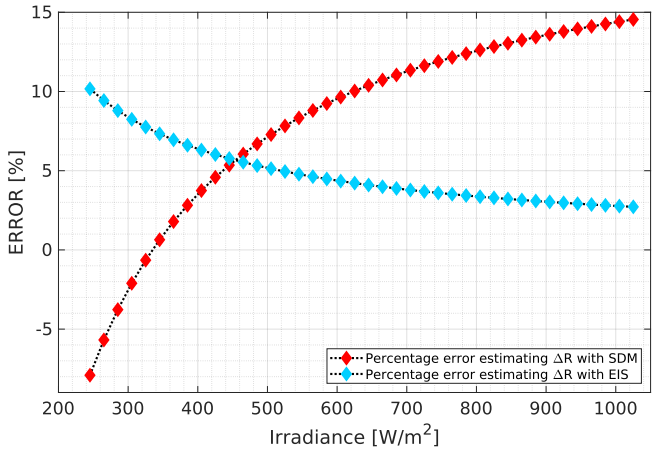

Figure 4.58. Percentage error estimation between the nominal delta value (ΔR = 0.175 Ω) and the value given by the SDM and the dynamic model using the regression curves for the whole irradiance range.

In fact, the error between the physical resistance value and each estimation (Fig. 4.58) shows that the dynamic (CPE) model approximates in a good way the

resistance variation (ΔR), even better than the static model (SDM), especially in the range from medium to high irradiance. The dynamic (CPE) model also shows a positive attribute since it displays an estimated error always positive (overestimation) and tends to stabilize from low to high irradiance levels. In contrast, the SDM depicts under and overestimations from low to high irradiance. This behavior reveals a technical weakness and supports the idea that the dynamic (CPE) model is most reliable for approximating the series resistance variations in all irradiance levels. As an additional test, the external resistance is changed to $\Delta R = 0.35\ \Omega$. Table 4.37 compares some similar irradiance values and corroborates the results previously discussed. Although the available data only covers from low to medium irradiance range, it again shows that the dynamic (CPE) model, calculated by using the EIS methodology, estimates the degradation of series resistance better than the SDM.

Table 4.37. Preliminary comparison of the series resistance variation found by the SDM and the CPE model($\Delta R = 0.35\ \Omega$).

Additional Resistance				**Nominal Case**				**Variation**	
G [W/m^2]	T [°C]	$R_s[\Omega]$	$R_0[\Omega]$	G [W/m^2]	T [°C]	$R_s[\Omega]$	$R_0[\Omega]$	$\Delta R_s[\Omega]$	$\Delta R_0[\Omega]$
297	29.2	0.481	0.541	286	23.4	0.258	0.232	0.223	0.309
361	27.2	0.446	0.529	347	25.2	0.217	0.200	0.229	0.329
414	27.5	0.435	0.537	400	25.6	0.175	0.188	0.260	0.349
479	29.6	0.425	0.516	482	28.7	0.146	0.166	0.279	0.350
542	31.4	0.402	0.504	535	30.7	0.108	0.168	0.294	0.336
596	34.3	0.402	0.496	599	33.6	0.070	0.154	0.332	0.342

4.5 Impedance spectroscopy for partial shading detection

4.5.1 Setup of series connected PV panels

The objective of this experimental campaign is to identify the relationship between the partial shading conditions occurring on the PV panels and the EIS spectra. For testing the EIS methodology on series-connected PV panels, the structure shown in figure 4.59 have been implemented. Only two PV panels are used in the PV string due to voltage limitations of the impedance spectroscopy equipment.

In order to emulate and keep under control the partial shading effect, a semi-transparent sheet with different shadow degrees is mounted over the PV structure as shown in figure 4.59b.

(a) Uniform irradiance condition

(b) Simulated partial shading condition

Figure 4.59. PV panel disposition.

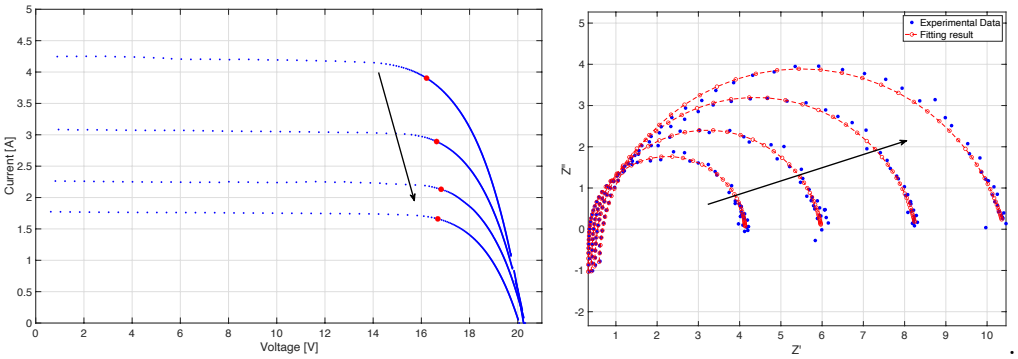

(a) I-V curves. In red the maximum power point.

(b) Impedance spectra measured in MPP

Figure 4.60. Static (a) and dynamic (b) response of two series connected PV panels under uniform environmental conditions.

Figure 4.60 shows the experimental I-V curves and the impedance spectra measured in each corresponding MPP (fig. 4.60b), with the two PV panels operating in outdoor uniform conditions.

The measurement system executes the procedure described in section 4.3 for acquiring periodically the I-V curve and the corresponding EIS spectra in MPP. For these tests, the amplitude of the signal perturbation for performing the EIS is

fixed at 100 mV, as for the test on the single PV panel. It corresponds, in average, to 0.7% of V_{mpp}.

As already discussed in the previous sections referring to the single panel analysis, the shape of the impedance spectra is well approximated by an semi-circle and can be modelled with a dynamic model with an unique constant phase element (CPE), representing the small-signal circuit shown in figure 1.6.

By comparing the trend of the I-V curves against the corresponding impedance spectra, the arc is enlarging as the irradiance is reducing. In red are reported the spectra reconstructed with the CPE model adjusted on the experimental data.

The measured impedance spectra does not show considerable noise, then the fitting procedure (adjusted as advises [70]) is used for calculating the parameters of the CPE dynamic model, which is now representing the whole PV string. The identified parameters are shown in table 4.38.

For each test, the table 4.38 reports the environmental conditions of the two panels (G_1, G_2; T_1,T_2) corresponding to the average values of the sensor measures acquired during the tests; the MPP operating point (V_{mpp},I_{mpp}) where the impedance analysis is performed; the CPE parameters values (L, R_0, R_1, Q,β, C_{eq}) with the corresponding interval of confidence given in percentage [%]. Finally, the mean square error (MSE) calculated with equation (4.60).

$$MSE = \frac{\sum_{k=1}^{N}[\Re(Z_{exp,k} - Z_{CPE,k})]^2 + [\Im(Z_{exp,k} - Z_{CPE,k}]^2}{N} \tag{4.60}$$

In almost all the cases, the difference between the irradiance and temperature values of the two PV panels is very small. Moreover, the interval of confidence and the MSE associated with each test is acceptable. Thus, all the proposed experimental tests, which have been performed in uniform conditions are considered valid.

Table 4.38. Estimated parameter of the CPE model for different environmental conditions.

Test	**Environmental Data**				**Operating point**		**CPE dynamic model parameters**											
#	$G1$ [W/m^2]	$G2$ [W/m^2]	$T1$[°C]	$T1$[°C]	V_{mpp}[V]	I_{mpp}[A]	L [μH]	± [%]	R_0[Ω]	± [%]	R_1[Ω]	± [%]	Q	± [%]	β	± [%]	C_{eq}[μF]	**MSE**
7	243.43	242.58	21.69	23.21	16.79	1.19	4.26	4.54	0.58	7.57	14.51	1.80	7.8E-05	9.40	0.78	1.36	11.70	**0.0383**
8	244.12	243.30	23.90	25.02	16.66	1.20	4.42	4.78	0.59	9.07	15.00	3.45	7.2E-05	13.76	0.79	1.97	11.60	**0.0468**
36	244.98	243.88	24.73	25.87	16.66	1.20	4.14	3.55	0.60	7.87	13.54	1.25	7.3E-05	9.66	0.80	1.30	12.30	**0.0330**
10	329.94	328.58	26.90	27.38	16.69	1.66	4.25	2.04	0.49	4.24	9.91	1.02	6.5E-05	7.37	0.85	0.89	18.10	0.0093
12	331.20	329.53	27.39	27.55	16.69	1.66	4.26	1.30	0.49	3.28	9.79	1.22	6.7E-05	6.27	0.85	0.76	18.30	0.0060
9	333.63	332.46	27.05	27.43	16.72	1.66	4.20	1.40	0.48	2.39	9.47	0.85	6.7E-05	7.05	0.85	0.86	19.10	0.0052
14	418.54	417.08	28.18	27.93	16.80	2.12	4.26	1.19	0.42	3.62	7.81	2.47	7.1E-05	10.02	0.88	1.12	25.00	0.0046
16	420.41	418.19	27.18	27.44	16.88	2.13	4.27	1.53	0.42	6.94	7.85	1.95	6.9E-05	10.44	0.88	1.23	23.60	0.0046
15	420.89	419.05	27.34	26.98	16.86	2.13	4.18	1.39	0.42	2.57	7.58	0.98	7.4E-05	7.96	0.87	0.96	24.20	0.0033
13	421.60	419.53	26.39	26.14	16.96	2.14	4.31	1.41	0.41	4.03	7.59	2.34	7.4E-05	10.07	0.87	1.17	24.30	0.0027
17	484.39	481.30	29.70	29.34	16.85	2.47	4.38	8.84	0.40	10.16	6.51	2.85	6.9E-05	21.14	0.90	2.62	29.00	**0.0249**
19	563.19	557.88	35.10	34.35	16.57	2.89	4.31	8.17	0.36	7.53	5.32	1.64	8.2E-05	18.43	0.91	2.44	37.30	0.0114
20	563.67	558.25	32.34	32.98	16.62	2.90	4.35	3.95	0.38	4.60	5.61	1.73	7.5E-05	12.32	0.91	1.51	34.30	0.0076
21	564.02	558.79	33.45	33.18	16.62	2.90	4.32	8.50	0.37	8.14	5.52	1.89	8.1E-05	22.50	0.91	3.03	36.30	0.0112
22	580.15	572.41	26.57	27.73	16.90	2.18	3.86	4.35	0.45	11.16	7.45	2.78	2.0E-04	18.94	0.77	2.67	27.60	**0.0262**
23	580.58	572.97	28.99	29.83	16.78	2.18	4.06	4.43	0.44	8.36	7.76	2.67	1.8E-04	15.31	0.77	2.31	25.90	**0.0256**
24	594.03	587.16	32.03	33.12	16.59	2.25	3.96	6.37	0.46	6.77	7.65	6.10	1.5E-04	18.03	0.80	2.49	28.50	**0.0224**
25	673.09	669.28	37.48	38.30	16.26	3.52	4.23	6.33	0.33	5.40	4.45	1.27	8.7E-05	15.88	0.94	1.90	50.10	0.0055
26	676.82	672.80	32.80	34.64	16.47	3.54	4.31	6.40	0.33	7.24	4.59	1.68	8.6E-05	14.23	0.93	1.86	49.00	0.0065
27	685.50	682.24	38.06	38.82	16.27	3.58	4.24	4.89	0.33	7.50	4.37	1.72	8.4E-05	14.51	0.94	1.88	51.60	0.0047
28	728.20	725.35	40.60	41.83	16.14	3.87	4.16	2.49	0.32	3.07	4.01	1.17	8.4E-05	7.60	0.96	0.93	57.60	0.0025
29	735.03	731.39	39.59	41.17	16.20	3.88	4.10	3.49	0.32	3.57	3.81	1.43	8.6E-05	11.03	0.96	1.35	58.90	0.0032
31	740.03	736.27	40.82	42.17	16.15	3.91	4.11	3.89	0.33	3.90	3.91	1.67	9.0E-05	10.13	0.95	1.24	57.20	0.0027
32	794.67	795.18	40.62	43.25	16.16	4.31	3.96	4.36	0.31	3.17	3.57	1.39	1.0E-04	10.31	0.94	1.27	62.20	0.0024
30	796.56	797.19	40.19	42.37	16.18	4.31	3.95	5.21	0.32	3.99	3.66	1.31	8.4E-05	14.28	0.96	1.75	58.80	0.0036
33	800.52	801.16	41.87	44.54	16.03	4.36	3.93	3.48	0.32	5.20	3.75	1.60	9.3E-05	11.50	0.95	1.40	61.30	0.0035
34	802.70	803.91	43.58	45.49	15.98	4.37	4.03	3.02	0.32	5.02	3.69	1.67	8.4E-05	10.89	0.96	1.23	59.70	0.0033
5	856.93	856.44	45.12	47.00	15.99	4.63	4.10	3.50	0.30	2.35	3.20	0.95	9.7E-05	9.67	0.96	1.17	66.40	0.0012
11	864.05	863.19	43.91	46.17	15.98	4.68	4.13	3.22	0.30	2.59	3.34	1.18	1.0E-04	9.34	0.95	1.11	67.20	0.0019

4.5.2 Series connected panels operating in partial shading conditions

The setup described in subsection 4.5.1 is also used for testing the dynamic behavior of the two series-connected PV panels operating under partial shading conditions. The latter are emulated as shown in figure 4.59b.

Figure 4.61 shows the corresponding experimental I-V curves and the EIS spectra for different irradiance levels. Depending on the angle of incidence of the sun, the degree of the shadow change during the experimental campaign in average a 30%. The exact shadowing factor can be easily obtained by the ratio of the two solar sensor values provided for each test.

Figure 4.61b illustrates that, using the same perturbation amplitude of the uniform case, the experimental EIS data showed high variability, especially for low irradiance conditions. As consequence, the reconstructed semi-arcs obtained using the CPE dynamic model are considered not representative at low irradiance tests. This is also justified by a significant increase of the MSE and the confidence intervals resulting from the CPE dynamic model parameters, as shown in table 4.39.

It is also worth noting that a large part of this research activity has been performed during the winter season thus has been difficult to do several experimental campaigns because it was necessary to have regular and stable environmental conditions. For this reason, although the experimental campaign is not completely useful, at least the tests performed at higher irradiance levels should be considered reliable, thus to have a first comparison with the uniform irradiated cases.

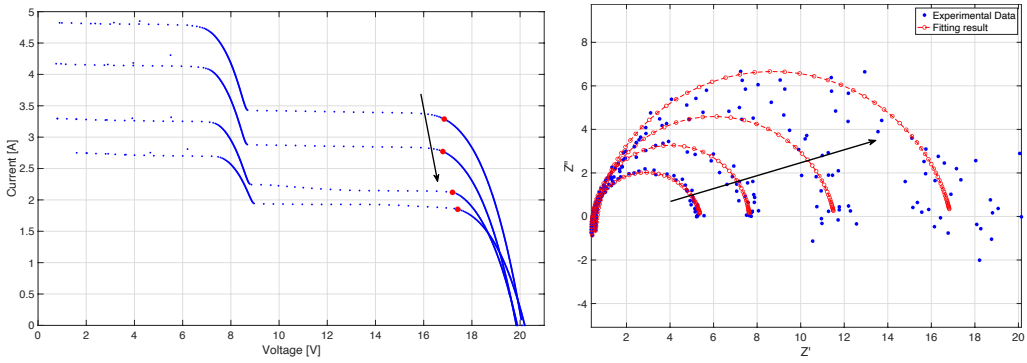

(a) I-V curves. In red the local maximum power point at the right side of the I-V curves. **(b)** Impedance spectra measured in MPP

Figure 4.61. Static (a) and dynamic (b) response of two series-connected PV panels under partial shading conditions.

Table 4.39. Estimated parameter of the CPE dynamic model in partial shading conditions.

Test	**Environmental Data**				**Operating point**		**CPE dynamic model parameters**										
#	$G1$ [W/m^2]	$G2$ [W/m^2]	$T1$[°C]	$T1$[°C]	V_{mpp}[V]	I_{mpp}[A]	L [μH]	± [%]	R_0[Ω]	± [%]	R_1[Ω]	± [%]	Q	± [%]	β	± [%]	C_{eq}[μF]	**MSE**
4	547.14	384.76	38.00	34.61	17.32	1.89	3.66	22.45	0.54	36.14	21.01	6.38	2.4E-05	55.08	0.90	6.50	9.60	**3.7548**
5	557.58	395.06	38.43	34.67	17.32	1.93	3.95	14.92	0.50	63.40	20.44	5.88	1.9E-05	62.56	0.90	7.38	8.20	**3.3174**
3	546.51	390.32	35.73	33.48	17.40	1.90	3.49	35.46	0.60	26.30	19.91	8.00	2.1E-05	68.10	0.91	8.15	9.70	**2.9122**
11	605.77	430.60	39.06	35.00	17.34	2.13	3.80	16.19	0.51	37.82	18.18	6.97	3.3E-05	46.43	0.89	5.87	13.20	**2.8261**
10	601.78	420.06	41.09	37.69	17.14	2.13	4.00	19.14	0.48	39.33	16.92	7.58	3.6E-05	62.76	0.87	7.89	12.10	**1.4494**
15	645.35	445.82	40.77	36.90	17.15	2.33	4.22	16.72	0.46	27.81	14.22	7.14	4.8E-05	59.53	0.88	7.51	17.70	**1.2931**
14	642.01	443.53	42.99	39.11	17.04	2.31	3.76	19.92	0.54	32.13	14.45	6.62	2.8E-05	59.07	0.90	7.24	11.80	**1.1301**
12	607.80	431.91	40.68	36.76	17.21	2.15	4.23	9.06	0.46	29.36	16.45	4.84	3.2E-05	37.96	0.87	4.43	10.40	**1.1035**
9	597.61	416.78	43.38	39.78	17.01	2.11	3.65	15.02	0.50	22.45	14.86	6.73	4.7E-05	42.39	0.86	5.55	14.60	**0.6381**
13	641.61	442.87	42.58	38.74	17.04	2.30	3.71	14.90	0.50	24.67	13.65	5.50	4.0E-05	48.86	0.88	6.17	14.50	**0.6024**
2	513.85	335.20	31.92	30.27	17.34	1.86	3.58	28.45	0.55	9.46	11.65	7.33	4.2E-05	38.00	0.93	4.54	22.30	**0.4121**
17	654.41	451.73	41.76	37.66	17.09	2.38	4.10	12.27	0.42	14.19	11.20	4.67	6.1E-05	32.21	0.89	3.99	23.70	**0.2514**
16	651.60	450.21	41.67	37.67	17.13	2.36	3.87	30.71	0.40	29.80	8.89	8.17	6.8E-05	61.01	0.89	7.96	26.00	**0.2120**
1	504.81	326.24	31.46	29.75	17.42	1.84	3.69	11.82	0.46	33.51	11.09	4.39	4.9E-05	35.78	0.88	4.06	18.20	**0.1855**
6	559.58	373.69	34.34	31.39	17.21	2.08	3.75	27.92	0.46	20.67	8.95	4.24	6.3E-05	41.04	0.88	5.82	23.10	**0.1349**
7	561.50	367.32	28.76	27.26	17.40	2.04	3.07	12.17	0.47	27.78	9.31	3.96	1.8E-04	29.12	0.72	4.58	14.30	**0.0998**
8	567.76	375.80	33.20	30.56	17.27	2.10	3.67	19.77	0.41	24.34	8.00	3.58	7.1E-05	29.87	0.88	3.94	26.40	**0.0736**
20	702.16	497.40	45.90	41.05	16.87	2.60	3.89	7.31	0.38	10.36	7.58	2.15	4.9E-05	18.21	0.96	2.06	34.70	**0.0594**
24	746.68	535.96	47.37	41.63	16.72	2.79	3.76	10.27	0.41	8.87	7.24	2.09	5.3E-05	22.15	0.94	2.68	32.00	**0.0393**
19	701.53	496.94	43.70	39.12	17.00	2.60	3.87	4.49	0.35	8.12	7.22	1.73	6.1E-05	14.41	0.94	1.62	37.80	**0.0373**
23	744.32	532.47	47.56	42.06	16.80	2.78	3.76	24.35	0.37	13.51	6.28	4.46	4.9E-05	33.45	0.97	4.06	38.90	**0.0338**
18	701.35	497.11	42.31	37.65	17.11	2.59	3.78	12.44	0.34	13.68	6.64	2.94	6.2E-05	25.74	0.95	3.23	39.50	**0.0330**
21	710.34	503.36	42.60	37.97	17.09	2.63	3.83	10.24	0.35	14.34	6.87	2.30	5.5E-05	19.25	0.95	2.14	36.80	**0.0279**
26	750.28	538.27	46.95	41.56	16.81	2.80	3.69	9.98	0.36	11.25	6.05	1.96	5.8E-05	23.77	0.96	2.83	40.70	**0.0244**
25	750.01	537.36	46.47	40.70	16.89	2.79	3.78	12.41	0.34	13.54	6.04	2.17	7.2E-05	29.19	0.94	3.54	41.60	**0.0240**
22	740.30	529.83	47.31	41.87	16.85	2.76	3.80	4.98	0.35	8.10	6.21	1.70	6.3E-05	14.78	0.95	1.73	41.90	0.0170
27	750.34	537.96	46.78	41.02	16.85	2.79	3.63	5.99	0.37	7.67	6.06	1.82	5.7E-05	18.08	0.96	1.97	41.40	0.0167
35	856.88	654.65	49.03	42.65	16.67	3.28	3.27	5.92	0.37	5.93	5.17	2.18	1.8E-04	16.21	0.84	2.15	44.50	0.0124
46	932.10	695.56	44.50	40.21	16.72	3.72	3.66	4.39	0.33	6.83	4.89	2.37	1.8E-04	15.21	0.84	2.14	50.20	0.0112
41	896.87	710.34	47.16	41.23	16.69	3.49	3.33	5.66	0.36	6.18	4.86	1.88	1.7E-04	17.23	0.85	2.32	44.90	0.0110
37	858.43	657.12	47.81	40.96	16.80	3.28	3.23	5.49	0.37	6.33	4.92	2.44	1.6E-04	16.77	0.85	2.20	42.90	0.0103
36	858.16	657.60	49.47	42.15	16.71	3.28	3.29	4.63	0.35	6.25	5.01	1.66	1.8E-04	14.66	0.84	1.98	46.90	0.0095
39	860.23	656.87	48.32	42.06	16.73	3.29	3.24	4.38	0.36	6.24	4.94	2.08	1.8E-04	18.81	0.84	2.36	46.20	0.0090
31	801.69	587.57	49.42	42.96	16.70	3.01	3.70	4.64	0.35	5.49	5.39	1.44	1.1E-04	13.06	0.89	1.67	43.50	0.0087
45	930.88	694.26	43.32	40.26	16.79	3.71	3.57	4.37	0.33	7.33	4.51	2.80	1.6E-04	15.94	0.86	2.10	49.10	0.0087
47	933.92	696.17	43.42	38.54	16.85	3.72	3.70	5.04	0.33	7.82	4.67	2.52	1.7E-04	19.16	0.85	2.59	47.30	0.0084
42	897.72	708.51	44.21	38.69	16.90	3.49	3.40	3.94	0.35	5.59	4.89	1.84	1.8E-04	15.29	0.83	2.01	43.10	0.0083
43	898.96	710.67	45.50	39.55	16.84	3.50	3.48	3.60	0.34	7.64	5.14	2.07	1.7E-04	14.71	0.83	2.15	42.30	0.0082
38	859.67	657.18	48.44	42.10	16.69	3.29	3.24	4.34	0.37	5.93	5.00	2.37	1.8E-04	16.08	0.84	2.08	44.70	0.0080
44	901.39	713.71	47.44	41.88	16.64	3.51	3.32	5.16	0.35	4.82	4.88	1.73	1.7E-04	11.82	0.84	1.65	45.20	0.0074
34	856.17	653.48	47.73	41.67	16.77	3.28	3.38	2.73	0.35	4.63	5.18	1.89	1.5E-04	12.47	0.85	1.70	45.40	0.0058

4.5.3 Uniform vs. partial shading condition operation

A graphical comparison of two I-V curves and the corresponding EIS spectra is shown in figure 4.62. The plots have been selected among the reliable tests and refer to an uniform operating condition and to a partial shading condition having similar MPP respectively. Specifically, the data of test #21 of table 4.38 and test #35 of table 4.39 have been used.

First of all, this comparison put into evidence how the knowledge of only the V_{mpp} and I_{mpp} values is not enough to distinguish if the PV system is operating in uniform or partial shading conditions (if the I-V scan is not performed and the irradiance values are not known). In these cases, the EIS spectra should provide additional information to distinguish the uniform from the partial shading operation..

When the two PV panels operate in uniform conditions, the dynamic behavior of each one is similar, thus it is expected that the whole string could be modeled as a single EIS semi-arc using a simple CPE dynamic model as already verified in the previous subsection. Differently, in partial shading conditions, the not shaded PV panel is working at a point not corresponding to its MPP. Figure 4.63 proves that it operates closer to its own open-circuit voltage. As discussed in section 4.3.3, the PV operating point has a strong impact on its internal junction capacitance and resistance, thus the two PV panels connected in series should exhibit a different dynamic behavior that should affect the impedance spectra of the PV string. Unfortunately, this difference is not visible in figure 4.62b where the CPE dynamic model gives a good fitting also for the partial shading condition.

Since this result is in contrast with the simulation analysis shown in subsection 4.2, a further experimental campaign has been conducted and discussed in the next section.

4.6 Double arc identification on the impedance spectra

4.6.1 Analysis of EIS experimental data with improved quality

A second campaign of measurements has been performed by adjusting some configuration parameters of the impedance spectroscopy instrumentation. In particular, the perturbation amplitude has been increased step by step until regular shapes was appearing for the EIS spectra. For the measures analysed in these sections, the perturbation amplitude has been fixed to 500 mV, it gives satisfactory results both in uniform and mismatched conditions. This amplitude corresponds, in average, to about 3% of PV operating voltage. In order to have

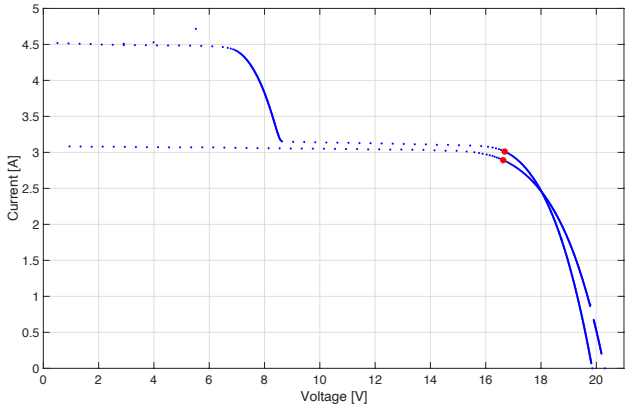

(a) I-V curves.

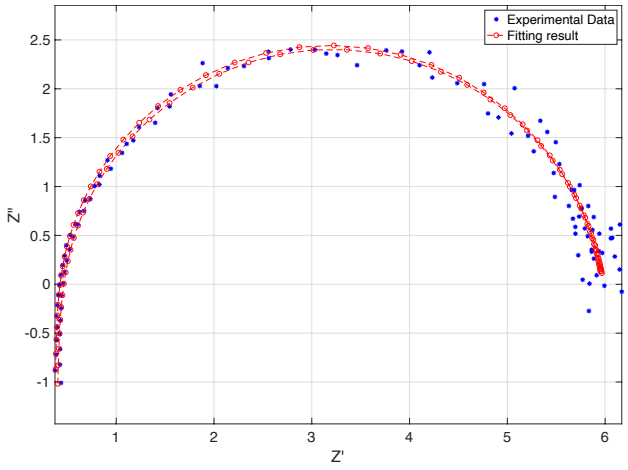

(b) Impedance spectra measured in MPP

Figure 4.62. Comparison of static a) and dynamic response b) of two series connected PV panels under uniform and partial shading conditions.

a comparison with the previous test, the same shadowing factor of 30% has been applied. Figure 4.64 shows the I-V curves and EIS plots acquired in uniform conditions. A small improvement is obtained with respect to the previous cases, since they were already satisfactory.

The most interesting results are appeared in partial shading conditions. Indeed, as shown in figure 4.65, the experimental impedance spectra now exhibit a double curvature at high frequency. This effect is usually due to the combination of two arcs, thus correctly representing the dynamic behavior of each one of the two panels operating in different environmental conditions. In these cases,the fitted curve obtained with a single CPE branch is not able to reconstruct this more complex EIS shape. In the figure only one case has been shown for a better

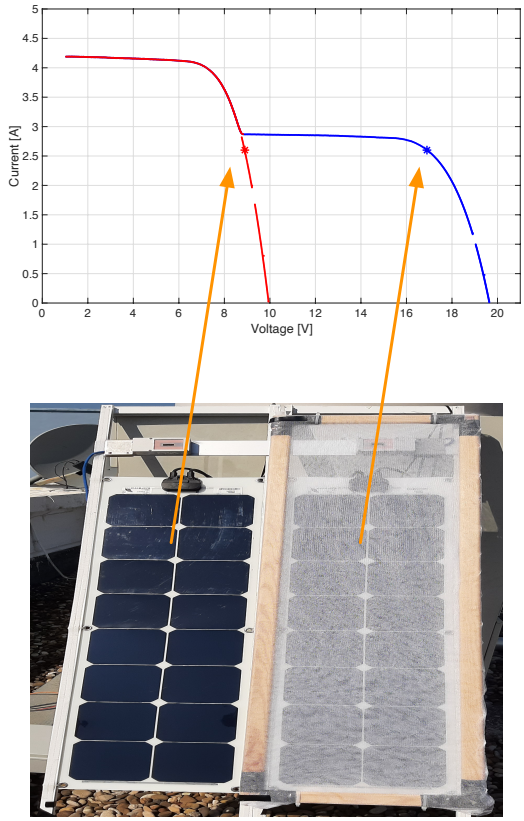

Figure 4.63. Different operating points for PV panels operating in partial shading conditions

visualization, but the EIS shape modification is evident in every test performed in partial shading condition.

4.6.2 PV dynamic models for PV string operating in partial shading conditions

As reported in literature the complex shapes of EIS spectra can be modelled in different way [70], [73], [80]. The three dynamic circuits shown in figure 4.66, which are potentially able to reproduce the double semi-arcs, will be analysed for verifying their capability to fit with the experimental measurements.

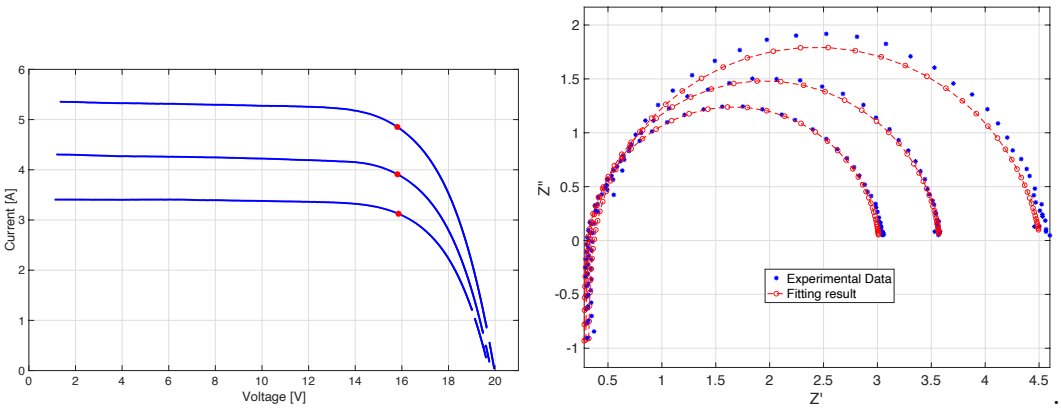

(a) I-V curves. In red the maximum power point. **(b)** Impedance spectra measured in MPP

Figure 4.64. Static (a) and dynamic (b) response of two series connected PV panels under uniform environmental conditions with optimised perturbation amplitude.

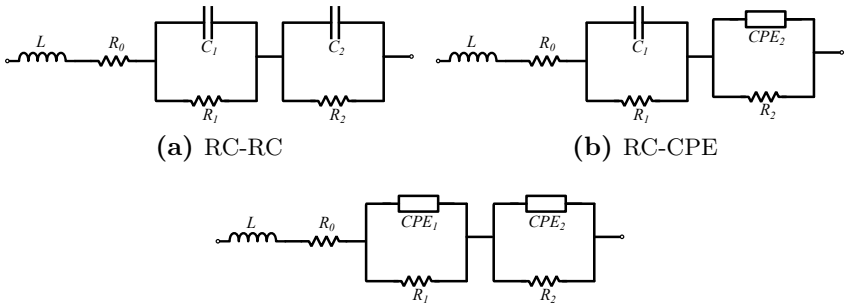

(a) RC-RC **(b)** RC-CPE

(c) CPE-CPE

Figure 4.66. PV dynamic models for representing PV string operating in partial shading condition.

The identified parameters are reported in table 4.40 for the model with two RC branches, in table 4.41 for the model with an RC branch and a CPE branch, in table 4.42 for the model with two CPE branches.
In each table the columns corresponding to the capacitive effects is highlighted to put into evidence the different dynamic behavior of the two panels connected in series.
Figure 4.67 shows the graphical comparison of the impedance spectra fitted with the three selected model. This example is referring to the same experimental impedance shown in figure 4.65b. As it is evident in the graphics, the first model, composed with two RC branches, does not perform accurately while the other two models exhibit similar results.

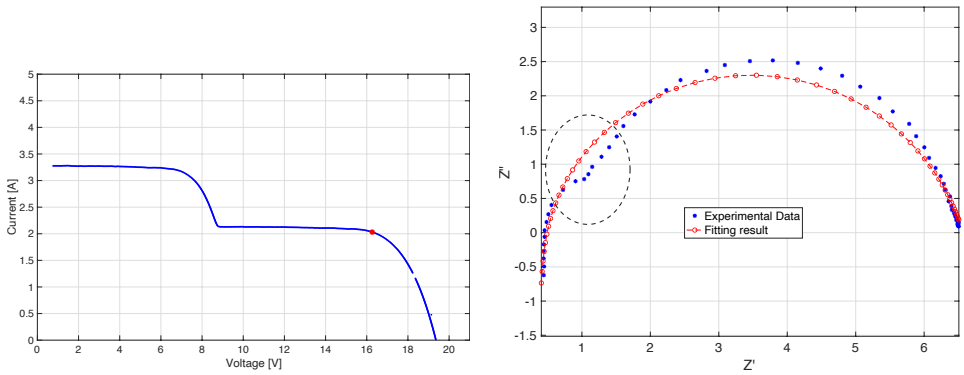

(a) I-V curves. In red the local maximum power point at the right side of the I-V curves.

(b) Impedance spectra measured in MPP

Figure 4.65. Static (a) and dynamic (b) response of two series connected PV panels under partial shading conditions with optimised perturbation amplitude.

Moreover, although the experimental impedance spectra are well fitted with the R-RC-CPE and R-CPE-CPE models, the parameters identification method does not give satisfactory results in terms of interval of confidence. This is in part justified by the fact that the procedure developed for the parameters identification in partial shading condition, is based on the deterministic approach implemented in the MATLAB identification toolbox and not yet optimised. As already did in section 3.8 for the static model, it is expected a significant improvements if a customised procedure is developed. Or investigating different approaches based on stochastic methods, as for example genetic algorithms, that might be much more effective for such kind of application. Indeed, in [157] and [42] has been already proven that optimised stochastic methods are suitable for the parameters identification of both static and dynamic models we are using for PV characterisation. Moreover stochastic methods can be implemented on embedded systems in more easy way since usually are characterised by low computational complexity, then more suitable for the on board applications.
Nevertheless, due to the limited number of tests currently available in partial shading conditions, a final assessment concerning the best model cannot be provided at this time. More complex models could be also analysed for achieving better results, if the proposed solutions are not satisfactory when an enriched experimental dataset will be available.

Table 4.40. Estimated parameter of a double RC branch

Test	Environmental Data				Operating point		L+R0 + R1//C1 parameters								additional R2//C2 branch				
#	$G1$ [W/m^2]	$G2$ [W/m^2]	$T1$[°C]	$T2$[°C]	V_{mpp}[V]	I_{mpp}[A]	L [μH]	± [%]	$R_0[\Omega]$	± [%]	$R_1[\Omega]$	± [%]	$C1[\mu$F]	± [%]	$R_2[\Omega]$	± [%]	$C2[\mu$F]	± [%]	MSE
1	619.96	389.79	46.14	44.96	16.49	1.99	3.57	5.29	0.41	37.38	4.10	53.67	**85.70**	48.13	1.93	40.93	**23.80**	11.25	0.0437
2	617.70	397.32	46.62	44.80	16.51	1.98	3.55	5.57	0.40	38.24	4.55	28.35	**72.30**	51.33	1.67	54.68	**27.80**	17.78	0.0600
3	775.06	532.75	46.36	46.08	16.61	2.67	4.02	9.18	0.22	45.60	3.83	8.90	**45.70**	29.07	0.39	30.60	**23.80**	60.30	0.0162
4	827.03	576.39	48.92	46.28	16.56	2.93	4.06	9.07	0.21	46.48	3.70	10.14	**50.80**	31.04	0.43	30.14	**23.80**	50.57	0.0197
5	910.00	650.49	47.61	47.44	16.59	3.35	4.33	8.53	0.19	57.55	3.15	6.46	**52.90**	17.71	0.32	26.94	**27.80**	82.33	0.0143
6	959.39	687.10	50.04	48.04	16.47	3.57	4.26	10.53	0.18	90.52	2.88	7.59	**55.30**	14.43	0.28	46.18	**27.80**	120.52	0.0139
7	968.00	706.04	48.91	48.17	16.48	3.65	4.24	7.67	0.20	48.09	3.10	5.24	**59.10**	17.46	0.27	31.32	**32.40**	77.94	0.0105
9	1043.15	768.71	52.49	51.25	16.31	3.88	4.11	9.48	0.19	69.96	2.78	6.18	**57.70**	13.65	0.25	43.24	**32.40**	114.43	0.0122
10	1053.80	769.92	50.05	50.02	16.50	3.85	4.15	11.29	0.19	98.65	2.65	6.05	**57.90**	11.41	0.22	72.16	**32.50**	170.74	0.0114
11	1066.96	777.00	49.55	48.34	16.51	3.86	3.82	11.13	0.20	91.92	2.82	6.16	**56.90**	19.60	0.23	75.37	**32.50**	139.24	0.0128

Table 4.41. Estimated parameter of the CPE model plus with an additional RC branch

Test	Environmental Data				Operating point		L+R0+CPE parameters										additional R2//C2 branch				
#	$G1$ [W/m^2]	$G2$ [W/m^2]	$T1$[°C]	$T2$[°C]	V_{mpp}[V]	I_{mpp}[A]	L [μH]	± [%]	$R_0[\Omega]$	± [%]	$R_1[\Omega]$	± [%]	Q1	± [%]	$\beta 1$	± [%]	$C1_{eq}[\mu$F]	$R_2[\Omega]$	± [%]	$C2[\mu$F]	± [%]	MSE
1	619.96	389.79	46.14	44.96	16.49	1.99	3.08	9.05	0.51	7.89	0.47	38.88	1.3E-06	139.05	1.34	10.81	**47.25**	5.20	6.74	**39.53**	15.38	0.0207
2	617.70	397.32	46.62	44.80	16.51	1.98	3.10	9.00	0.50	7.24	0.41	40.23	8.2E-07	125.84	1.39	9.39	**53.71**	5.61	6.61	**39.05**	15.94	0.0337
3	775.06	532.75	46.36	46.08	16.61	2.67	3.32	6.22	0.45	5.44	0.25	24.53	5.2E-07	53.85	1.46	3.91	**78.20**	3.89	6.54	**52.16**	8.30	0.0037
4	827.03	576.39	48.92	46.28	16.56	2.93	3.36	6.19	0.44	6.36	0.28	27.60	5.2E-07	72.45	1.46	4.87	**71.56**	3.75	6.72	**54.80**	10.81	0.0075
5	910.00	650.49	47.61	47.44	16.59	3.35	3.66	5.39	0.39	4.87	0.22	25.43	1.1E-06	75.02	1.42	5.74	**98.40**	3.19	5.26	**64.13**	7.81	0.0022
6	959.39	687.10	50.04	48.04	16.47	3.57	3.57	5.47	0.38	4.92	0.18	24.98	5.2E-07	46.66	1.51	3.53	**119.65**	2.92	7.20	**69.08**	8.86	0.0016
7	968.00	706.04	48.91	48.17	16.48	3.65	3.66	4.92	0.37	4.85	0.20	37.67	1.9E-06	100.53	1.39	8.24	**119.92**	3.11	3.66	**69.75**	10.96	0.0035
9	1043.15	768.71	52.49	51.25	16.31	3.88	3.50	5.18	0.37	4.55	0.19	29.22	9.7E-07	73.16	1.46	5.63	**124.79**	2.80	5.56	**72.10**	9.59	0.0016
10	1053.80	769.92	50.05	50.02	16.50	3.85	3.56	5.33	0.36	4.63	0.17	30.14	1.3E-06	82.92	1.45	6.41	**142.19**	2.65	5.74	**74.08**	8.30	0.0014
11	1066.96	777.00	49.55	48.34	16.51	3.86	3.24	5.60	0.36	4.87	0.19	27.95	1.1E-06	87.82	1.45	6.53	**124.15**	2.82	4.87	**71.13**	8.39	0.0026

Table 4.42. Estimated parameter of a double CPE model

Test	Environmental Data				Operating point		L+R0 + CPE parameters										additional CPE branch							
#	$G1$ [W/m^2]	$G2$ [W/m^2]	$T1$[°C]	$T2$[°C]	V_{mpp}[V]	I_{mpp}[A]	L [μH]	± [%]	$R_0[\Omega]$	± [%]	$R_1[\Omega]$	± [%]	Q1	± [%]	$\beta 1$	± [%]	$C1_{eq}[\mu$F]	$R_2[\Omega]$	± [%]	Q2	± [%]	$\beta 2$	± [%]	$C2_{eq}[\mu$F]	MSE
1	619.96	389.79	46.14	44.96	16.49	1.99	3.11	9.24	0.49	12.76	0.30	55.20	5.0E-07	97.09	1.46	7.76	**68.22**	5.46	9.01	6.0E-05	67.66	0.95	8.69	**37.33**	0.0188
2	617.70	397.32	46.62	44.80	16.51	1.98	3.15	8.81	0.48	12.11	0.28	50.99	3.8E-07	84.54	1.49	6.59	**74.14**	5.86	8.31	5.8E-05	62.05	0.95	7.75	**37.63**	0.0310
3	775.06	532.75	46.36	46.08	16.61	2.67	3.31	9.31	0.45	12.18	0.25	44.56	5.0E-07	53.74	1.47	4.18	**78.19**	3.87	7.69	5.0E-05	103.72	1.00	11.64	**51.87**	0.0041
4	827.03	576.39	48.92	46.28	16.56	2.93	3.33	9.39	0.44	13.49	0.28	44.71	4.6E-07	70.45	1.46	4.61	**69.96**	3.72	8.57	4.9E-05	120.41	1.01	13.19	**54.60**	0.0081
5	910.00	650.49	47.61	47.44	16.59	3.35	3.64	7.73	0.39	10.90	0.21	45.21	8.6E-07	70.77	1.45	5.94	**102.89**	3.19	6.93	6.4E-05	94.28	1.00	10.90	**63.37**	0.0025
6	959.39	687.10	50.04	48.04	16.47	3.57	3.53	8.85	0.39	10.24	0.18	33.13	4.6E-07	45.40	1.52	3.52	**119.04**	2.90	7.06	6.2E-05	82.83	1.01	9.03	**68.41**	0.0021
7	968.00	706.04	48.91	48.17	16.48	3.65	3.68	4.86	0.36	7.83	0.12	44.03	7.5E-07	67.89	1.51	5.87	**184.01**	3.24	4.81	1.0E-04	46.62	0.95	5.87	**66.97**	0.0029
9	1043.15	768.71	52.49	51.25	16.31	3.88	3.50	7.52	0.37	11.59	0.18	50.72	8.8E-07	70.69	1.47	6.11	**128.93**	2.80	7.44	7.3E-05	100.69	1.00	11.62	**71.61**	0.0018
10	1053.80	769.92	50.05	50.02	16.50	3.85	3.56	6.67	0.35	8.90	0.14	45.48	7.3E-07	67.40	1.52	5.75	**176.26**	2.69	6.83	8.4E-05	55.20	0.98	6.84	**71.52**	0.0014
11	1066.96	777.00	49.55	48.34	16.51	3.86	3.23	6.89	0.36	9.02	0.16	45.02	7.5E-07	77.39	1.49	6.32	**140.03**	2.85	7.44	7.7E-05	63.61	0.99	7.74	**69.63**	0.0027

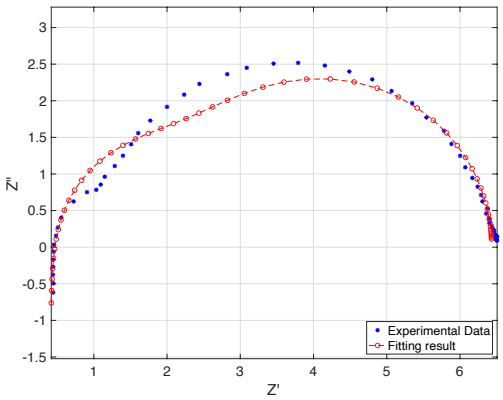

(a) Dynamic model with two RC branch

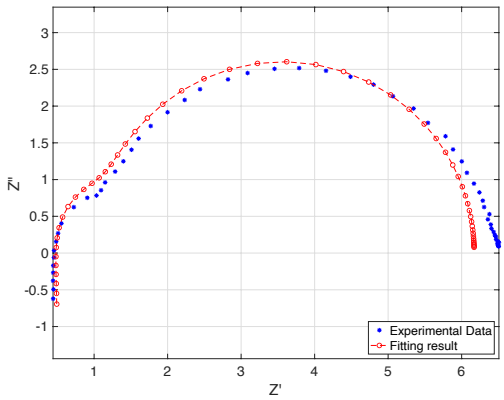

(b) Dynamic model with a RC branch and a CPE branch

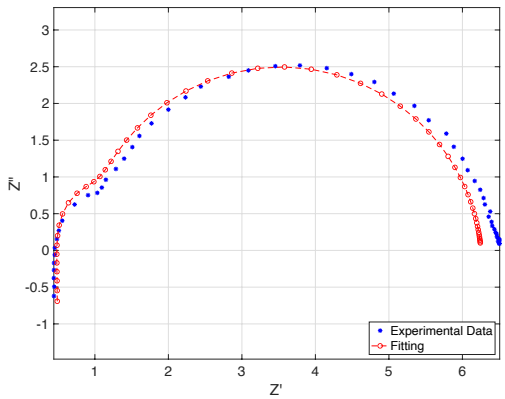

(c) Dynamic model with two CPE branch

Figure 4.67. Fitted impedance spectra with models of fig.4.66 for two series connected PV panels under partial shading conditions.

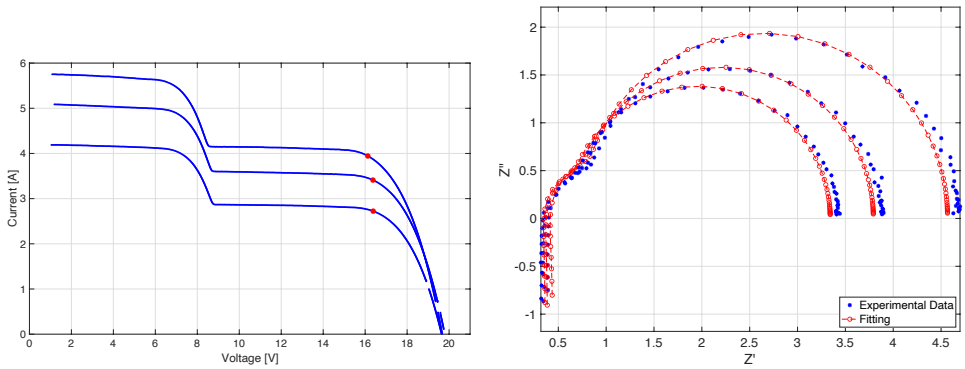

(a) I-V curves. In red the local maximum power point at the right side of the I-V curves.

(b) Impedance spectra measured in MPP

Figure 4.68. Static (a) and dynamic (b) response of two series connected PV panels under partial shading conditions with optimised perturbation amplitude.

4.6.3 Detection of small partial shading effect

Unfortunately few experimental cases are available with different environmental and shadowing conditions. As already mentioned, since the measurement equipment has been delivered by the manufacturer with a strong delay due to the pandemic emergency, it has been possible to start with the outdoor experiments during the winter season when many measurements have been not considered reliable due to the wrong setup, as the cases discussed in section 4.5.2, or for unstable environmental conditions.
Nevertheless the plots shown in figure 4.69 are very encouraging since they put into evidence how, with the proposed approach is possible to identify the presence of very small partial shading condition with a good reconstruction of the double arc.

4.6.4 EIS measurement vs. simulation data

In this section a comparison among experimental EIS and simulated EIS is provided. The LTspice model discussed in section 4.2.2 has been adapted to reproduce the static and dynamic behaviour of the two panels operating under the environmental conditions reported in the test #1 of table 4.42. The simulations have been performed with the schemes shown in figure 4.40 and 4.42 scaled to two panels. The SDM parameters of each panel have been identified by using the fitting procedure introduced in section 2.2.5. As concerns the p-n junction capacitive effects, the values $C1_{eq}$ and $C2_{eq}$ of test #1 in table 4.42 are used. The corresponding inductive and series resistive effects are also included. The

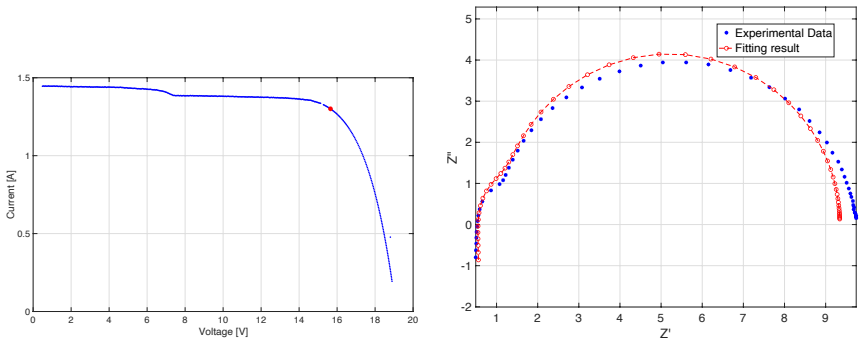

(a) I-V curve

(b) Impedance spectra measured in MPP

Figure 4.69. Static (a) and dynamic (b) response of two series connected PV panels under partial shading conditions with optimised perturbation amplitude.

p-n junction resistive effects that are accounted as differential resistances (R_1 and R_2) in the PV dynamic model, are self included in the LTspice circuit since they correspond to the non-linear effect of PV cell diodes when operate around their own polarisation point. The parameters of a commercial by-pass diode are also included in the LT spice model.

Figure 4.70a shows a very good agreement among experimental and simulated data. On the contrary the EIS spectra, shown in figure 4.70b, are not in perfect agreement, this is mainly due to the fact that LTspice circuit is not configured to reproduce the non linear effects of the two constant phase element associated to the PV panels. Indeed in the same figure are also reported the EIS impedance spectra of the double CPE model and double RC model fitted with the experimental data. It is well evident that the CPE-based model is converging to the experimental data while the RC-based model is almost perfectly fitted with the simulation data, thus confirming the previous assertion. This analysis opens the space for future improvement of LTspice model for a better modelling of PV dynamic behaviour.

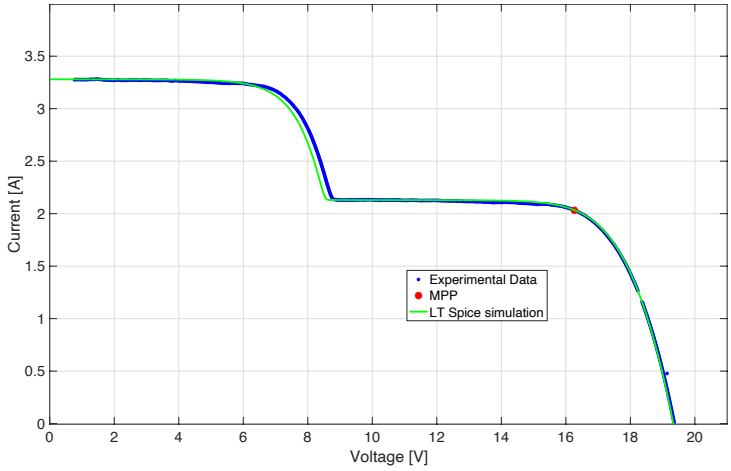

(a) I-V curves

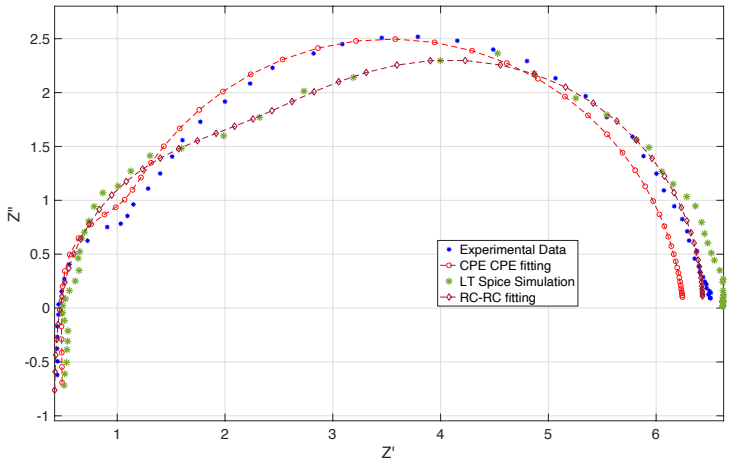

(b) Impedance spectra measured in MPP

Figure 4.70. Comparison of experimental vs. simulation data of two partial shaded PV panels.

4.7 Conclusion

In this chapter, the EIS methodology and the dynamic model of the SDM have been useful for analysing the behaviour of a PV panel under different conditions. The obtained outcomes have illustrated the high potential EIS methodology has for real–time monitoring conditions. The EIS based diagnostic method can be fruitfully employed in PV systems working at MPP in outdoor conditions without altering the standard operation of the system. Therefore, it avoids power losses and undesirable changing in the PV system operation. The dynamic model built with the impedance measurements provided better approximations than the classic static model (SDM) for a specific degradation process such as series resistance variations.

It has been also demonstrated and validated the feasibility of mismatching analysis using the EIS methodology for finding the wrong functionalities inside the PV panels. It will allow taking care of the PV panel health for improving their functionalities and the performance of the whole PV installation or plant, e.g by improving the tracking capability of MPPT algorithms to reach the global maximum.

Finally it is important to remark that this work is the first attempt to apply the EIS methodology for detecting the PV degradation phenomena in real–operative outdoor conditions. The validation of experimental results demonstrated the potentiality of the proposed approach to detect other PV degradation phenomena as well as by-pass diode failure, potential induced degradation and hot–spot that usually happen in PV sources operating in outdoor conditions.

General Conclusions

This thesis proposed advances in models and methods for the early detection of degradation effects on PV devices. The research activity has been mainly focused on approaches suitable for online implementation with the additional benefit of avoiding changing the nominal operative condition of the PV devices.

The analysis performed in this work took advantage of two properties of the static model (SDM). Firstly, the good representation of the PV characteristics in healthy conditions. Secondly, the effect that degradation processes have on the set of parameters that compound it. These attributes have been exploited by using particular developed methods that additionally complement the SDM attributes with the dynamic model features of PV devices.

- As concerns the analytical approach, the most significant results achieved in this thesis work is the experimental validation and comparison of some methods that, although have been well-validated in the literature for estimating the SDM parameters in healthy conditions, could fail into detecting the SDM parameters when the PV panels operate in degraded conditions. Indeed, since these methods are based on some assumptions/simplifications that could be valid only in healthy conditions, it has been proven that among the selected methods, only few of them are able to identify correctly the SDM parameters in presence of degradation phenomena. In particular to estimate the variations of the internal series and shunt resistances.

- In the second part of the thesis is proposed a method for detecting the SDM parameters through the combination of numerical algorithms and ANN. In this approach the ability of the ANN of modelling the strong non-linear relationships among the SDM parameters, the I-V characteristics and the environmental conditions is used. The numerical algorithm is employed during the training phase for providing the target values to the ANN. A comparison of the ANN performance with respect to other regression model approaches has been also provided for confirming the best result of ANN for this kind of applications.

The main novelties of the proposed method are in the information used for the diagnosis. Firstly it does not need of experimental degraded I-V curves for the training phase. This aspect is very important since the degraded I-V curves are usually not available because of the difficulty of reproducing the large variety of degraded conditions and the long time the measurement process will take. Secondly during the online operation it only needs to measure few points of the I-V curve close the MPP and the environmental information for determining the degradation effect. Thus the proposed approach can run on board without affecting the normal operation of the PV system.

- Finally, in the third part of the thesis work, is developed an innovative method for PV diagnosis based on the analysis in the frequency-domain by exploiting the Impedance Spectroscopy technique. The implementation of this methodology combined with modelling using PV dynamic models allowed the detection of degradation effects in PV panels such as the increment in the series resistance and effects of partial shading conditions. The experimental results proven that the proposed method outperform the other approaches, which are generally based on the static model, in the estimation of some parameters variation, e.g. series resistance. The innovation around this approach lies in the fact that it can be applied to commercial PV panels under real-operating outdoor conditions. In fact, previous literature shows few works that analyzed the characteristics of PV cells and some on PV panels in the frequency domain, but they were applied at the laboratory level in controlled environmental conditions.

In conclusion, we can affirm that the main relevance of this thesis lies in providing to the researchers and operators working in the PV field, valuable analytical and experimental information related to methods for the identification of PV degradation. Indeed, it has been demonstrated that some well-known approaches, used for analyzing the PV panel in healthy conditions, are not so effective for studying degraded PV panels.

Table 4.43 summarizes the three methodologies presented in this thesis having into account two elements, the complexity of performing the methodology and the information needed for applying each analysis. The applicability of each methodology depends on the resources and information available for implementing the solution. For instance, although the analytical methods require a set of information from different sources, it has a low complexity for their implementation. On the other hand, the implementation using Impedance Spectroscopy only requires to assure that the PV device is working on MPP, situation that assures the correct functionality of the system for power production. Thus, this methodology has a great advantage over the other two (requiring less

Table 4.43. Summary of the methodologies proposed

	Analytical Methods	**ANN based model**	**Impedance Spectroscopy**
Complexity	*Low*: Based on a set of explicit equations and approximations	*Medium*: The training phase could demand medium computational resources. After this stage, it requires less computational effort.	*High*: Require specialized hardware for an on-field application (under development)
Required information	Isc, Voc, Vmpp, Impp. Datasheet parameters. Environmental information (G,T)	3 points (V,I) around MPP. Environmental information (G,T)	MPP. **NO** environmental information.

information), but, at this moment, it needs specialized equipment for performing the analysis. This type of equipment currently is under development.

It is important to highlight that the proposed approach of operating in the frequency domain for PV degradation analysis opens a new perspective for PV system manufacturers interested in developing online-diagnostic functionality employing embedded systems.

Future Works

The promising results of the methodology working on the frequency domain have taken the attention for increasing the efforts of improving it for the next steps. The development proposed and addressed for enhancing the methodology goes around two aspects. The extension of the analysis to other degradation effects and the onboard implementation. In the first line, this methodology showed great potential for detecting degradation effects such as increments in the ohmic resistance and partial shading conditions. But, it could be extended to other types of effects as hot spots or potential induced degradation (PID).

Finally, the onboard implementation activity is necessary for integrating the analysis with the equipment that allows the implementation of the technique in the field.

Both activities will be also carried out in the frame of the "A Holistic Monitoring and Diagnostic Tool for Photovoltaic Generators" (HOTSPHOT) PRIN 2020 National Project.

REFERENCES

[1] J.-W. Arnulf, "Pv status report 2019," Publications Office of the European Union, 2019. [Online]. Available: https://publications.jrc.ec.europa.eu/repository/bitstream/JRC118058/kjna29938enn_1.pdf

[2] S. A. Aleem, S. M. S. Hussain, and T. S. Ustun, "A review of strategies to increase pv penetration level in smart grids," Energies, vol. 13, no. 3, 2020. [Online]. Available: https://www.mdpi.com/1996-1073/13/3/636

[3] H. Dag and M. Buker, "Performance evaluation and degradation assessment of crystalline silicon based photovoltaic rooftop technologies under outdoor conditions," Renewable Energy, vol. 156, pp. 1292 – 1300, 2020. [Online]. Available: http://www.sciencedirect.com/science/article/pii/S096014811931835X

[4] E. L. Meyer and E. E. van Dyk, "Assessing the reliability and degradation of photovoltaic module performance parameters," IEEE Transactions on Reliability, vol. 53, no. 1, pp. 83–92, 03 2004.

[5] V. Poulek, J. Šafránková, L. Černá, M. Libra, V. Beránek, T. Finsterle, and P. Hrzina, "Pv panel and pv inverter damages caused by combination of edge delamination, water penetration, and high string voltage in moderate climate," IEEE Journal of Photovoltaics, vol. 11, no. 2, pp. 561–565, 2021.

[6] P. Sánchez-Friera, M. Piliougine, J. Peláez, J. Carretero, and M. Sidrach de Cardona, "Analysis of degradation mechanisms of crystalline silicon PV modules after 12 years of operation in Southern Europe," Progress in Photovoltaics: Research and Applications, vol. 19, no. 6, pp. 658–666, 2011.

[7] M. Piliougine, A. Oukaja, P. Sánchez-Friera, G. Petrone, F. J. Sánchez-Pacheco, G. Spagnuolo, and M. S. de Cardona, "Analysis of the degradation of single-crystalline silicon modules after 21years of operation," Progress in Photovoltaics, 2021.

[8] M. Kumar and A. Kumar, "Performance assessment and degradation analysis of solar photovoltaic technologies: A review," Renewable and

Sustainable Energy Reviews, vol. 78, pp. 554–587, 2017. [Online]. Available: https://www.sciencedirect.com/science/article/pii/S1364032117305919

[9] "Pv residential," https://solar.huawei.com/apac/FusionSolarResidential, accessed: 2022-05-23.

[10] S. R. Madeti and S. Singh, "Monitoring system for photovoltaic plants: A review," Renewable and Sustainable Energy Reviews, vol. 67, pp. 1180 – 1207, 2017. [Online]. Available: http://www.sciencedirect.com/science/article/pii/S1364032116305792

[11] F. D. Lia, S. Castello, and L. Abenante, "Efficiency degradation of c-silicon photovoltaic modules after 22-year continuous field exposure," in 3rd World Conference onPhotovoltaic Energy Conversion, 2003. Proceedings of, vol. 2, 2003, pp. 2105–2108 Vol.2, ISBN: 4-9901816-0-3.

[12] J. A. Kratochvil, W. E. Boyson, and D. L. King, "Photovoltaic array performance model." Albuquerque (NM, USA), Tech. Rep., 2004, SAND2004-3535.

[13] A. Kimber, T. Dierauf, L. Mitchell, C. Whitaker, T. Townsend, J. NewMiller, D. King, J. Granata, K. Emery, C. Osterwald, D. Myers, B. Marion, A. Pligavko, A. Panchula, T. Levitsky, J. Forbess, and F. Talmud, "Improved test method to verify the power rating of a photovoltaic (PV) project," in 34th IEEE Photovoltaic Specialists Conference (PVSC), June 2009, pp. 000 316–000 321.

[14] A. Cuevas and R. A. Sinton, Characterisation and diagnosis of silicon wafers and devices. Oxford (UK): Elsevier Science, 2005, ch. IIb-4, pp. 163 – 188, ISBN: 978-1-85617-457-2.

[15] M. Piliougine, C. C. nete, R. Moreno, J. Carretero, J. Hirose, S. Ogawa, and M. S. de Cardona, "Comparative analysis of energy produced by photovoltaic modules with anti-soiling coated surface in arid climates," Applied Energy, vol. 112, pp. 626 – 634, 2013.

[16] A. Phinikarides, N. Kindyni, G. Makrides, and G. E. Georghiou, "Review of photovoltaic degradation rate methodologies," Renewable and Sustainable Energy Reviews, vol. 40, pp. 143 – 152, 2014.

[17] D. L. King, W. Boyson, B. Hansen, and W. Bower, "Improved accuracy for low-cost solar irradiance sensors," in 2nd World Conference and Exhibition on Photovoltaic Solar Energy Conversion, 1998, pp. 1–5.

[18] A. Kumar, S. Gomathinayagam, G. Giridhar, I. Mitra, R. Vashistha, R. Meyer, M. Schwandt, and K. Chhatbar, "Field experiences with the operation of solar radiation resource assessment stations in India," Energy Procedia, vol. 49, pp. 2351 – 2361, 2014.

[19] J. Mölken, U. Yusufoglu, A. Safiei, H. Windgassen, R. Khandelwal, T. Pletzer, and H. Kurz, "Impact of micro-cracks on the degradation of solar cell performance based on two-diode model parameters," Energy Procedia, vol. 27, p. 167–172, 12 2012.

[20] J. Weicht, F. Hamelmann, and G. Behrens, "Parameter variation of the one-diode model of a-Si and a- Si/μc-Si solar cells for modeling light-induced degradation," Journal of Physics: Conference Series, vol. 559, p. 012017, 11 2014.

[21] E. L. Meyer, "Extraction of saturation current and ideality factor from measuring v_{oc} and i_{sc} of photovoltaic modules," International Journal of Photoenergy, vol. 2017, p. 9, 2017.

[22] N. Femia, G. Petrone, G. Spagnuolo, and M. Vitelli, Power Electronics and Control Techniques for Maximum Energy Harvesting in Photovoltaic Systems. CRC Press, 2013, ISBN: 978-1-4665-0690-9.

[23] M. C. Di Piazza, M. Luna, and G. Vitale, "Dynamic pv model parameter identification by least-squares regression," IEEE Journal of Photovoltaics, vol. 3, no. 2, pp. 799–806, 2013. [Online]. Available: https://doi.org/10.1109/JPHOTOV.2012.2236146

[24] J. D. Bastidas-Rodriguez, G. Petrone, C. A. Ramos-Paja, and G. Spagnuolo, "Photovoltaic modules diagnostic: An overview," in IECON 2013 - 39th Annual Conference of the IEEE Industrial Electronics Society, November 2013, pp. 96–101.

[25] NIST, "2018 CODATA recommended values of the fundamental constants of physics and chemistry SP 959. national institute of standard and technology. u.s. department of commerce," June 2019. [Online]. Available: https://physics.nist.gov/cuu/pdf/wallet_2018.pdf

[26] E. I. Batzelis and S. A. Papathanassiou, "A Method for the Analytical Extraction of the Single-Diode PV Model Parameters," IEEE Transactions on Sustainable Energy, vol. 7, no. 2, pp. 504–512, 2016.

[27] G. Ciulla, V. Lo Brano, V. Di Dio, and G. Cipriani, "A comparison of different one-diode models for the representation of I-V characteristic of a PV cell," Renewable and Sustainable Energy Reviews, vol. 32, pp. 684–696, 2014. [Online]. Available: http://dx.doi.org/10.1016/j.rser.2014.01.027

[28] B. Yang, J. Wang, X. Zhang, T. Yu, W. Yao, H. Shu, and F. Zeng, "Comprehensive overview of meta-heuristic algorithm applications on PV cell parameter identification," Energy Conversion and Management, vol. 208, no. January, p. 112595, 2020. [Online]. Available: https://doi.org/10.1016/j.enconman.2020.112595

[29] M. Oulcaid, H. E. Fadil], L. Ammeh, A. Yahya, and F. Giri, "Parameter extraction of photovoltaic cell and module: Analysis and discussion of various combinations and test cases," Sustainable Energy Technologies and Assessments, vol. 40, p. 100736, 2020. [Online]. Available: http://www.sciencedirect.com/science/article/pii/S2213138819308896

[30] N. Aoun and N. Bailek, "Evaluation of mathematical methods to characterize the electrical parameters of photovoltaic modules," Energy Conversion and Management, vol. 193, pp. 25 – 38, 2019.

[31] K. Ishaque, Z. Salam, S. Mekhilef, and A. Shamsudin, "Parameter extraction of solar photovoltaic modules using penalty-based differential evolution," Applied Energy, vol. 99, pp. 297 – 308, 2012.

[32] F. J. Toledo and J. M. Blanes, "Analytical and quasi-explicit four arbitrary point method for extraction of solar cell single-diode model parameters," Renewable Energy, vol. 92, pp. 346–356, 2016.

[33] D. Kler, Y. Goswami, K. Rana, and V. Kumar, "A novel approach to parameter estimation of photovoltaic systems using hybridized optimizer," Energy Conversion and Management, vol. 187, pp. 486 – 511, 2019.

[34] U. Eicker, "Chapter 5 – Grid–connected photovoltaic systems," in Solar Technologies for Buildings. John Wiley & Sons, Ltd, 2003, ch. 5, pp. 201–242. [Online]. Available: http://dx.doi.org/10.1002/0470868341.ch5

[35] E. Saloux, A. Teyssedou, and M. Sorin, "Explicit model of photovoltaic panels to determine voltages and currents at the maximum power point," Solar Energy, vol. 85, no. 5, pp. 713 – 722, 2011.

[36] J. Cubas, S. Pindado, and C. De Manuel, "Explicit expressions for solar panel equivalent circuit parameters based on analytical formulation and the Lambert W-Function," Energies, vol. 7, no. 7, pp. 4098–4115, 2014.

[37] D. Sera and R. Teodorescu, "Robust series resistance estimation for diagnostics of photovoltaic modules," in 2009 35th Annual Conference of IEEE Industrial Electronics, Nov 2009, pp. 800–805.

[38] F. Ghani, G. Rosengarten, M. Duke, and J. Carson, "The numerical calculation of single-diode solar-cell modelling parameters," Renewable Energy, vol. 72, pp. 105 – 112, 2014.

[39] E. van Dyk and E. Meyer, "Analysis of the effect of parasitic resistances on the performance of photovoltaic modules," Renewable Energy, vol. 29, no. 3, pp. 333 – 344, 2004.

[40] V. J. Chin, Z. Salam, and K. Ishaque, "Cell modelling and model parameters estimation techniques for photovoltaic simulator application: A review," Applied Energy, vol. 154, pp. 500 – 519, 2015. [Online]. Available: http://www.sciencedirect.com/science/article/pii/S0306261915006455

[41] G. Petrone, C. A. Ramos-Paja, and G. Spagnuolo, Photovoltaic Sources Modeling. Chichester, West Sussex, United Kingdom: John Wiley & Sons, 2017, ISBN: 978-1-118-75612-6.

[42] G. Petrone, M. L. Id, G. L. Tona, M. Carmela, D. Piazza, and G. S. Id, "Online Identification of Photovoltaic Source Parameters by Using a Genetic Algorithm," Applied Sciences, no. 9, pp. 1–16, 2018.

[43] E. Batzelis, "Non-iterative methods for the extraction of the single-diode model parameters of photovoltaic modules: A review and comparative assessment," Energies, vol. 12, no. 3, p. 358, 2019.

[44] A. R. Jordehi, "Parameter estimation of solar photovoltaic (PV) cells: A review," Renewable and Sustainable Energy Reviews, vol. 61, pp. 354–371, 2016. [Online]. Available: http://dx.doi.org/10.1016/j.rser.2016.03.049

[45] P. A. Kumari and P. Geethanjali, "Parameter estimation for photovoltaic system under normal and partial shading conditions: A survey," Renewable and Sustainable Energy Reviews, vol. 84, no. December 2017, pp. 1–11, 2018. [Online]. Available: https://doi.org/10.1016/j.rser.2017.10.051

[46] M. Köntges, S. Kurtz, C. Packard, U. Jahn, K. Berger, K. Kato, T. Friesen, H. Liu, M. V. Iseghem, J. Wohlgemuth, D. Miller, M. Kempe, P. Hacke, F. Reil, N. Bogdanski, W. Herrmann, C. Buerhop-Lutz, G. Razongles, and G. Friesen, "Review of failures of photovoltaic modules," 2014. [Online]. Available: https://iea-pvps.org/wp-content/uploads/2020/01/IEA-PVPS_T13-01_2014_Review_of_Failures_of_Photovoltaic_Modules_Final.pdf

[47] D. Sera, R. Teodorescu, and P. Rodriguez, "Photovoltaic module diagnostics by series resistance monitoring and temperature and rated power estimation," in 34th IEEE Conference on Industrial Electronics, 2008. [Online]. Available: https://doi.org/10.1109/IECON.2008.4758297

[48] J. S. Stein, S. McCaslin, C. W. Hansen, W. E. Boyson, and C. D. Robinson, "Measuring PV system series resistance without full IV curves," in 40th IEEE Photovoltaic Specialist Conference (PVSC), 2014, pp. 2032–2036. [Online]. Available: https://doi.org/10.1109/PVSC.2014.6925326

[49] M. G. Deceglie, T. J. Silverman, B. Marion, and S. R. Kurtz, "Real-time series resistance monitoring in PV systems without the need for i–v curves," IEEE J Photovolt, vol. 5, pp. 1706–1709, 2015. [Online]. Available: https://doi.org/10.1109/jphotov.2015.2478070

[50] G. Spagnuolo, K. Lappalainen, S. Valkealahti, and P. Manganiello, "Identification and diagnosis of a photovoltaic module based on outdoor measurements," in IEEE Milan PowerTech, 2019, pp. 1–6. [Online]. Available: https://doi.org/10.1109/PTC.2019.8810767

[51] G. Alves dos Reis Benatto, C. Mantel, S. Spataru, A. A. Santamaria Lancia, N. Riedel, S. Thorsteinsson, P. B. Poulsen, H. Parikh, S. Forchhammer, and D. Sera, "Drone-based daylight electroluminescence imaging of pv modules," IEEE Journal of Photovoltaics, vol. 10, no. 3, pp. 872–877, 2020.

[52] A. Catalano, V. d'Alessandro, P. Guerriero, and S. Daliento, "Diagnosis of power losses in pv plants by means of uav thermography," in 2019 International Conference on Clean Electrical Power (ICCEP), 2019, pp. 306–310.

[53] A. Mellit, G. Tina, and S. Kalogirou, "Fault detection and diagnosis methods for photovoltaic systems: A review," Renewable and Sustainable Energy Reviews, vol. 91, pp. 1–17, 2018. [Online]. Available: https://www.sciencedirect.com/science/article/pii/S1364032118301370

[54] A. Mellit and S. Kalogirou, "Artificial intelligence and internet of things to improve efficacy of diagnosis and remote sensing of solar photovoltaic systems: Challenges, recommendations and future directions," Renewable and Sustainable Energy Reviews, vol. 143, p. 110889, 2021. [Online]. Available: https://www.sciencedirect.com/science/article/pii/S1364032121001830

[55] W. Chine, A. Mellit, V. Lughi, A. Malek, G. Sulligoi, and A. Massi Pavan, "A novel fault diagnosis technique for photovoltaic systems based on artificial neural networks," Renewable Energy, vol. 90, pp. 501–512, 2016. [Online]. Available: https://www.sciencedirect.com/science/article/pii/S0960148116300362

[56] Z. Chen, L. Wu, S. Cheng, P. Lin, Y. Wu, and W. Lin, "Intelligent fault diagnosis of photovoltaic arrays based on optimized

kernel extreme learning machine and i-v characteristics," Applied Energy, vol. 204, pp. 912–931, 2017. [Online]. Available: https://www.sciencedirect.com/science/article/pii/S0306261917305214

[57] M. Hussain, M. Dhimish, S. Titarenko, and P. Mather, "Artificial neural network based photovoltaic fault detection algorithm integrating two bi-directional input parameters," Renewable Energy, vol. 155, pp. 1272–1292, 2020. [Online]. Available: https://doi.org/10.1016/j.renene.2020.04.023

[58] H. Zhu, L. Lu, J. Yao, S. Dai, and Y. Hu, "Fault diagnosis approach for photovoltaic arrays based on unsupervised sample clustering and probabilistic neural network model," Solar Energy, vol. 176, pp. 395–405, 2018. [Online]. Available: https://www.sciencedirect.com/science/article/pii/S0038092X18310338

[59] S. Tchoketch Kebir, N. Cheggaga, A. Ilinca, and S. Boulouma, "An efficient neural network-based method for diagnosing faults of pv array," Sustainability, vol. 13, no. 11, 2021. [Online]. Available: https://www.mdpi.com/2071-1050/13/11/6194

[60] L. Erhan, M. Ndubuaku, M. Di Mauro, W. Song, M. Chen, G. Fortino, O. Bagdasar, and A. Liotta, "Smart anomaly detection in sensor systems: A multi-perspective review," Information Fusion, vol. 67, pp. 64–79, 2021. [Online]. Available: https://www.sciencedirect.com/science/article/pii/S1566253520303717

[61] "Smart pv optimizer," https://solar.huawei.com/na/Products, accessed: 2021-04-02.

[62] M. Ma, Z. Zhang, P. Yun, Z. Xie, H. Wang, and W. Ma, "Photovoltaic module current mismatch fault diagnosis based on i-v data," IEEE Journal of Photovoltaics, pp. 1–10, 2021.

[63] K. A. Kim, G.-S. Seo, B.-H. Cho, and P. T. Krein, "Photovoltaic hot-spot detection for solar panel substrings using AC parameter characterization," IEEE T Power Electr, vol. 31, no. 2, pp. 1121–1130, 2016. [Online]. Available: https://doi.org/10.1109/TPEL.2015.2417548

[64] K. A. Kim, C. Xu, L. Jin, and P. T. Krein, "A dynamic photovoltaic model incorporating capacitive and reverse-bias characteristics," IEEE J Photovolt, vol. 3, no. 4, pp. 1334–1341, 2013. [Online]. Available: https://doi.org/10.1109/JPHOTOV.2013.2276483

[65] J. Johnson, D. Schoenwald, S. Kuszmaul, J. Strauch, and W. Bower, "Creating dynamic equivalent PV circuit models with impedance spectroscopy for arc fault modeling," in 37th IEEE Photovoltaic Specialists Conference (PVSC), 2011, pp. 002 328–002 333. [Online]. Available: https://doi.org/10.1109/PVSC.2011.6186419

[66] O. I. Olayiwola and P. S. Barendse, "Photovoltaic cell/module equivalent electric circuit modeling using impedance spectroscopy," IEEE T Ind Appl, vol. 56, pp. 1690–1701, 2020. [Online]. Available: https://doi.org/10.1109/tia.2019.2958906

[67] T. Yeow, J. Sun, Z. Yao, J.-N. Jaubert, and K. P. Musselman, "Evaluation of impedance spectroscopy as a tool to characterize degradation mechanisms in silicon photovoltaics," Sol Energy, vol. 184, pp. 52–58, May 2019. [Online]. Available: https://doi.org/10.1016/j.solener.2019.03.088

[68] N. Katayama, S. Osawa, S. Matsumoto, T. Nakano, and M. Sugiyama, "Degradation and fault diagnosis of photovoltaic cells using impedance spectroscopy," Sol Energ Mat Sol C, vol. 194, pp. 130–136, 2019. [Online]. Available: https://doi.org/10.1016/j.solmat.2019.01.040

[69] Elizabeth Von Hauff, "Impedance Spectroscopy for Emerging Photovoltaics," J Phys Chem C, vol. 123, no. 18, pp. 11 329–11 346, 2019. [Online]. Available: https://doi.org/10.1021/acs.jpcc.9b00892

[70] A. Lasia, Electrochemical impedance spectroscopy and its applications, 3rd ed. Springer, 2014, ISBN: 978-1-4614-8932-0.

[71] S. M. Abdulrahim, Z. Ahmad, J. Bahadra, and N. J. Al-Thani, "Electrochemical impedance spectroscopy analysis of hole transporting material free mesoporous and planar perovskite solar cells," Nanomaterials, vol. 10, 2020. [Online]. Available: https://doi.org/10.3390/nano10091635

[72] A. Bouzidi, W. Jilani, I. Yahia, and H. Zahran, "Impedance spectroscopy of monocrystalline silicon solar cells for photosensor applications: Highly sensitive device," Physica B, vol. 596, p. 412375, 2020. [Online]. Available: https://doi.org/10.1016/j.physb.2020.412375

[73] L. Shelembe and P. Barendse, "Online condition monitoring of photovoltaic (PV) cells by implementing electrical impedance spectroscopy using a switch-mode DC-DC converter," in IEEE Energy Conversion Congress and Exposition (ECCE), 2020. [Online]. Available: https://doi.org/10.1109/ecce44975.2020.9235596

[74] A. Sacco, "Electrochemical impedance spectroscopy: Fundamentals and application in dye-sensitized solar cells," Renew Sust Energ Rev, vol. 79, pp. 814–829, 2017. [Online]. Available: https://doi.org/10.1016/j.rser.2017.05.159

[75] E. Barsoukov and J. R. Macdonald, Impedance Spectroscopy: Theory, Experiment, and Applications, 3rd ed. John Wiley & Sons, Inc., 2018, ISBN: 978-1-119-33317-3.

[76] G. Nusev, D. juričić, M. Gaberšček, J. moškon, and P. Boškoski, "Fast impedance measurement of li-ion battery using discrete random binary excitation and wavelet transform," IEEE Access, vol. 9, pp. 46 152–46 165, 2021.

[77] P. Boškoski, Fast electrochemical impedance spectroscopy. Springer, 2017, ISBN: 978-3-319-53389-6.

[78] M. I. Oprea, S. V. Spataru, D. Sera, P. B. Poulsen, S. Thorsteinsson, R. Basu, A. R. Andersen, and K. H. Frederiksen, "Detection of potential induced degradation in c-Si PV panels using electrical impedance spectroscopy," in 43rd IEEE Photovoltaic Specialists Conference (PVSC), 2016, pp. 1575–1579. [Online]. Available: https://doi.org/10.1109/PVSC.2016.7749885

[79] S. Kumar, P. Singh, and G. Chilana, "Study of silicon solar cell at different intensities of illumination and wavelengths using impedance spectroscopy," Sol Energ Mat Sol C, vol. 93, no. 10, pp. 1881–1884, 2009. [Online]. Available: https://doi.org/10.1016/j.solmat.2009.07.002

[80] J. Panigrahi, Vandana, R. Singh, N. Batra, J. Gope, M. Sharma, P. Pathi, S. Srivastava, C. Rauthan, and P. Singh, "Impedance spectroscopy of crystalline silicon solar cell: Observation of negative capacitance," Sol Energy, vol. 136, pp. 412–420, 2016. [Online]. Available: https://doi.org/10.1016/j.solener.2016.06.041

[81] M. U. Saleh, J. LaCombe, N. K. T. Jayakumar, S. Kingston, J. Harley, C. Furse, and M. Scarpulla, "Signal propagation through piecewise transmission lines for interpretation of reflectometry in photovoltaic systems," IEEE J Photovolt, vol. 9, no. 2, pp. 506–512, 2019. [Online]. Available: https://doi.org/10.1109/JPHOTOV.2018.2884011

[82] I. Matacena, L. Lancellotti, N. Lisi, P. Delli Veneri, P. Guerriero, and S. Daliento, "Impedance spectroscopy for the characterization of the all-carbon graphene-based solar cell," Energies, vol. 13, no. 8, 2020. [Online]. Available: https://doi.org/10.3390/en13081908

[83] M. A. Varnosfaderani and D. Strickland, "Online electrochemical impedance spectroscopy (EIS) estimation of a solar panel," Vacuum, vol. 139, pp. 185–195, 2017. [Online]. Available: https://doi.org/10.1016/j.vacuum.2017.01.011

[84] D. Chenvidhya, K. Kirtikara, and C. Jivacate, "A new characterization method for solar cell dynamic impedance," Sol Energ Mat Sol C, vol. 80, no. 4, pp. 459–464, 2003. [Online]. Available: https://doi.org/10.1016/j.solmat.2003.06.011

[85] J. E. Garland, D. J. Crain, J. P. Zheng, C. M. Sulyma, and D. Roy, "Electro-analytical characterization of photovoltaic cells by combining voltammetry and impedance spectroscopy: voltage dependent parameters of a silicon solar cell under controlled illumination and temperature," Energy Environ Sci, vol. 4, pp. 485–498, 2011. [Online]. Available: https://doi.org/10.1039/C0EE00307G

[86] P. Yadav, K. Pandey, B. Tripathi, and M. Kumar, "Investigation of interface limited charge extraction and recombination in polycrystalline silicon solar cell: Using DC and AC characterization techniques," Sol Energy, vol. 116, pp. 293–302, 2015. [Online]. Available: https://doi.org/10.1016/j.solener.2015.04.011

[87] O. I. Olayiwola and P. S. Barendse, "Characterization of silicon-based photovoltaic cells using broadband impedance spectroscopy," IEEE T Ind Appl, vol. 54, no. 6, pp. 6309–6319, 2018. [Online]. Available: https://doi.org/10.1109/TIA.2018.2850025

[88] M. U. Saleh, C. Deline, E. J. Benoit, S. R. Kingston, J. B. Harley, C. M. Furse, and M. A. Scarpulla, "Detection and localization of damaged photovoltaic cells and modules using spread spectrum time domain reflectometry," IEEE J Photovolt, vol. 11, no. 1, pp. 195–201, 2021. [Online]. Available: https://doi.org/10.1109/JPHOTOV.2020.3030185

[89] L. Liu, W. Liu, X. Zhang, and J. Ingenhoff, "Research on the novel explicit model for photovoltaic i-v characteristic of the single diode model under different splitting spectrum," Results in Physics, vol. 12, pp. 662 – 672, 2019.

[90] J. C. H. Phang, D. S. H. Chan, and J. R. Phillips, "Accurate analytical method for the extraction of solar cell model parameters," Electronics Letters, vol. 20, no. 10, pp. 406–408, 1984.

[91] L. Cristaldi, M. Faifer, M. Rossi, and S. Toscani, "A simplified model of photovoltaic panel," in 2012 IEEE International Instrumentation and Measurement Technology Conference Proceedings, May 2012, pp. 431–436.

[92] D. Sera, L. Mathe, T. Kerekes, R. Teodorescu, and P. Rodriguez, "A low-disturbance diagnostic function integrated in the PV arrays'MPPT algorithm," in IECON 2011 - 37th Annual Conference of the IEEE Industrial Electronics Society, Nov 2011, pp. 2456–2460.

[93] F. J. Toledo, J. M. Blanes, A. Garrigós, and J. A. Martínez, "Analytical resolution of the electrical four-parameters model of a photovoltaic module using small perturbation around the operating point," Renewable Energy, vol. 43, pp. 83 – 89, 2012.

[94] F. J. Toledo and J. M. Blanes, "Geometric properties of the single-diode photovoltaic model and a new very simple method for parameters extraction," Renewable Energy, vol. 72, pp. 125–133, 2014.

[95] S. Cannizzaro, M. Di Piazza, M. Luna, and G. Vitale, "Generalized classification of PV modules by simplified single-diode models," in Industrial Electronics (ISIE), 2014 IEEE 23rd International Symposium on, June 2014, pp. 2266–2273.

[96] S. Cannizzaro, M. C. Di Piazza, M. Luna, and G. Vitale, "PVID: An interactive Matlab application for parameter identification of complete and simplified single-diode PV models," in 2014 IEEE 15th Workshop on Control and Modeling for Power Electronics (COMPEL), June 2014, pp. 1–7.

[97] A. Senturk and R. Eke, "A new method to simulate photovoltaic performance of crystalline silicon photovoltaic modules based on datasheet values," Renewable Energy, vol. 103, pp. 58 – 69, 2017.

[98] R. M. Corless, G. H. Gonnet, D. E. G. Hare, D. J. Jeffrey, and D. E. Knuth, "On the lambertw function," Advances in Computational Mathematics, vol. 5, no. 1, pp. 329–359, 12 1996.

[99] C. A. Ramos-Paja, G. Petrone, and G. Spagnuolo, "Symbolic algebra for the calculation of the series and parallel resistances in PV module model," in International Conference on Clean Electrical Power Renewable Energy Resources Impact (ICCEP), Alghero, Sardinia, Italy, 11-13 June 2013, pp. 62–66, ISBN: 978-1-4673-4430-2.

[100] F. Lasnier and T. G. Ang, Photovoltaic Engineering Handbook. IOP Publishing, 1990, ISBN: 0-85274-311-4.

[101] A. R. Conn, N. I. M. Gould, and P. L. Toint, Trust-Region Methods. SIAM Society for Industrial and Applied Mathematics, 2000, ISBN: 0-89871-460-5.

[102] T. Khatib and W. Elmenreich, Modeling of photovoltaic systems using Matlab. Hoboken, New Jersey (USA): John Wiley & Sons, 2016, ISBN: 978-1-119-11810-7.

[103] B. R. Zaharatos, M. Campanelli, and L. Tenorio, "On the estimability of the PV single-diode model parameters," Statistical Analysis and Data Mining: The ASA Data Science Journal, vol. 8, no. 5-6, pp. 329–339, 2015.

[104] MathWorks, "Matlab optimization toolbox. user's guide. r2019b," Natick, Massachusetts (USA), techreport, 2019. [Online]. Available: www.mathworks.com/help/pdf_doc/optim/optim_tb.pdf

[105] K. Emery, "Photovoltaic calibrations at the National Renewable Energy Laboratory and uncertainty analysis following the ISO 17025 guidelines," Golden (CO, USA), Tech. Rep., 2016, NREL/TP-5J00-66873. [Online]. Available: https://www.nrel.gov/docs/fy17osti/66873.pdf

[106] E. Koutroulis and F. Blaabjerg, "A new technique for tracking the global maximum power point of pv arrays operating under partial-shading conditions," IEEE Journal of Photovoltaics, vol. 2, no. 2, pp. 184–190, 2012.

[107] I. Shams, S. Mekhilef, and K. S. Tey, "Maximum power point tracking using modified butterfly optimization algorithm for partial shading, uniform shading, and fast varying load conditions," IEEE Transactions on Power Electronics, vol. 36, no. 5, pp. 5569–5581, 2021.

[108] R. Ahmad, A. F. Murtaza, and H. A. Sher, "Power tracking techniques for efficient operation of photovoltaic array in solar applications – a review," Renewable and Sustainable Energy Reviews, vol. 101, pp. 82–102, 2019.

[109] M. Piliougine, J. Carretero, L. Mora-López, and M. Sidrach de Cardona, "Experimental system for current–voltage curve measurement of photovoltaic modules under outdoor conditions," Progress in Photovoltaics: Research and Applications, vol. 19, no. 5, pp. 591–602, 2011.

[110] M. Piliougine, J. Carretero, L. Mora-López, and M. Sidrach de Cardona, "New software tool to characterize photovoltaic modules from commercial equipment," WEENTECH Proceedings in Energy, pp. 211 – 220. , 2018.

[111] S. Kaplanis and E. Kaplani, "Energy performance and degradation over 20 years performance of BP c–Si PV modules," Simulation Modelling Practice and Theory, vol. 19, no. 4, pp. 1201 – 1211, 2011. [Online]. Available: http://www.sciencedirect.com/science/article/pii/S1569190X10001711

[112] Z. Salam, K. Ishaque, and H. Taheri, "An improved two-diode photovoltaic (PV) model for PV system," in 2010 Joint International Conference on Power Electronics, Drives and Energy Systems 2010 Power, India, December 2010, pp. 1–5.

[113] K. G. Calkins, "Applied Statistics - Lesson 5 - Correlation Coefficients." July 2005, Last visited: 14/07/2020. [Online]. Available: www.andrews.edu/~calkins/math/edrm611/edrm05.htm

[114] M. B. Rhouma, A. Gastli, L. Ben Brahim, F. Touati, and M. Benammar, "A simple method for extracting the parameters of the pv cell single-diode model," Renewable Energy, vol. 113, pp. 885 – 894, 2017. [Online]. Available: http://www.sciencedirect.com/science/article/pii/S0960148117305694

[115] M. Piliougine, D. Elizondo, L. Mora-López, and M. Sidrach de Cardona, "Modelling photovoltaic modules with neural networks using angle of incidence and clearness index," Progress in Photovoltaics: Research and Applications, vol. 23, no. 4, pp. 513–523, 2015.

[116] B. Cortés, R. Tapia Sánchez, and J. J. Flores, "Characterization of a polycrystalline photovoltaic cell using artificial neural networks," Solar Energy, vol. 196, no. November 2019, pp. 157–167, 2020. [Online]. Available: https://doi.org/10.1016/j.solener.2019.12.012

[117] M. Mittal, B. Bora, S. Saxena, and A. M. Gaur, "Performance prediction of pv module using electrical equivalent model and artificial neural network," Solar Energy, vol. 176, pp. 104–117, 2018.

[118] W. Hayder, A. Abid, and M. Ben Hamed, "Modeling of a photovoltaic cell based on recurrent neural networks," in 2017 International Conference on Green Energy Conversion Systems (GECS), March 2017, pp. 1–5.

[119] F. Salem and M. A. Awadallah, "Parameters estimation of photovoltaic modules: comparison of ANN and ANFIS," International Journal of Industrial Electronics and Drives, vol. 1, no. 2, p. 121, 2014.

[120] E. Karatepe, M. Boztepe, and M. Colak, "Neural network based solar cell model," Energy Conversion and Management, vol. 47, no. 9-10, pp. 1159–1178, 2006.

[121] K. Jolson Singh, K. L. R. Kho, S. Jitu Singh, Y. Chandrika Devi, N. Singh, and S. Sarkar, "Artificial Neural Network Approach for More Accurate Solar Cell Electrical Circuit Model," International Journal on Computational Science & Applications, vol. 4, no. 3, pp. 101–116, 2014.

[122] PV Simulation under Homogeneous Conditions. John Wiley & Sons, Ltd, 2017, ch. 3, pp. 45–80. [Online]. Available: https://onlinelibrary.wiley.com/doi/abs/10.1002/9781118755877.ch3

[123] Y. Li, K. Ding, J. Zhang, F. Chen, X. Chen, and J. Wu, "A fault diagnosis method for photovoltaic arrays based on fault parameters identification," Renewable Energy, vol. 143, pp. 52–63, 2019. [Online]. Available: https://www.sciencedirect.com/science/article/pii/S0960148119306317

[124] W. Marion, A. Anderberg, C. Deline, S. Glick, M. Muller, G. Perrin, J. Rodriguez, S. Rummel, K. Terwilliger, and T. Silverma, "User's manual for data for validating models for pv module performance (nrel/tp-5200-61610)," United States of America,: The National Renewable Energy Laboratory (NREL), 2014.

[125] Y. Chaibi, A. Allouhi, M. Malvoni, M. Salhi, and R. Saadani, "Solar irradiance and temperature influence on the photovoltaic cell equivalent-circuit models," Solar Energy, vol. 188, no. July, pp. 1102–1110, 2019. [Online]. Available: https://doi.org/10.1016/j.solener.2019.07.005

[126] Z. Chen, Y. Chen, L. Wu, S. Cheng, and P. Lin, "Deep residual network based fault detection and diagnosis of photovoltaic arrays using current-voltage curves and ambient conditions," Energy Conversion and Management, vol. 198, p. 111793, 2019.

[127] "Exporting matlab neural network in open neural network exchange," https://www.mathworks.com/help/deeplearning/deep-learning-import-export-and-customization.html, accessed: 2021-04-02.

[128] "Exporting matlab functions via the matlab compiler sdk," https://www.mathworks.com/products/matlab-compiler-sdk.html, accessed: 2021-04-02.

[129] "Stm32 solutions for artificial neural networks," https://www.st.com/content/st_com/en/ecosystems/stm32-ann.html#stm32-sann-stepnncontainer, accessed: 2021-04-02.

[130] A. Mellit, S. Sağlam, and S. Kalogirou, "Artificial neural network-based model for estimating the produced power of a photovoltaic module," Renewable Energy, vol. 60, pp. 71 – 78, 2013. [Online]. Available: http://www.sciencedirect.com/science/article/pii/S0960148113002279

[131] M. Hudson Beale, M. T. Hagan, and H. B.Demuth, "Deep learning toolbox," Tech. Rep., 2019.

[132] O. Hachana, K. E. Hemsas, G. M. Tina, and C. Ventura, "Comparison of different metaheuristic algorithms for parameter identification of photovoltaic cell/module," Journal of renewable and sustainable energy, vol. 5, no. 5, p. 053122, 2013. [Online]. Available: https://doi.org/10.1063/1.4822054

[133] R. Abbassi, A. Abbassi, M. Jemli, and S. Chebbi, "Identification of unknown parameters of solar cell models: A comprehensive overview of available approaches," Renewable and Sustainable Energy Reviews, vol. 90, pp. 453–474, 2018. [Online]. Available: https://doi.org/10.1016/j.rser.2018.03.011

[134] P. J. Gnetchejo, S. Ndjakomo Essiane, P. Ele, R. Wamkeue, D. Mbadjoun Wapet, and S. Perabi Ngoffe, "Important notes on parameter estimation of solar photovoltaic cell," Energy Conversion and Management, vol. 197, no. May, p. 111870, 2019. [Online]. Available: https://doi.org/10.1016/j.enconman.2019.111870

[135] K. Lappalainen, P. Manganiello, M. Piliougine, G. Spagnuolo, and S. Valkealahti, "Virtual sensing of photovoltaic module operating parameters," IEEE Journal of Photovoltaics, vol. 10, no. 3, pp. 852–862, 2020. [Online]. Available: https://doi.org/10.1109/JPHOTOV.2020.2972688

[136] M. Piliougine and G. Spagnuolo, "Mismatching and partial shading identification in photovoltaic arrays by an artificial neural network ensemble," Solar Energy, vol. 236, pp. 712–723, 2022. [Online]. Available: https://doi.org/10.1016/j.solener.2022.03.026

[137] M. Aghaei, A. Fairbrother, A. Gok, S. Ahmad, S. Kazim, K. Lobato, G. Oreski, A. Reinders, J. Schmitz, M. Theelen, P. Yilmaz, and J. Kettle, "Review of degradation and failure phenomena in photovoltaic modules," Renew Sust Energ Rev, vol. 159, p. 112160, 2022. [Online]. Available: https://doi.org/10.1016/j.rser.2022.112160

[138] Y. C. Hsieh, L. R. Yu, T. C. Chang, W. C. Liu, T. H. Wu, and C. S. Moo, "Parameter identification of one-diode dynamic equivalent circuit model for photovoltaic panel," IEEE J Photovolt, vol. 10, no. 1, pp. 219–225, 2020. [Online]. Available: https://doi.org/10.1109/JPHOTOV.2019.2951920

[139] T. S. Ustun, Y. Nakamura, J. Hashimoto, and K. Otani, "Performance analysis of PV panels based on different technologies after two years of outdoor exposure in fukushima, japan," Renew Energ, vol. 136, pp. 159–178, 2019. [Online]. Available: https://doi.org/10.1016/j.renene.2018.12.100

[140] M. Zaimi, H. El Achouby, O. Zegoudi, A. Ibral, and E. Assaid, "Numerical method and new analytical models for determining temporal changes of model-parameters to predict maximum power and efficiency of pv module operating outdoor under arbitrary conditions," Energ Convers Manage, vol. 220, p. 113071, 2020. [Online]. Available: https://doi.org/10.1016/j.enconman.2020.113071

[141] E. A. Sarquis Filho, C. A. F. Fernandes, and P. J. da Costa Branco, "A complete framework for the simulation of photovoltaic arrays under mismatch conditions," Solar Energy, vol. 213, no. September 2019, pp. 13–26, 2021.

[142] S. K. Das, D. Verma, S. Nema, and R. K. Nema, "Shading mitigation techniques: State-of-the-art in photovoltaic applications," Renewable and Sustainable Energy Reviews, vol. 78, no. March, pp. 369–390, 2017. [Online]. Available: http://dx.doi.org/10.1016/j.rser.2017.04.093

[143] O. I. Olayiwola and P. S. Barendse, "Power electronic implementation of electrochemical impedance spectroscopy on photovoltaic modules," in IEEE Energy Conversion Congress and Exposition (ECCE), 2020. [Online]. Available: https://doi.org/10.1109/ecce44975.2020.9236404

[144] BioLogic, Accessed date: 2022-04-26. [Online]. Available: https://www.biologic.net/

[145] Solbian Flex SP50–L Flexible Photovoltaic Panels, Accessed date: 2022-04-26. [Online]. Available: https://www.dropbox.com/s/xtdp3axmxqkbg2a/SOLBIAN_50W_sp50l_eng.pdf

[146] LiteMeter 1-10V Pro, 2019, Accessed date: 2022-04-26. [Online]. Available: https://www.dropbox.com/s/3n7ah2ffkcnj2qb/LiteMeter.pdf

[147] Texas Instruments LM35 Precision Centigrade Temperature Sensors, 2017, Accessed date: 2022-04-26. [Online]. Available: https://www.dropbox.com/s/93mn12yd44r3pwt/lm35.pdf

[148] E. Von Hauff and D. Klotz, "Impedance spectroscopy for perovskite solar cells: Characterisation, analysis, and diagnosis," J. Mater. Chem. C, vol. 10, pp. 742–761, 2022. [Online]. Available: https://doi.org/10.1039/D1TC04727B

[149] R. A. Kumar, M. S. Suresh, and J. Nagaraju, "Facility to measure solar cell ac parameters using an impedance spectroscopy technique," Rev Sci Instrum, vol. 72, pp. 3422–3426, 2001. [Online]. Available: https://doi.org/10.1063/1.1386632

[150] N. Femia, G. Petrone, G. Spagnuolo, and M. Vitelli, Power Electronics and Control Techniques for Maximum Energy Harvesting in Photovoltaic Systems. CRC Press, 2013, ISBN: 978-1-315-21653-9.

[151] Kramers-Kronig Validity Test Lin-KK for Impedance Spectra: Lin-KK Tool, Accessed date: 2022-04-26. [Online]. Available: https://www.iam.kit.edu/et/Lin-KK.php

[152] B. A. Boukamp, "A linear Kronig-Kramers transform test for immittance data validation," J Electrochem Soc, vol. 142, no. 6, pp. 1885–1894, 1995. [Online]. Available: https://doi.org/10.1149/1.2044210

[153] M. Schönleber, D. Klotz, and E. Ivers-Tiffée, "A method for improving the robustness of linear Kramers-Kronig validity tests," Electrochim Acta, vol. 131, pp. 20–27, 2014, electrochemical Impedance Spectroscopy. [Online]. Available: https://doi.org/10.1016/j.electacta.2014.01.034

[154] M. Schönleber, R. Goyal, and E. Ivers-Tiffée, "Lin-KK tool: Operating rules and examples," Tech. Rep., 2014, Accessed date: 2022-04-26.

[155] S. Hara, H. Douzono, M. Imamura, and T. Yoshioka, "Estimation of photovoltaic cell parameters using measurement data of photovoltaic module string currents and voltages," IEEE J Photovolt, pp. 1–6, 2021. [Online]. Available: https://doi.org/10.1109/JPHOTOV.2021.3135262

[156] M. Piliougine, R. A. Guejia-Burbano, G. Petrone, F. J. Sánchez-Pacheco, L. Mora-López, and M. S. de Cardona, "Parameters extraction of single diode model for degraded photovoltaic modules," Renew Energ, vol. 164, pp. 674–686, 2021. [Online]. Available: https://doi.org/10.1016/j.renene.2020.09.035

[157] W. Zamboni, G. Petrone, G. Spagnuolo, and D. Beretta, "An evolutionary computation approach for the online/on-board identification of pem fuel cell impedance parameters with a diagnostic perspective," Energies, vol. 12, no. 22, 2019. [Online]. Available: https://www.mdpi.com/1996-1073/12/22/4374